SYNTHESIS AND CHARACTERIZATION OF BULK METALLIC GLASS MATRIX COMPOSITES

Thesis by

Haein Choi-Yim

In Partial Fulfillment of the Requirements

for the Degree of

Doctor of Philosophy

California Institute of Technology

Pasadena, California

1999

(Submitted November 3, 1998)

To Jaisig,

Boryoung and David

ACKNOWLEDGMENTS

I have always thought how lucky I am to meet such brilliant, kind people and to study in such a great place throughout the period of my stay at Caltech. My work would have not been possible without the support from many individuals. My advisor, Dr. Bill Johnson, gave me continuous inspiration and encouragement during exciting and frustrating times of my research for the last four years. I am thankful for him to give me a chance to join his group and support me in several ways. His exceptional scientific enthusiasm and optimism always kept me going further, not giving up.

I am grateful to Professor Brent Fultz for his kindness. His advise in scientific and nonscientific area has been a great help. He also instructed me in electron and X-ray diffraction both in the classroom and the laboratory.

My special thanks go to Dr. Ralf Busch, my collaborator on the composite project during the last two years. He always stimulated discussions and carefully proofread this thesis. Many other people in Keck lab have also been a great help. Dr. Xianghong Lin's work in developing non-beryllium bulk glass forming alloys laid the basis for this study. Dr. Xianghong Lin and Dr. Richard Dandliker showed me how to operate lab equipment, which was essential for my research. Dr. Dale Conner performed compressive and tensile tests and gave me an insight into mechanics. Carol Garland provided me valuable TEM pictures. I would like to thank to the rest of Keck lab people for their friendship, for help in lab, and for discussions on various issues. They are Dr. Valerie Scruggs, Dr. Chuck Hays, Dr. Jan Schroers, Dr. Joerg Loeffler, Dr.

Wenshan Liu, Dr. Kwanghyun Ryu, Jainzhong Li, Chuck Whitham, Andreas Masuhr, Sven Bossuyt, Stephen glade, Andy Waniuk, Michael Manley, Paul Kim, Pam Albertson, and Monica Palacios.

The financial support from the U.S. Army Research Office under grant number DAAH04-95-1-0233 and the Air Force Office of Scientific Research under grant number AFS 5 F4920-97-0323 are greatly appreciated.

I would like to thank to Dr. Michael Tenhover for performing Scanning Auger Microscopy (SAM) and Secondary Ion Mass Spectrometry (SIMS). I am grateful to Professor Uwe Koester for his help on fracture surface analysis during the Scanning Electron Microscopy (SEM) operation.

Finally, I would like to thank my parents, who encourage and support my education throughout my life in all ways they could. I also like to give my deepest thanks to my husband for being with me and encouraging me all the time. My lovely daughter and little baby son make me laugh even in times when I feel tired. I thank my mother-in-law for taking care of my daughter and son, while I wrote this thesis.

ABSTRACT

Composites with a bulk metallic glass matrix are synthesized and characterized. This was made possible by the recent development of bulk metallic glasses that exhibit high resistance to crystallization in the undercooled liquid state. In this thesis, experimental methods for processing metallic glass composites are introduced. Three different bulk metallic glass (BMG) forming alloys were used as the matrix materials. Ceramics such as SiC, WC, or TiC, and metals W or Ta were introduced as reinforcement into the metallic glass.

Structure, microstructure and thermal stability of the composites are studied by X-ray diffraction, optical microscopy and differential scanning calorimetry. The metallic glass matrix remained amorphous after adding up to 30 percent volume fraction of particles or short wires. X-ray diffraction patterns of the composites show only peaks from the second phase particles superimposed on the broad diffuse maxima from the amorphous phase. Optical micrographs reveal uniformly distributed particles in the matrix. The thermal stability of the matrix did not deteriorate after adding the particles. In the case of SiC, the matrix becomes even more robust with respect to crystallization.

The reactions at the interfaces between the matrix and the different reinforcing materials are investigated with scanning electron microscopy, transmission electron microscopy, and electron microprobe. At the interfaces between the matrix and the WC or SiC particles, ZrC layers formed. W and Si diffused into the matrix, repectively. At the interface between W and the matrix,

a thin layer of nanocrystals is observed after cooling the liquid/particulate mixture.

The mechanical properties of the composites are studied in compression and tension. Compressive strain to failure increased by over 300% compared to the unreinforced $Zr_{57}Nb_5Al_{10}Cu_{15.4}Ni_{12.6}$ and the energy to fracture of the tensile samples increased by over 50% adding 15 vol. % W.

The effect of silicon on the glass forming ability of $Cu_{47}Ti_{34}Zr_{11}Ni_8$ bulk metallic glass during composite processing is studied. Composites of the $Cu_{47}Ti_{34}Zr_{11}Ni_8$ bulk metallic glass, reinforced with up to 30 vol. % SiC particles are synthesized. During processing of the composites, a TiC layer forms around the SiC particles and Si diffuses into the $Cu_{47}Ti_{34}Zr_{11}Ni_8$ matrix stabilizing the supercooled liquid against crystallization. The small Si addition between 0.5 and 1 at. % increases the attainable maximum thickness of glassy ingots from 4mm for Cu-Ti-Zr-Ni alloy to 7mm for Cu-Ti-Zr-Ni-Si alloys. DSC analyses show that neither the thermodynamics nor the kinetics of the alloy is significantly affected by the Si addition. This suggests that Si enhances the glass forming ability by chemically passivating impurities such as oxygen and carbon that cause heterogeneous nucleation in the melt.

TABLE OF CONTENTS

LIST OF FIGURES

LIST OF TABLES

CHAPTER 1
INTRODUCTION

1.1 METALLIC GLASSES

1.1.1 Definition of Metallic Glasses

"Metallic glass" denotes an amorphous metallic solid, which is a noncrystalline metallic solid lacking long-range periodicity of the atomic arrangement. In contrast to the amorphous solid, in a perfect crystalline solid the atoms are arranged in a pattern that repeats periodically in three dimensions to a large or infinite extent. Metallic glass has been prepared by cooling the liquid at a rate sufficiently high to avoid a significant degree of crystallization, so that the disordered atomic configuration of the liquid state is frozen-in. This means that glass is a vitrified liquid, which thus has an atomic structure similar to that of a liquid.

When a liquid is cooled, one of two events may occur. Either crystallization may take place, or the liquid will become undercooled below T_m, becoming more viscous with decreasing temperature, ultimately forming a glass. The solidification to a glass is continuous and occurs over a range of temperature. In contrast, the first-order crystallization of the liquid is discontinuous and the solid crystal coexists with and grows into the liquid. These changes can be observed by monitoring the volume as a function of temperature, and a typical result is shown schematically in Fig. 1.1.[1] The crystallization process is manifested by an abrupt change in volume at T_m, whereas glass

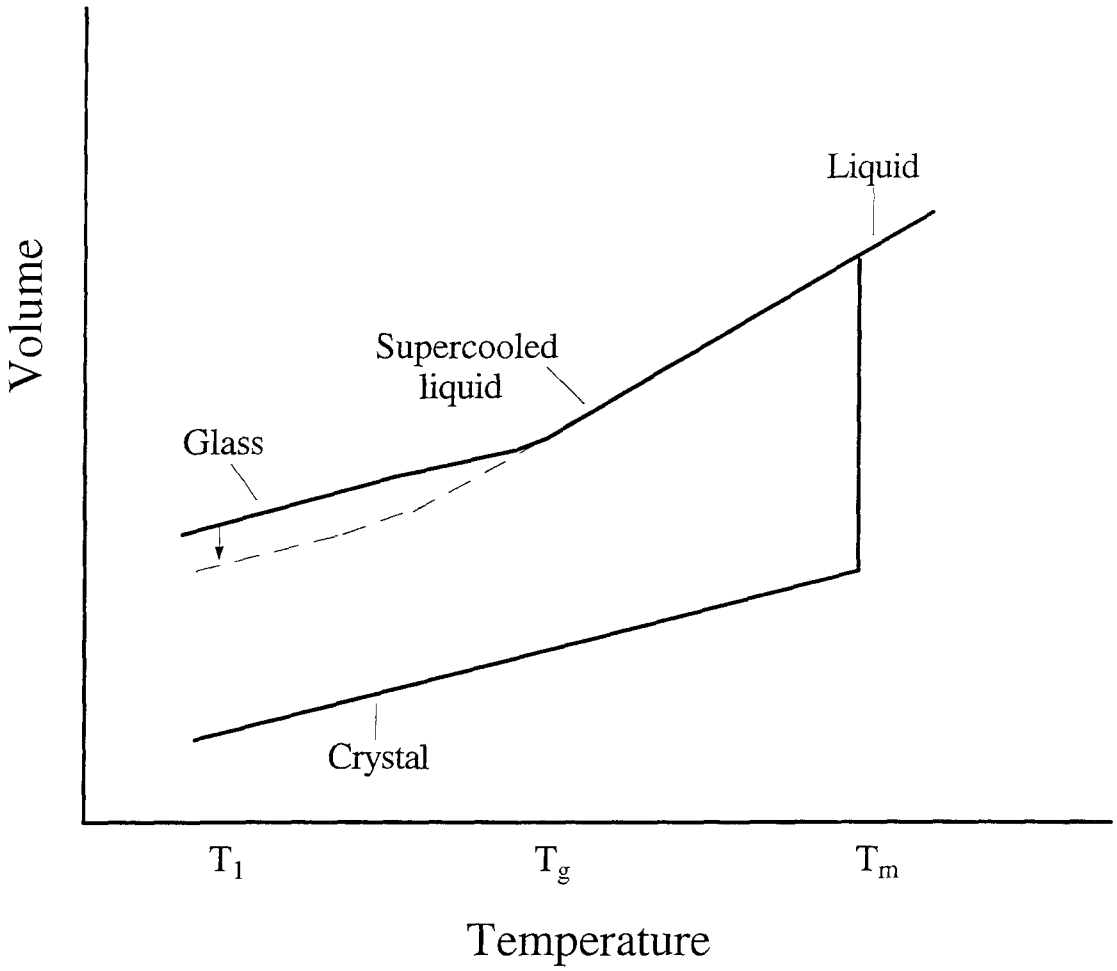

Fig. 1.1. Schematic illustration of the change in volume with temperature as an undercooled liquid is cooled through the glass transition temperature T_g. The vertical arrow illustrates the volume change accompanying the structural relaxation or stabilization of the glass if held at temperature T_1. Reproduced from ref. 1.

formation is characterized by a change in the slope. The temperature at which the change of slope occurs is termed the glass-transition temperature T_g.

The thermodynamic variables such as volume, entropy and enthalpy are continuous through the glass transition, but exhibit a change of slope there. This implies that at T_g there should be a discontinuity in derivative variables such as heat capacity ($C_p = (\partial H/\partial T)_p$) and thermal expansivity ($\alpha_T = \partial \ln V/\partial T$). Fig. 1.2 shows the heat capacity curves of a glass, the corresponding liquid and crystalline solid as a function of temperature.[2] The sudden increase in the heat capacity of the glass upon heating is the thermal manifestation of the glass transition. The glass transition is the phenomenon in which a solid amorphous phase exhibits a more or less abrupt change in derivative thermodynamic properties such as heat capacity or thermal expansivity, from the crystal-like to the liquid-like values with change of temperature. The glass transition temperature, T_g[3], is defined as the point of inflection of the rising heat capacity. The temperature of the glass transition is not a constant of the material, but is a function of experimental conditions. Thus, slower cooling rates will move the glass transition temperature to the lower temperature.

When the viscosity is about 10^{13} poise, the atomic configuration of the liquid becomes homogeneously frozen, at the glass transition temperature T_g. Above the glass transition region and the below the melting point, the material is an undercooled liquid which is metastable with respect to crystallization, but is in internal equilibrium. Below this region, it is a glass which is in a nonequilibrium state. Fig. 1.3 shows the viscosity of the undercooled liquid as a

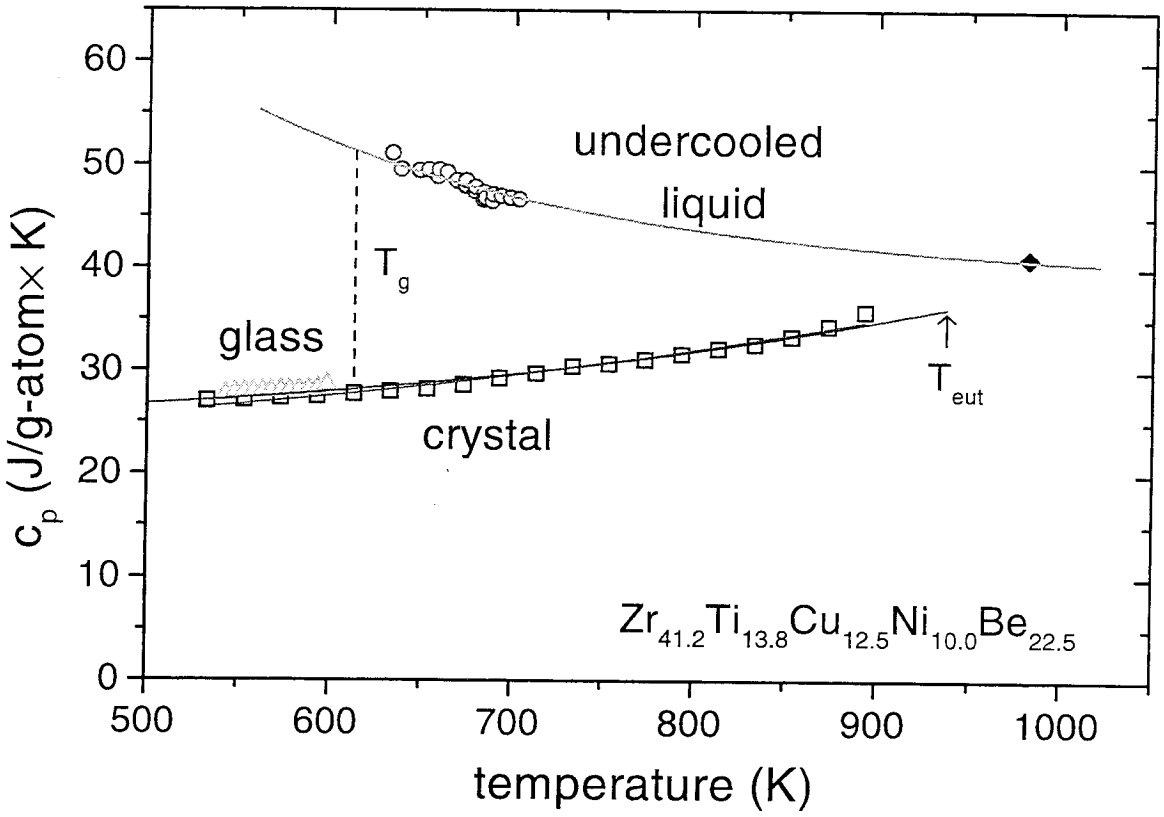

Fig. 1.2. Heat capacity curves of the $Zr_{41.2}Ti_{13.8}Cu_{12.5}Ni_{10}Be_{22.5}$ glass, the corresponding liquid and crystalline solid as a function of temperature. Reproduced from ref. 2.

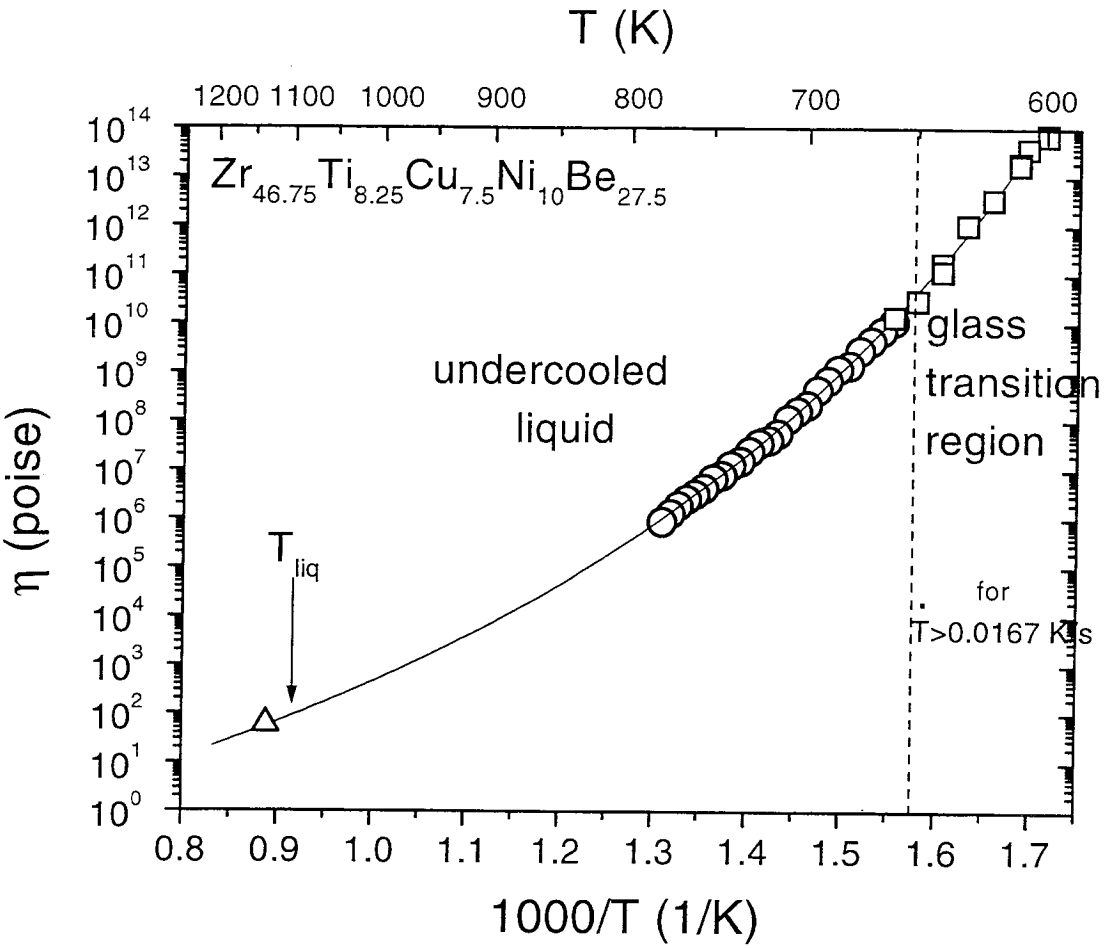

Fig. 1.3. Equilibrium viscosity as a function of temperature for the undercooled liquid of $Zr_{46.75}Ti_{8.25}Cu_{7.5}Ni_{10}Be_{27.5}$ alloy. Reproduced from ref. 4.

function of temperature.[4] It depicts the viscosity in the entire range from glass transition to the melting point. At T_g, viscosity reaches 10^{13} poise.

As mentioned before, high cooling rates are usually required to form metallic glasses. In silicate, in contrast, glass formation occurs easily. These materials, in which the atomic bonding is strongly covalent, are characterized by very high viscosity. In other words, the bonding places severe limits on the rate at which the atomic or molecular rearrangements, necessary for maintaining thermodynamic equilibrium during cooling, can occur. Thus, the melt solidifies to a glass, even at low rates of cooling often less than 10^{-2} K/s. Metallic melts, in contrast, have non-directional bonding, so that atomic rearrangements occur very rapidly. Hence, usually very high cooling rates (>10^5 K/s) are required to form metallic glasses.

1.1.2 History of Metallic Glasses

The first synthesis of a metallic glass was performed in 1960 when Klement, Willens and Duwez reported that a liquid $Au_{75}Si_{25}$ alloy, when rapidly quenched, would form an amorphous solid.[5]

Since Duwez et al. first reported the metallic glass formation from the liquid state, numerous glass forming alloys have been discovered. These metallic glasses have unique magnetic, mechanical, electrical and corrosion behavior, which results from the amorphous structure.[6] For example, some behave as very soft magnetic materials. Magnetic losses in high magnetization alloys have been measured which are lower than those measured in any other known crystalline

alloys. They are also exceptionally hard and show extremely high tensile strengths and electrical resistivities which are three to four times higher than those of conventional Fe or Fe-Ni alloys. The particular Fe-Cr-P-C alloy has extraordinarily high corrosion resistance in hostile environment.[7] This alloy is excellent coating material. However, these alloys required cooling rates of 10^5~10^6 K/s to suppress crystallization and form a glass. The high critical cooling rates limited the dimension of the samples to thin sheets or ribbons. This small dimension of the metallic glass limits the number of practical applications. In 1982, Drehman et al. reported the formation of a metallic glass as a bulk sample in the Pd-Ni-P alloy systems.[8] Bulk glassy material with thickness up to 1 cm could be produced at low cooling rates by fluxing the surface to avoid heterogeneous nucleation of crystals. In this thesis, we define a "bulk" glass as having a minimum dimension of 1 mm which is equivalent to a critical cooling rate of about 10^3 to 10^4 K/s.

In early 1990's, bulk metallic glass formation without fluxing became possible by judicious choice of the compositions in multicomponent alloy systems. These alloys are at deep eutectic compositions. This gives the melt the chance to cool easily to a low temperature at which its viscosity is quite high and thus the crystallization is sluggish enough to enable the melt to vitrify during the less rapid quenching. Inoue, Masumoto et al. have investigated a large variety of alloys such as La-Ni-Al[9], Mg-Cu-Y[10] and Zr-Cu-Ni-Al.[11] These systems have critical cooling rates of 100 K/s for glass formation and exhibit good thermal stability above the glass transition. Glassy samples could be quenched from the

melt up to dimensions of several millimeters in diameter. Peker and Johnson discovered the exceptionally good glass forming alloy system: Zr-Ti-Cu-Ni-Be.[12] The particular $Zr_{41.2}Ti_{13.8}Cu_{12.5}Ni_{10}Be_{22.5}$ alloy exhibits a critical cooling rate of 1 K/s.[13] This permits it to form amorphous samples with a smallest dimension of several centimeters in diameter (critical thickness). However, the toxicity of beryllium in Zr-Ti-Cu-Ni-Be system limits some practical applications.

More recently, Lin and Johnson found new bulk metallic glasses such as Cu-Ti-Zr-Ni[14] and Zr-Ti(Nb)-Cu-Ni-Al[15] with critical thickness of amorphous samples near 1 centimeter. The best Cu-Ti-Zr-Ni amorphous alloy is $Cu_{47}Ti_{34}Zr_{11}Ni_8$, Vit 101. It can be cast at least 4 mm thick. One of the most highly processible of the Zr-Ti(Nb)-Cu-Ni-Al amorphous alloys are $Zr_{52.5}Ti_5Cu_{17.9}Ni_{14.6}Al_{10}$, Vit 105 and $Zr_{57}Nb_5Cu_{15.4}Ni_{12.6}Al_{10}$, Vit 106. Glassy ingots of 1 cm thickness can be produced. The estimated critical cooling rate for these alloys is 10 K/s.[15] They have superior mechanical properties such as high strength (~1.9 GPa) and high elastic limit (~2%). They exhibit moderate stiffness of 85 GPa. They also exhibit good thermal stability above the glass transition. These new-developed non-beryllium alloys were used for the studies in this thesis.

Fig. 1.4 shows the critical cooling rates R_c for glass formation for some glass forming alloys versus the reduced glass transition temperature T_{rg}. The reduced glass transition temperature $T_{rg} = T_g/T_m$ is the ratio between the glass transition temperature T_g and the melting temperature T_m . High values of T_{rg} are

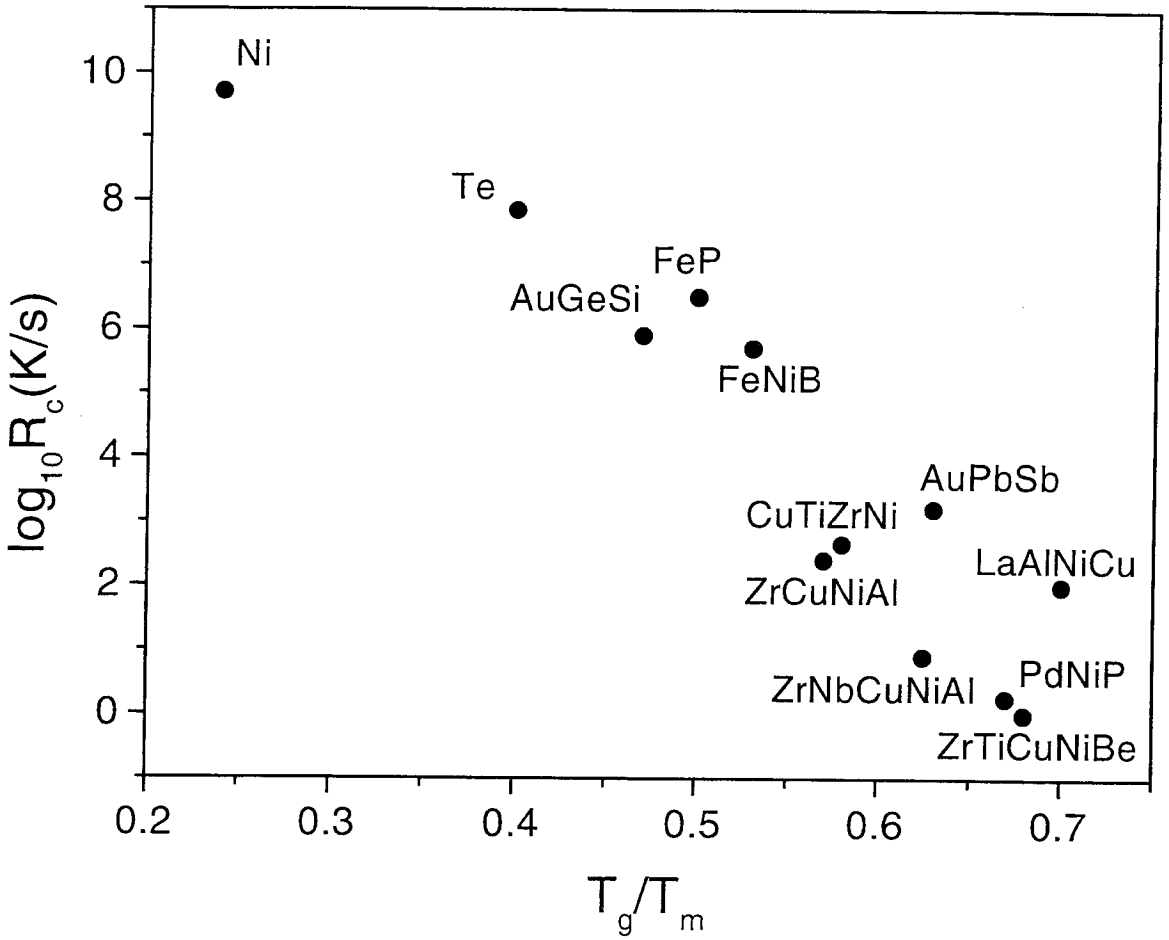

Fig. 1.4. Critical cooling rate, R_c, versus the reduced glass transition temperature, $T_{rg}=T_g/T_m$, for some glass forming alloys. Reproduced from refs. 12,14-21.

associated with good glass forming ability. For example, the $Pd_{40}Ni_{40}P_{20}$ alloy exhibits T_{rg}=0.66.[17] The $Zr_{41.2}Ti_{13.8}Cu_{12.5}Ni_{10}Be_{22.5}$ alloy has a T_{rg} of 0.67. The recently developed Vit 105 and 106 have T_{rg} of 0.638 and 0.62, respectively. All these alloys are among the best glass forming alloys of all known metallic glass forming systems and opens new opportunity for fundamental studies of the undercooled liquid state above glass transition temperature, T_g, as well as of the glass transition, which both were experimentally almost inaccessible before.

1.1.3 Synthesis of Metallic Glasses

Metallic glasses can be produced by a variety of techniques. They can be formed by rapid solidification of the alloying constituents from the gas or liquid phases. The first preparation technique of an amorphous metal from the liquid was the gun quenching.[5] In this process, the molten sample is held in the non-reactive crucible, then driven out of the hole in the form of small droplets by a shock wave. The droplets then impinge on the copper substrate, spreading out and overlapping to form a foil of variable thickness, which typically averages 5 to 25 μm. Some sections are very thin (~1000 A°), and thus are ideal for TEM study. Although the gun technique provides the highest cooling rates (10^6~10^8 K/s) of all liquid quenching techniques, the irregularity of the foil thickness means that the sample contains regions produced with different cooling rates and thus may contain different structures.

Regular foils of 20 to 50 μm thickness of foils are produced by hammer-anvil technique.[22] In this process, a molten droplet is quenched to a foil between two metallic pistons which are propelled at each other at high speed.

The melt spinning technique was the first potentially continuous process to be applied to metallic glasses.[23] In this technique, a stream of molten metal is directed at a rapidly rotating copper wheel. The final product is in the form of ribbons with a thickness of 20 to 100 μm.

Besides rapid quenching the molten alloy, it is also possible for produce amorphous alloys from the solid state. In 1983, Schwarz and Johnson observed the growth of an amorphous layer between two layers of crystalline metals at elevated temperature.[24] The other cases of solid state amorphization are high energy particle irradiation or mechanical attrition.

1.1.4 Crystallization of Supercooled Metallic Liquids and Glasses

An undercooled (supercooled) liquid is a thermodynamically metastable phase comparing to the corresponding equilibrium crystalline phases. This means that a supercooled liquid is not in the lowest-energy state and it will crystallize at high enough temperature and/or given long enough time. However, it is possible to kinetically constrain metastable phases so that the time required to transform is much longer than is measurable in laboratory.

One of the most important factors successfully processing composites with a metallic glass matrix is to control crystal nucleation and growth. The crystalline solid additions to the glass forming melts could act as catalytic sites

for heterogeneous crystal nucleation and growth. The other possibility is homogeneous crystal nucleation and growth. Dissolution or reaction of an excessive amount of the reinforcement phase with the metallic glass matrix changes the composition of the metallic glass in a manner which shifts the composition away from the optimum glass forming range. In this section, homogeneous and heterogeneous nucleation theory will be reviewed.

As shown in Fig. 1.5, the liquid has a higher Gibbs free energy than the crystal below the melting temperature. Therefore, a liquid becomes metastable with respect to the crystal, when the liquid is cooled below its melting temperature. The free energy difference represents the driving force for the nucleation of crystals from the liquid. However, the creation of the liquid-crystal interface disfavors the nucleation of the crystal since it contains a positive interfacial energy. According to the classical homogeneous nucleation theory [25,26], the free energy change upon nucleation is given by two terms. The first is the free energy decrease due to the liquid to crystal transformation, which is proportional to the volume of the embryo. The second term is the free energy increase due to the creation of liquid-crystal interface, which is proportional to the surface area of the embryo. The total Gibbs' free energy change associated with the formation of a spherical crystalline embryo with radius r is given by

$$\Delta G = 4\pi r^2 \sigma + \frac{4\pi}{3} r^3 \Delta G_v \qquad (1.1)$$

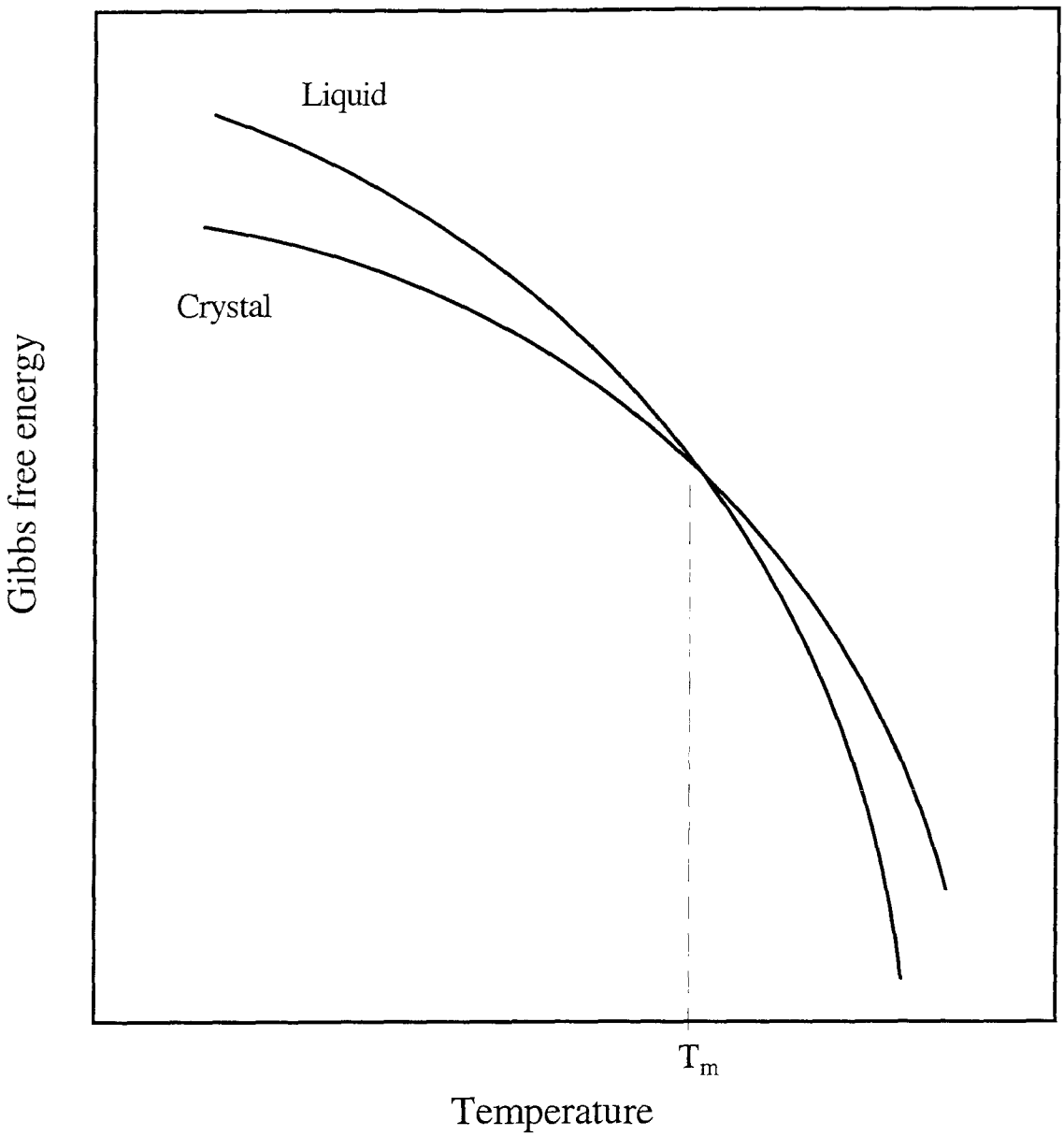

Fig. 1.5. Gibbs free energy curves for liquid and corresponding crystal with respect to the temperature.

where σ is the liquid-crystal interfacial energy per unit area, ΔG_v is the difference in free energy between liquid and crystal per unit volume. In Fig. 1.6, ΔG is shown as a function of embryo radius r. Below the melting point, interfacial energy σ and volume free energy ΔG_v will compete as r increases. The competition between these two terms gives a free energy maxima:

$$\Delta G^* = \frac{16\pi}{3}\left(\frac{\sigma^3}{\Delta G_v^2}\right) \tag{1.2}$$

at a critical nucleus radius

$$r^* = -\frac{2\sigma}{\Delta G_v} \tag{1.3}$$

ΔG^* is the nucleation energy barrier. Thus, the crystalline nuclei larger than critical nucleus radius r^* will grow with decreasing free energy and be stabilized. Crystalline nuclei smaller than r^* will tend to remelt with increasing free energy.

The number of embryos that have reached the critical radius r^* can be obtained from the Boltzmann distribution:

$$n^* = n\exp\left(-\frac{\Delta G^*}{kT}\right) \tag{1.4}$$

where n is total number of atoms in the system, k is the Boltzmann constant, and T is the absolute temperature. Below the melting point T_m, Equation 1.4 only applies for $r \leq r^*$ because embryos greater than the critical size are stable nuclei of solid and no longer part of the liquid. Then the nucleation rate I is governed

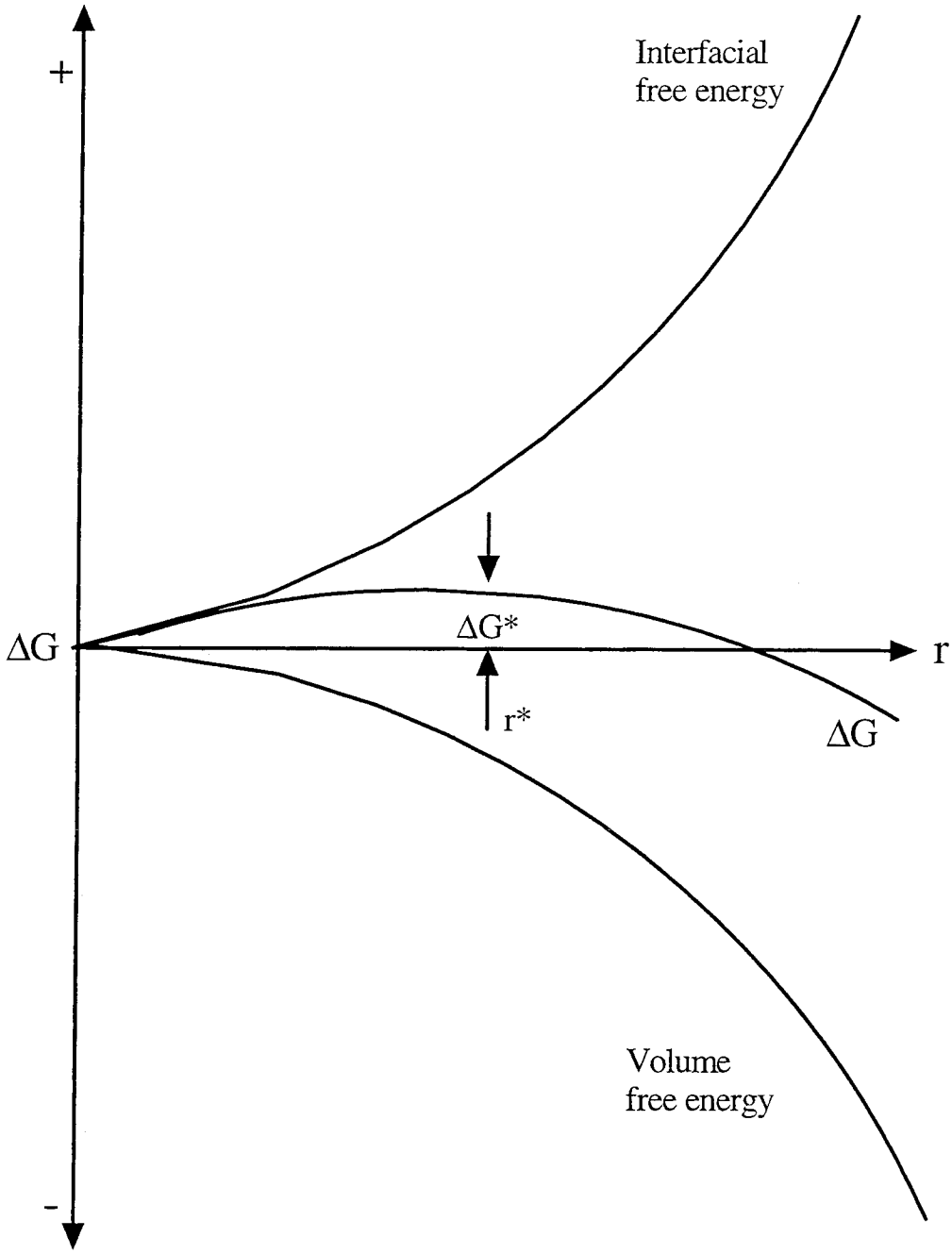

Fig. 1.6. Gibbs free energy ΔG_v associated with the nucleation of a crystalline embryo as a function of its radius.

by the rate at which smaller embryos can grow to the critical size. For the small embryos to grow, atoms need to transported from the liquid side of the interface to the crystal side so that the embryos growth rate is determined by the rate of atom transport which is described by the atomic diffusivity D. The diffusivity is related to the viscosity by the Stokes-Einstein relation,

$$D = \frac{kT}{3\pi a_0 \eta} \tag{1.5}$$

Where a_0 is the interatomic distance, k is Boltzmann constant.

Therefore, the homogeneous nucleation rate contains two terms, one results from free energy difference between liquid and crystal, the other from the atomic mobility. It is given by

$$I = \frac{k_n}{\eta(T)} \exp\left(-\frac{\Delta G^*}{kT}\right) \tag{1.6}$$

Where k_n is a kinetic constant, η is the viscosity. As the liquid is cooled below the melting point, the driving force for nucleation is continuously increasing. This is opposed by the rapidly decreasing atomic mobility at very high undercoolings. The overall nucleation rate reflects these two factors by increasing from zero at the transformation temperature T_m to a maximum value somewhere below T_m and then decreasing with further decreases in temperature as shown in Fig. 1.7.[27]

The viscosity of undercooled melts has been found to be well described by the Vogel-Fulcher equation:

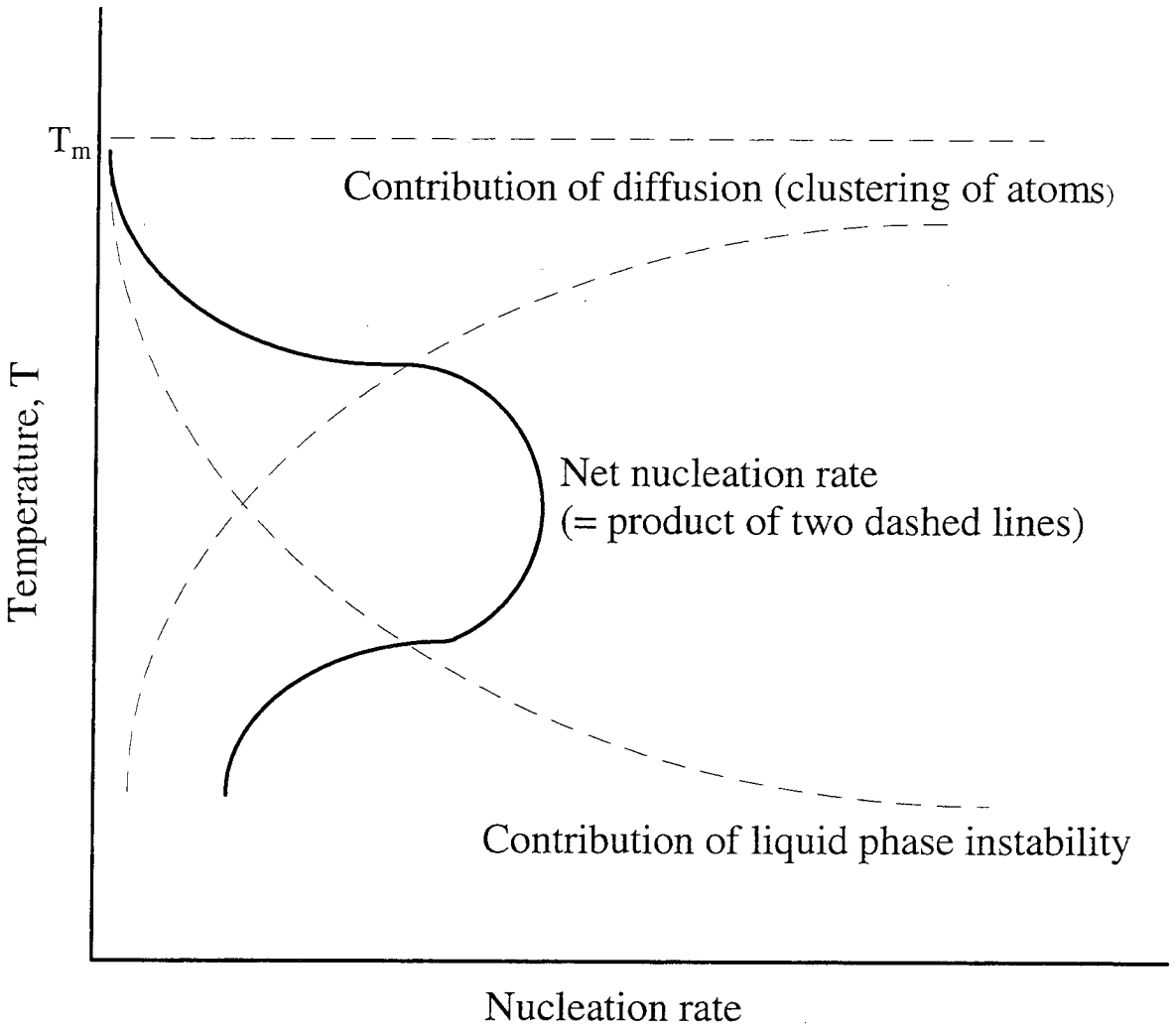

Fig. 1.7. The rate of nucleation is a product of two curves that represent two opposing factors (instability and diffusivity). Reproduced from ref. 27.

$$\eta(T) = A\exp\left(\frac{B}{T - T_0}\right) \tag{1.7}$$

where A,B and T_0 are constants.

Using the linear approximation, the expression for ΔG becomes:

$$\Delta G = -\frac{L\Delta T_r}{V_m} \tag{1.8}$$

and the homogeneous nucleation frequency becomes:

$$I = \frac{k_n}{\eta(T)}\exp\left(-\frac{16\pi}{3}\frac{\alpha^3\beta}{\Delta T_r^2 T_r}\right) \tag{1.9}$$

where L is the molar latent heat of fusion, V_m is molar volume of the crystal, T_r $=T/T_m$, $\Delta T_r = 1\text{-}T_r$ and α and β are dimensionless constants defined by:

$$\alpha = \frac{(N_A V_m^2)^{1/3}\sigma}{L}\ ; \qquad \beta = \frac{L}{RT_m} \tag{1.10}$$

where N is Avogardro's number.

Turnbull obtained the homogeneous nucleation frequency as a function of reduced temperature T_r for alloys of varying reduced glass transition temperature T_{rg} as shown in Fig. 1.8.[28] One sees that for T_{rg}<1/2, the maximum nucleation rate will be too large to make glass formation possible, while for T_{rg}>2/3, the nucleation rates are so low that crystallization can be easily avoided, which in turn results the formation of bulk metallic glasses.

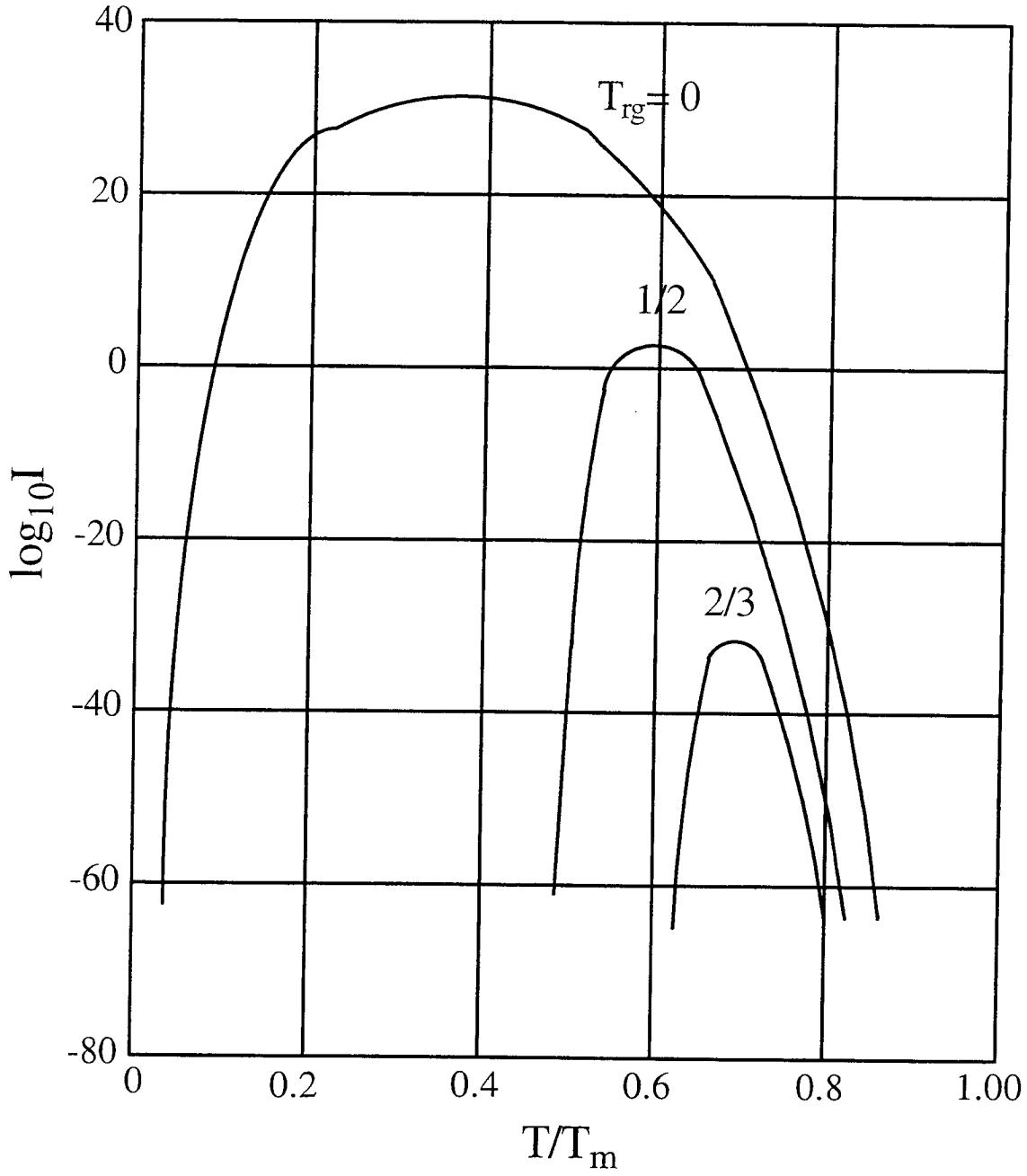

Fig. 1.8. The logarithm of the nucleation frequency (in nuclei/cm^{3}s) as a function of reduced temperature T/T_m for various values of the reduced glass transition temperature $T_{rg}=T_g/T_m$. Reproduced from ref. 28.

The above arguments only consider homogeneous nucleation. Additionally, the formation of a nucleus of the critical size can be catalyzed by a solid particle suspended in the liquid, the surface of the container, or a solid film, such as oxide, on the surface of the liquid. This nucleation which is catalyzed by a suitable surface in contact with the liquid is called heterogeneous nucleation.

Consider a solid embryo forming in contact with a perfectly flat substrate as shown in Fig. 1.9. Assuming that the interface is stable and in equilibrium, the balance for the horizontal components of the surface tension requires:[29]

$$\sigma_{SL} = \sigma_{SC} + \sigma_{LC} \cos\theta \tag{1.11}$$

where σ_{SL}, σ_{SC}, and σ_{LC} are the interfacial energies between substrate and liquid, substrate and crystal, and liquid and crystal, respectively. θ is the angle of contact between the crystalline embryo and the substrate, also known as the wetting angle.

It is convenient to represent the surface energy relationship by the parameter m which is defined as:

$$m = \frac{\sigma_{SL} - \sigma_{SC}}{\sigma_{LC}} \tag{1.12}$$

If m>1, then there is complete contact. The crystal spreads completely across the surface of the substrate. If m<-1, then no contact occurs, and any contact between embryo and substrate causes increase in interfacial energy. A spherical cap forms for any value of m between +1 and –1.

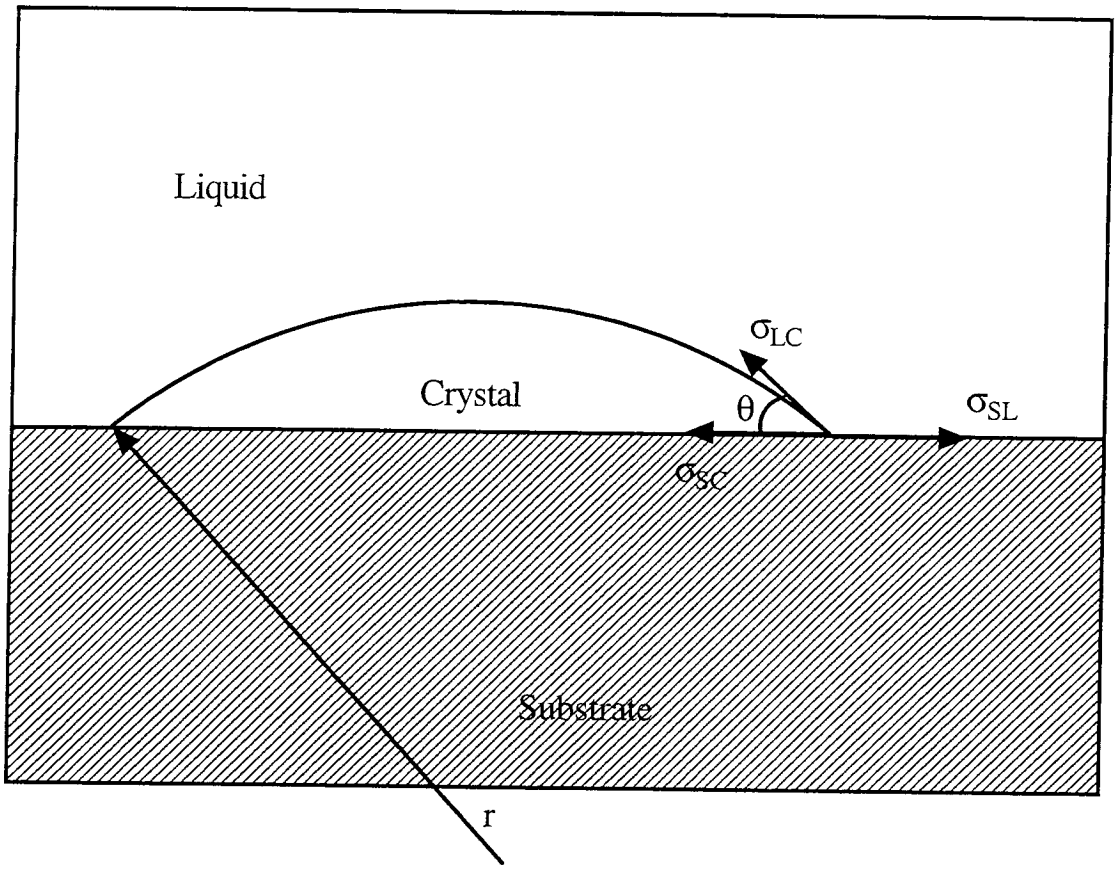

Fig. 1.9. Stability of a spherical cap shaped embryo on a substrate.

Reproduced from ref. 29.

For a spherical cap, the surface area representing the interface between the liquid and the embryo is:

$$A = 2\pi (1\text{-}\cos\theta)\, r^2 \tag{1.13}$$

And the volume is given by:

$$V = \frac{1}{3}\pi(1-\cos\theta)^2(2+\cos\theta)r^3 \tag{1.14}$$

The Gibbs free energy change associated with the formation of a spherical cap shaped crystalline embryo is given by:

$$\Delta G_{hetero} = 2\pi(1-\cos\theta)r^2\sigma_{LC} + \pi(r\sin\theta)^2(\sigma_{SC}-\sigma_{SL}) + \frac{\pi}{3}(1-\cos\theta)^2(2+\cos\theta)r^3\Delta G_v \tag{1.15}$$

The first term represents the interfacial energy between the liquid and the crystalline embryo. The second term is the energy of replacing the interface between substrate and liquid by one between substrate and crystal, and the third term is the energy of converting the volume of liquid to crystal. This can be rewritten using the energy change for homogeneous nucleation ΔG.

$$\Delta G_{hetero} = f(\theta)\Delta G = \frac{(1-\cos\theta)^2(2+\cos\theta)}{4}\Delta G \tag{1.16}$$

Differentiating with respect to r, we find that ΔG_{hetero} has maximum at the same point as ΔG. Thus, the radius of critical spherical cap for heterogeneous

nucleation is the same as the radius of critical nucleus for homogeneous nucleation. However, the energy of formation is reduced by the factor $f(\theta)$.

Similar to Eqn 1.6, the heterogeneous nucleation rate is given by:

$$I_{hetero} = \frac{k_n}{\eta(T)} \exp\left(-\frac{f(\theta)\Delta G^*}{kT}\right) \tag{1.17}$$

Since a $f(\theta)$ is between 0 and 1, it increases heterogeneous nucleation rates that are thus often orders of magnitude larger than homogeneous nucleation rates.

1.2 COMPOSITES

1.2.1 Definition and Classification of Composites

A composite is defined as any material that consists of two or more materials deliberately combined to form heterogeneous structures with desired or intended properties.[30] Mud bricks reinforced with straw were known to have been made for many centuries, as were laminated woods. Recently there has been more considerable scientific and industrial interest in a variety of composites as a way to improve mechanical properties such as stiffness, fracture toughness, and high temperature strength as well as magnetic and electrical properties.

Compromises in performance, production rate, and cost are often required since no single material will have all of the best properties. Therefore, the material must be chosen to have the best characteristics for the most important properties and minimal degradation of the others.

Categorization of different composites could be based on the matrix material used. The matrix serves two very important functions: First, it holds the

reinforcement phase in place and, secondly, it transfers loads to the reinforcement. Matrix materials are usually polymers, ceramics, or metals: reinforcements are used from all three of these classes as well. The polymer matrices are by far the most common and particularly attractive because of their relatively easy processibility, low-density, and good mechanical and dielectric properties. Ceramic and metal matrices are most often used when polymer matrices will not suffice, usually because of their temperature limitations.

Ceramics have very high melting points, high compressive strength, and excellent resistance to corrosion and oxidation. These excellent properties give the principal reasons for their use as matrix materials. On the other hand, ceramics are brittle. This lack of toughness also motivates the fabrication of ceramic matrix composites. Thus, the ceramic matrix contributes the high temperature properties while the reinforcement improves the toughness by providing resistance to crack growth.

Metal-matrix composites, although not as widely used as polymer matrix composites, are currently a subject of great interest. Metal matrices offer good stiffness and strength, good high temperature capabilities, and low thermal expansion. A major problem of metal matrix composites with continuous reinforcements is the inherent non-wettability of most fibers with metal matrix. Various approaches are being pursued to overcome this problem such as coating fibers. Alternatively, high pressure assists in wetting.

The other way to categorize different composites is based on the type of reinforcement. Reinforcements for composites can be long or short fibers,

particles, or whiskers. Continuously reinforced composites provide maximum strength and stiffness on one direction but are anisotropic.[31] Discontinuously reinforced composites have been demonstrated to offer essentially isotropic properties with substantial improvements in strength and stiffness relative to those available with unreinforced materials.[32] Particulate composites have the further advantages of being machinable and workable using many conventional processing techniques.

1.2.2 Fabrication Processes of Composites

A variety of processing techniques have been developed for the fabrication of composites. For metal matrix composites, processing can be divided into two stages.[33] One is primary material production and the other is secondary consolidation or forming operations. A further important distinction can be drawn for the primary processes depending on whether the matrix becomes liquid at any stage.

Primary processes can be divided into two distinct techniques: liquid matrix primary processing and non-liquid matrix primary processing. Liquid matrix primary processing includes a number of techniques in which the reinforcements are initially incorporated into the molten matrix. After the matrix becomes molten, it is brought into contact with the reinforcement. This generally favors intimate interfacial contact between the matrix and reinforcement and hence a stronger bond. However, the high temperature to keep the matrix molten can lead to excessive reaction, which can also lead to the formation of a brittle

interfacial reaction layer. These features are sensitive to a number of factors such as liquid/reinforcement contact time and pressure. Thus, short contact time and high pressure during processing can be a solution of this drawback of liquid matrix primary processing.

For the liquid matrix primary processing, three basic techniques exist: squeeze casting and squeeze infiltration, spray deposition, and slurry casting (compocasting). The term squeeze casting has been applied to various processes in which pressure is imposed on a solidifying system, usually via a single hydraulically activated ram. The ram movement is usually slow and the applied pressure often greater than is typical of die-casting. Squeeze casting can be applied to metal matrix composites, as reheated powder mixtures or as stir-cast material, but the most common pressure-assisted solidification process for metal matrix composite production is properly termed squeeze infiltration. This involves the injection of liquid metal into the interstices of an assembly of fibers or particle, usually called a preform.

The spray deposition technique was developed commercially in the late 1970s and throughout the 1980s by Osprey Ltd. as a method of building up bulk material by atomizing a molten stream of metal with jets of cold gas. The reinforcement can be fed into the spray. The advantages of this technique are rapid solidification and low oxide contents. The disadvantages are significant porosity levels and difficulties in obtaining homogeneous distributions of reinforcement.

The simplest and most economically attractive method of metal matrix composite manufacture is slurry casting. Slurry casting is the technique, which stir mix the liquid metal with solid reinforcement prior to forming and then allows the mixture to solidify. The slurry can be continuously agitated while the reinforcement is progressively added. This can in principle be done using fairly conventional processing equipment. In this study, the slurry casting technique was adapted to make particulate or short wires reinforced metallic glass matrix composites.

It is also possible to produce metal matrix composites without the matrix ever becoming even partially liquid while in contact with the reinforcement. However, this may result in less intimate interfacial contact. These non-liquid matrix primary processing techniques include powder blending, diffusion bonding, and physical vapor deposition. The most common form of non-liquid primary processing is powder blending that mix the reinforcement together with the matrix in powder form. This convenient and versatile technique for metal matrix composite production offers excellent control over the reinforcement content across the complete range. The blending can be carried out dry or in liquid suspension. This is usually followed by the secondary processing such as extrusion or hot isostatic pressing (HIPing). However, it can be difficult to achieve a homogeneous mixture during blending, particularly fibers and whiskers, which tend to persist in the form of tangled agglomerates.

Diffusion bonding can be used to join the same or dissimilar metals. As the name implies, interdiffusion of atoms between clean metal surfaces at the

temperature generally below the melting point of metals is responsible for creating the joint.[34] Diffusion bonding has been successfully adapted to the fabrication of metal matrix composites. The placement of arrays of long fibers between thin metallic foils is followed by a hot pressing operation. This allows plastic flow of the foil material around the reinforcement. This is a good technique for making continuous fiber composites because interfacial reactions can be easily controlled due to the lower temperatures compared to the liquid matrix processing. The drawback of this process is that the overall procedure is slow and cumbersome and there can be difficulties on obtaining very high fiber volume fractions and homogeneous fiber distributions.

Physical vapor deposition can also be used to join reinforcement and matrix. The matrix material is deposited directly onto a single wire by evaporation. Composite fabrication is usually completed by assembling the coated fibers into a bundle and consolidating this in a hot pressing or HIPing operation. A very uniform distribution of fibers is produced in this way. The other advantage of this technique is that a wide range of matrix compositions can be used.

A number of secondary processes can be applied to metal matrix composite materials. Secondary processes are required for consolidation, generating fiber alignment and/or forming into a required shape. These include extrusion, drawing, rolling, forging, and hot isostatic pressing (HIPing).

1.2.3 Basic Principles of Composites

It is obvious that the properties of composites must, in some way, represent an averaging of the properties of their individual components. However, the precise nature of the "average" is a sensitive function of microstructural geometry. Fig. 1.10 illustrates three idealized geometries: (a) a direction parallel to continuous fibers, (b) a direction perpendicular to continuous fibers, and (c) a direction relative to a uniformly dispersed particle composite.[27] The first two cases represent extremes in the highly anisotropic nature of fibrous composites. The third case represents an idealized model of the relatively isotropic nature of particle composites.

(a) Loading Parallel to Reinforcing Fibers – Isostrain

This loading system is obviously of most practical interest, since by loading in the direction of the fiber, the high modulus and strength of fiber material can be fully exploited. If the matrix is intimately bonded to the reinforcing fibers, the strain of both the matrix and the fibers must be the same. This isostrain condition is true even though the elastic moduli of each component will tend to be quite different. In other words,

$$\varepsilon_c = \frac{\sigma_c}{E_c} = \varepsilon_m = \frac{\sigma_m}{E_m} = \varepsilon_f = \frac{\sigma_f}{E_f} \tag{1.18}$$

where c refers to the composite, m to the matrix, and f to the fiber. The load carried by the composite, P_c, is the simple sum of loads carried by each component:

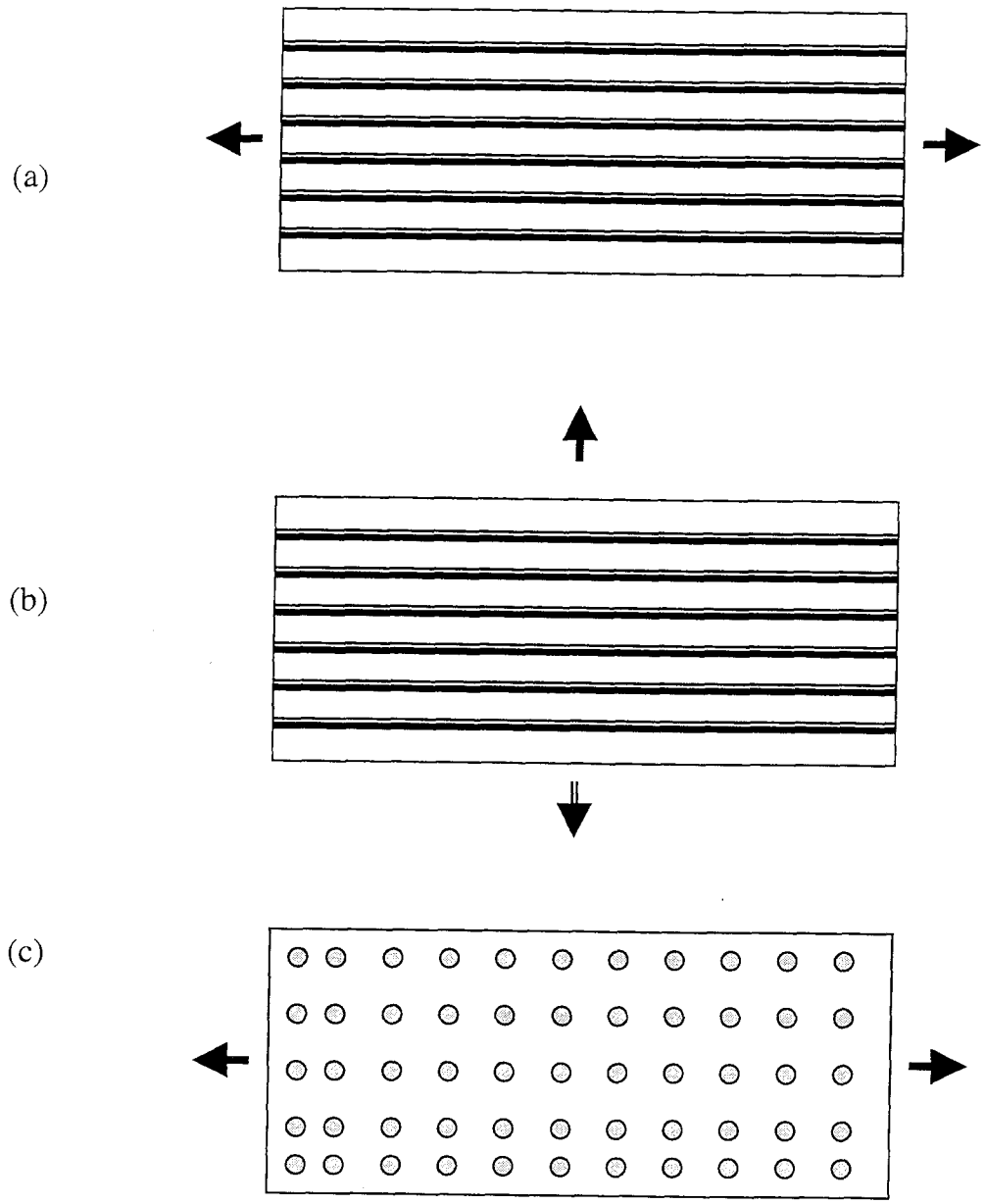

Fig. 1.10. Three idealized composite geometries: (a) a direction parallel to continuous fibers in a matrix, (b) a direction perpendicular to continuous fibers in a matrix, and (c) a direction relative to uniformly dispersed particle composite. Reproduced from ref. 27.

$$P_c = P_m + P_f \tag{1.19}$$

Each load is defined as a stress times an area, that is,

$$\sigma_c A_c = \sigma_m A_m + \sigma_f A_f \tag{1.20}$$

Dividing through by the composite area, A_c and converting area fractions to volume fractions (by multiplying each area by length, l) gives the relationship for the axial stress:

$$\sigma_c = f\,\sigma_m + (1\text{-}f)\,\sigma_f \tag{1.21}$$

where f represents the volume fraction of the matrix phase. Combining Eqns 1.18 and 1.20, and dividing through by A_c, gives the elastic modulus:

$$E_c = E_m \frac{A_m}{A_c} + E_f \frac{A_f}{A_c}$$

$$= f E_m + (1\text{-}f) E_f \tag{1.22}$$

Eqn. 1.22 identifies the modulus of a fiber composite loaded axially as a simple, weighted average of the moduli of its components. This Eqn is often called "rule of mixture" approximations and does not only apply to the modulus of elasticity. A number of properties such as transport properties exhibit this behavior.

(b) Loading Perpendicular to Reinforcing Fibers- Isostress

A substantially different result is obtained for the case of perpendicular loading of the reinforcing fibers. In this case, stress is assumed equal in both the reinforcement and the matrix. The composite strain is then expressed as a weighted average:

$$\varepsilon_c = f\,\varepsilon_m + (1\text{-}f)\,\varepsilon_f \tag{1.23}$$

Since the isostress condition requires that $\sigma=E_c\varepsilon_c=E_m\varepsilon_m=E_f\varepsilon_f$, we can rewrite Eqn. 1.23 as:

$$\frac{\sigma}{E_c} = f\frac{\sigma}{E_m} + (1-f)\frac{\sigma}{E_f} \tag{1.24}$$

Dividing out the σ term and rearranging gives the composite modulus:

$$E_c = \left(\frac{f}{E_m} + \frac{(1-f)}{E_f}\right)^{-1} \tag{1.25}$$

Eqn. 1.25 (isostress condition) is a less effective use of the high modulus of the reinforcing fibers compared to the Eqn. 1.22 (isostrain condition), in which the high modulus of the reinforcing fibers can be fully exploited.

(c) Loading a Uniformly Dispersed Particle Composite

A rigorous treatment of this system can become quite complex depending on the specific nature of the dispersed and continuous phases. Fortunately, the results of the two previous cases (isostrain and isostress fiber composites) serve as upper and lower bounds for the dispersed particle case. A simple approximation to the results for particulate composites is given by noting that the Eqns. 1.22 and 1.25 can both be written in the general form:

$$E_c^n = fE_l^n + (1-f)E_h^n \tag{1.26}$$

where *l* refers to the low modulus phase and *h* refers to the high modulus phase; *n* is 1 for the isostrain case (Eqn. 1.22) and –1 for the isostress case (Eqn. 1.25). For a first approximation, a higher-modulus particle in a lower-modulus matrix can be represented by n=0 in Eqn. 1.26. Similarly, a lower-modulus particle in a higher-modulus matrix can be represented by n=1/2.

Fig. 1.11 summarizes these cases. The composite modulus for a particulate composite is generally between the extremes of isostrain and isostress conditions. Two simple examples are given by Eqn. 1.26 for n =0 and 1/2. Decreasing n from a +1 to –1 represents a trend from a relatively low-modulus particle in a relatively high-modulus matrix to the reverse case of a high-modulus particle in a low-modulus matrix.

1.2.4 Interfacial Strength of Composites

The bonding between reinforcement and matrix is critical to the performance of the composite material. That is, the interface between the reinforcement and matrix must be strong enough to transfer the stress or strain due to a mechanical loading from one phase to the other.[33] There is considerable evidence that chemical reaction, provided it remains limited to a thin layer, can help to ensure intimate interfacial contact and hence raise the bond strength. Without this strength, the dispersed phase can fail to communicate with the matrix. Rather than have the "best of both worlds," we may obtain the worst behavior of each omponent. However, the toughness of material (which is the ability of the material to absorb energy) is sometimes increased by a weak bond

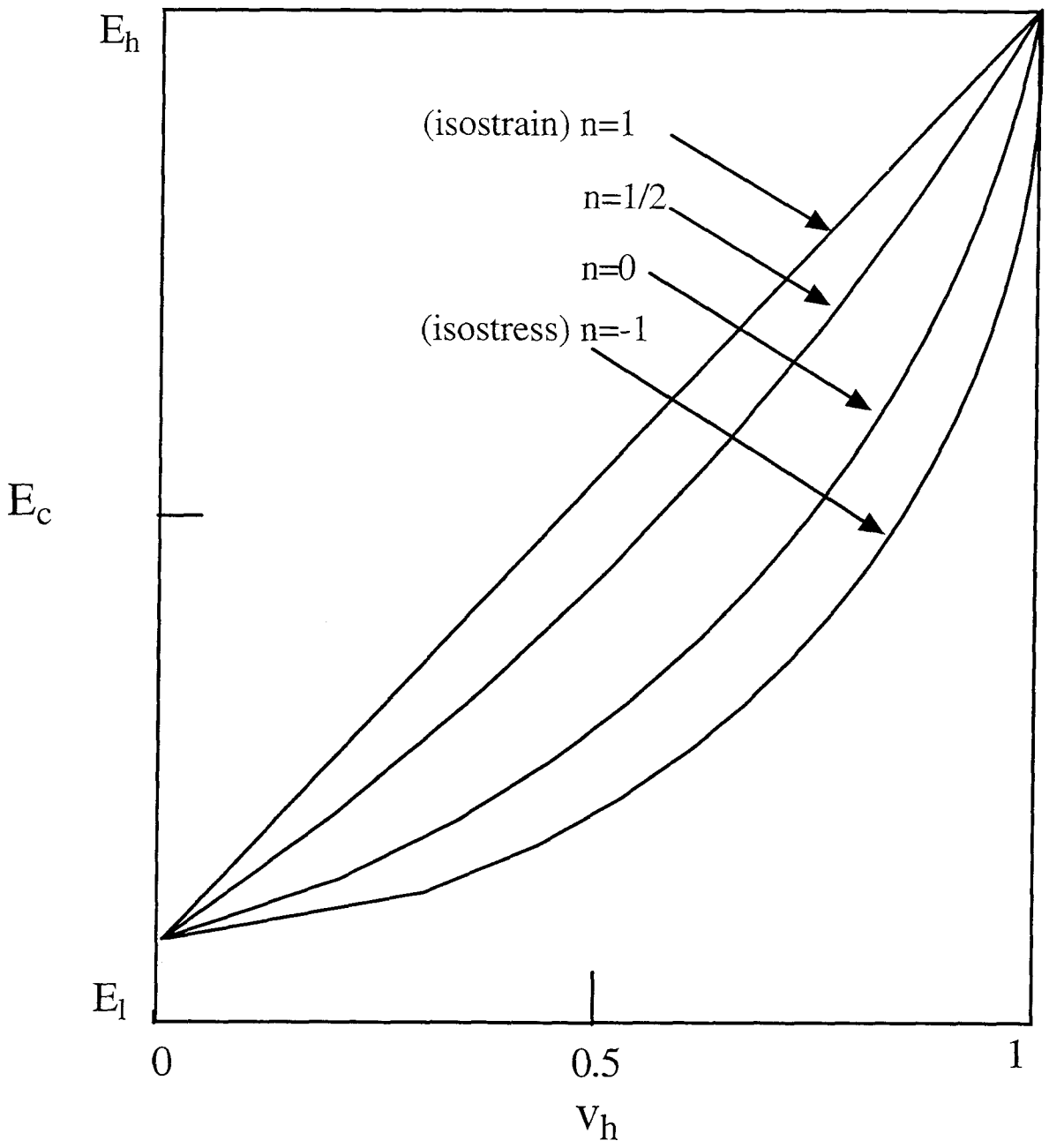

Fig. 1.11. The dependence of composite modulus, E_c, on the volume fraction of a high-modulus phase, v_h, for a particulate composite is generally between the extremes of isostrain and isostress conditions: n is 1 for the isostrain case and –1 for isostress case. These two cases serve as upper and lower bounds for the dispersed particulate case. Reproduced from ref. 27.

between matrix and reinforcement. This allows slipping between matrix and reinforcement, which promote energy dissipation at the interface.

Interfacial stresses can arise from differential thermal contraction and from prior plastic flow of the one phase (matrix or reinforcement), as well as by the application of an external load. These stresses can activate a variety of inelastic processes, as is illustrated shematically in Fig. 1.12. This figure represents the stresses near the interface, which is arising from an applied load and from differential thermal contraction. These stresses initiate the various inelastic processes as shown Fig. 1.12 (b). These processes occurring at or near the interface can act to relax the stress state by unloading the fiber. Energy is absorbed when these processes are activated, and this may make a significant contribution to the toughness of the composite. The composite toughening arises from an initial debonding as well as a fictional sliding for the debonded fibers. In addition, toughening can be accomplished by the work done of plastic deformation of ductile fibers. Therefore, large increases in toughness may be available if the pull-out and plastic deformation can be combined.

Interfacial reaction may occur both during composite fabrication and under service conditions. Interfacial reaction is controlled by the thermodynamics and kinetics factors. A large negative heat of mixing induces a reaction at the interface between reinforcement and matrix with a large thermodynamic driving force. If heat of mixing is positive, then the reaction will not take place at all, but a large negative value does not necessarily mean that it will occur quickly.

(a)

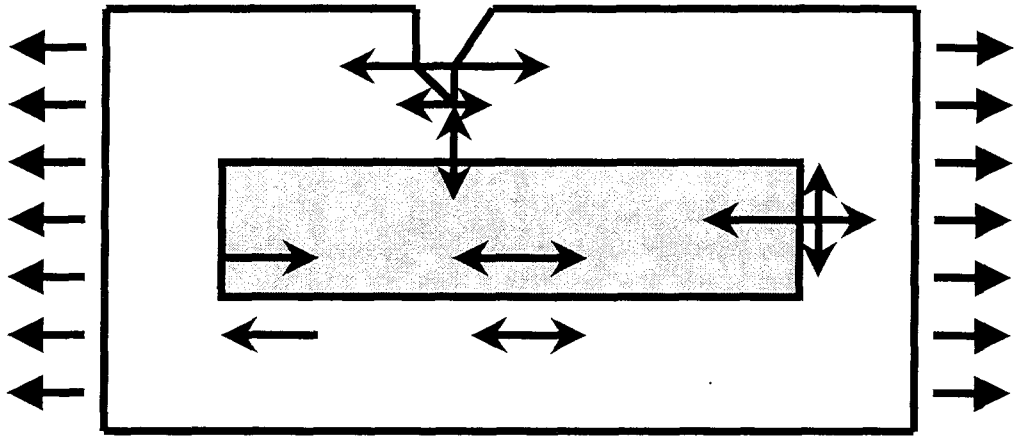

(b)

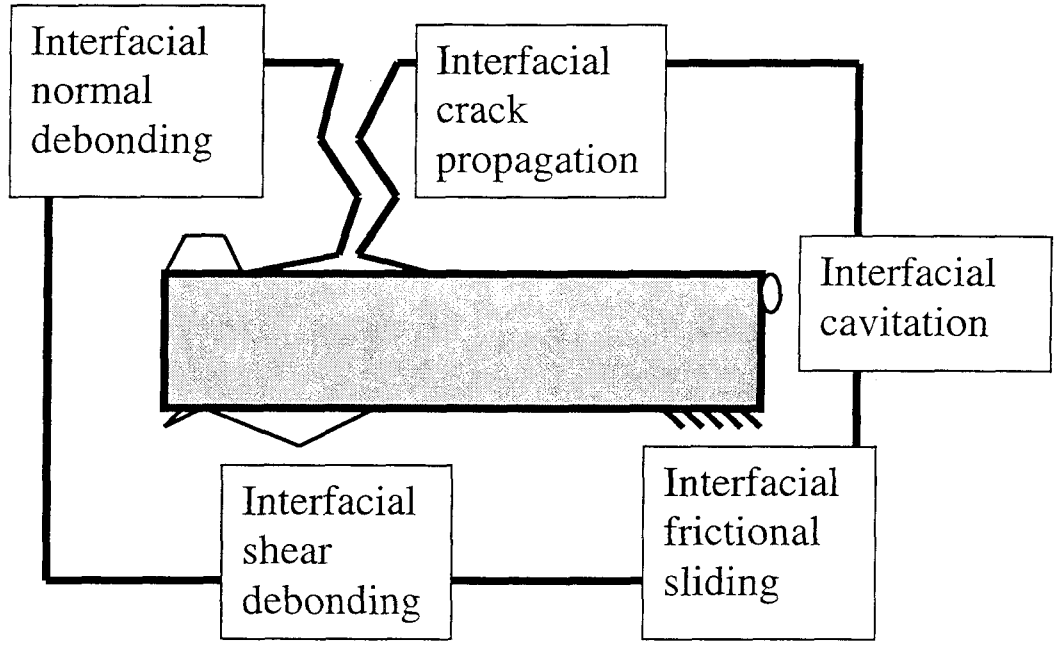

Fig. 1.12 Schematic illustration for a short fiber composite of (a) stresses near the interface, arising from an applied load and from differential thermal contraction, and (b) the various inelastic interfacial processes they initiate. Reproduced from ref. 33.

Interfacial diffusion also determine the reaction between the reinforcement and matrix.

The desired properties of the interface depend on the type of composite system. For polymer-based composites, the objectives are a high bond strength and a good resistance to environmental attack. In designing ceramic composites, the aim is usually to make the interface very weak, as the prime concern is in promoting energy dissipation at the interface so as to raise the toughness. For metal matrix composite, a strong bond is usually desirable, but there may be instances where inelastic processes at the interface can be beneficial. Furthermore, the need for control over chemical reactions between the constituents occurring during fabrication is important. Therefore, the methods to reduce the rates of growth of the interfaces are very important aspects of the development of useful composites.

1.3 METALLIC GLASS MATRIX COMPOSITES

Metallic glass ribbon has been used as a reinforcement in composite material because of its high strength and high strain limit. An amorphous metal ribbon reinforced resin-matrix composite was fabricated and mechanically tested by Strife et al.[35] These composites are found to have high strength and good fracture toughness, but poor fatigue resistance. Metallic glass ribbon has also been used as reinforcement in polymer and glass ceramic matrices.[36,37] The first metallic glass ribbon reinforced metal matrix composites were reported by Cytron.[38] $Ni_{60}Nb_{40}$ metallic glass ribbon was chosen as a reinforcement because

of its ductility and high crystallization temperature (650 °C). This metallic glass ribbon was hot pressed between wafers of superplastic aluminum alloy at 450-500 °C.

Metallic glass ribbon has also been used as a matrix. Usually the melt spinning technique is used to make composites in ribbon form. Adding tungsten carbide particles to $Ni_{78}Si_{10}B_{12}$ metallic glass ribbon during the melt-spinning process was done by Kimura et al.[39]

In addition to being used to fabricate particulate reinforced metallic glass ribbons, melt spinning process has been used to make discontinuous fiber reinforced composites.[40] However, the resulting fiber distribution was poor. Williford et al. described the technique to make continuous fiber reinforced metallic glass ribbons.[41] They arranged fibers in contact with the meniscus of molten metal protruding from the crucible orifice. The fibers were then drawn out along with the melt onto the moving substrate. The combination was chilled to form the composite. However, the best results were ribbons reinforced by a few tungsten wires. In addition, small dimension of these metallic glass ribbon composites limits a number of practical applications.

In this work, bulk metallic glasses were used as matrices reinforced with refractory ceramics, ductile metal particles, or short wires.[42] This was made possible by the use of recently reported multicomponent alloys that exhibits an extremely high glass forming ability. Bulk glassy material with thickness up to several cm could be produced, since they have low critical cooling rates. They usually are at deep eutectic composition. That means they have low melting

temperature. Accordingly, these alloys can be used in liquid-phase processing at lower temperature. This lowers the cost of processing and reduces the chemical interactions between the reinforcement and the glass. This makes for easy control of interfacial reactions. In addition, the low glass transition temperature decreases differential thermal stresses which arise between the reinforcement and the matrix during freezing upon cooling. Further, these alloys are stable against crystallization above the glass transition temperature as an undercooled liquid. This allows for the processing at even lower temperatures slightly above the glass transition, although higher pressures would be required due to the higher viscosity.

REFERENCES

1. W. Kurz, *Fundamentals of Solidification*, Transtec, Switzerland (1986).
2. R. Busch, Y.J. Kim and W.L. Johnson, *J. Appl. Phys.* **77**, 4039 (1995).
3. T.R. Anantharaman, in *Metallic Glasses: Production, Properites, and Applications* (edited by T.R. Anantharaman), Transtec, Switzerland (1984).
4. R. Busch, E. Bakke, and W.L. Johnson, *Materials Science Forum.* **235-238**, 327 (1997).
5. W. Klement IV, R.H. Willens and P. Duwez, *Nature*. **187**, 869 (1960).
6. F.E. Luborsky (ed.), *Amorphous Metallic Alloys*, Butterworth, London (1983).
7. M. Naka, K. Hashimoto and T. Masumoto, *J. Japan Inst. Metals*. **38**, 835 (1974).
8. A.J. Drehman, A.L. Greer and D. Turnbull, *Appl. Phys. Lett.* **41**, 716 (1982).
9. A. Inoue, T. Zhang and T. Masumoto, *Mater. Trans. JIM*. **31**, 425 (1991).
10. A. Inoue, T. Nakamura, N. Nishiyama and T. Masumoto, *Mater. Trans. Acta metall. Mater.* **41**, 915 (1993).
11. T. Zhang, A. Inoue and T. Masumoto, *Mater. Trans. JIM*. **32**, 1005 (1991).
12. A. Peker and W.L. Johnson, *Appl. Phys. Lett.* **63**, 2342 (1993).
13. Y.J. Kim, R. Busch, W.L. Johnson, A.J. Rulison and W.K. Rhim, *Appl. Phys. Lett.* **65**, 2136 (1994).

14. X.H. Lin and W.L. Johnson, *J. Appl. Phys.* **78**(11), 6514 (1995).

15. X.H. Lin, *PhD thesis,* California Institute of Technology; X.H. Lin and W.L. Johnson, *Mater. Trans. JIM.* **38**, 475 (1997).

16. H.A. Davis, *Rapidly Quenched Metals III,* B. Cantor (ed.), Metals, Soc., London (1978), Vol. 1, p.1.

17. A.J. Drehman and A.L. Greer, *Acta. Metal.* **32**, 323 (1984).

18. M.C. Lee, J.M. Kendall and W.L. Johnson, *Appl. Phys. Lett.* **40**, 382 (1982).

19. A. Inoue, T. Nakamura, T. Sugita, T. Zhang and T. Masumoto, *Mater. Trans. JIM.* **34**, 351 (1993).

20. A. Inoue, A. Kato, T. Zhang, S.G. Kim and T. Masumoto, *Mater. Trans. JIM.* **32**, 609 (1990).

21. A. Inoue, T. Zhang, N. Nishiyama, K. Ohba and T. Masumoto, *Mater. Trans. JIM.* **34**, 1234 (1993).

22. M. Ohring and A. Haldipur, *Rev. Sci. Instrum.* **42**, 530 (1971).

23. R. Pond and R. Maddin, *Trans. Met. Soc. AIME.* **245**, 2475 (1969).

24. R.B. Schwarz and W.L. Johnson, *Phys. Rev. Lett.* **51**, 415 (1983).

25. J.H. Holloman and D. Turnbull, *Prog. In Met. Phys.* **4**, 333 (1953).

26. D. Turnbull, *Solid State Physic, Vol. 3*, Academic Press, New York (1956).

27. J.F. Shackelford, *Introduction to Mat. Sci for engineers*, Macmillan Publishing, New York (1992).

28. D. Turnbull, *Contemp. Phys.* **10**, 473 (1969).

29. B. Chalmers, *Principles of Solidification*, Wiley & Sons, New York,

(1964).

30. J.W. Weeton, *Engineer 's Guide to Composite Materials*, American Society for Metals, Metals Park, OH (1987).
31. A.K. Dhingra, *J. Met.* **38**, 17 (1986).
32. A.P. Divecha, S.G. Fishman and S.D. Karmarkar, *J. Met.* **33**, 12 (1981).
33. T.W. Clyne and P.J. Withers, *An Introduction to Metal Matrix Composites*, Cambridge University Press, Cambridge (1993).
34. R.K. Everett, *Metal Matrix Composites Processing and Interface*, Academic Press, New York (1991).
35. J.R. Strife and K.M. Prewo, *J. Mat.Sci.* **17**, 359 (1982).
36. R.U. Vaidya and K.N. Subramanian, *J. Mat. Sci. L.* **9**, 1397 (1990).
37. R.U. Vaidya, C. Norris and K.N. Subramanian, *J. Mat. Sci.* **27**, 4957 (1992).
38. S.J. Cytron, *J. Mat. Sci. Lett.* **1**, 211 (1982).
39. H. Kimura, B. Cunningham and D.G. Ast, *Proc. 4th Int. Conf. On Rapidly Quenched Metals* (edited by T. Masumoto and K. Suzuki), 1385, Japan Instit. Metals, Sendai (1982).
40. P.G. Zielinski and D.G. Ast, *MRS Symposia Proc.: Rapidly Solidified Metastable Materials* (edited by B.H. Kear and B.C. Giessen), 189, Elsevier, New York (1984).
41. J.F. Williford and J.P. Pilger, US patent 3, 776, 297 (1973).
42. H. Choi-Yim and W.L. Johnson, *Appl. Phys. Lett.* **71**, 3808 (1997).

CHAPTER 2
SYNTHESIS AND CHARACTERIZATION OF BULK METALLIC GLASS COMPOSITES

2.1 PROCESSING A BULK METALLIC GLASS MATRIX COMPOSITES BY CASTING

This section describes a processing procedure for the successful use of a bulk glass-forming alloy as a matrix material for composites. In this work, I used three different compositions of bulk metallic glasses developed by Lin and Johnson as matrix materials.[1,2] The low critical cooling rate of these alloys allows amorphous metal matrix composites to be made in bulk form. The nominal compositions of the three alloys are $Cu_{47}Ti_{34}Zr_{11}Ni_8$ (Vit 101), $Zr_{52.5}Ti_5Al_{10}Cu_{17.9}Ni_{14.6}$ (Vit 105) and $Zr_{57}Nb_5Al_{10}Cu_{15.4}Ni_{12.6}$ (Vit 106). Ingots of alloys were prepared by arc melting a mixture of the elements having purity of 99.7 percent or better on a water cooled copper hearth under a Ti-gettered argon atmosphere. The weight loss of the samples during alloying was less than 0.1 percent.

Composites were fabricated with a wide variety of reinforcements using the technique described below. Ceramics such as SiC, WC, or TiC, and the metals W, Carbon Steel, or Ta were used as second phase materials. Volume fractions of particles ranged from 5 to 30 percent and the sizes of the particles

varied between 20 and 80 micrometers. Short tungsten wires and high-carbon steel wires with aspect ratio of 3 and volume fractions of 10 percent were also used. All particles and wires were treated by ultrasonic cleaning in a bath of acetone followed by the same procedure in a bath of ethanol. A mixture of the pre-alloyed metallic glass forming elements and second phase material was combined by induction melting the glass forming alloy together with the solid second phase material on a watercooled copper boat under a Ti-gettered argon atmosphere. The composite ingots were then remelted at temperatures ranging from 850-1100°C under vacuum in a quartz tube using an induction heating coil and then injected through a nozzle into a copper mold using high purity argon at 1 atm pressure. Fig. 2.1 illustrates the mold-casting apparatus. The copper mold has internal rod shaped cavities of 30 mm length, 3 mm diameter and strip shaped cavities of 30 mm length, 6mm width and 2 mm thickness.

Table 2.1 gives an overview of the various combinations of metallic glasses and reinforcements which have been processed and characterized. "A" stands for an amorphous matrix after processing; "X" stands for fully or partially crystallized matrix after processing. The diameter of short wires is 100 micrometers and aspect ratio is 3. All specimens are 3 mm diameter rods. From this table we can conclude that many metallic glass/reinforcement mixtures used in this work are very stable with respect to nucleation and growth of second phases under the processing conditions used here.

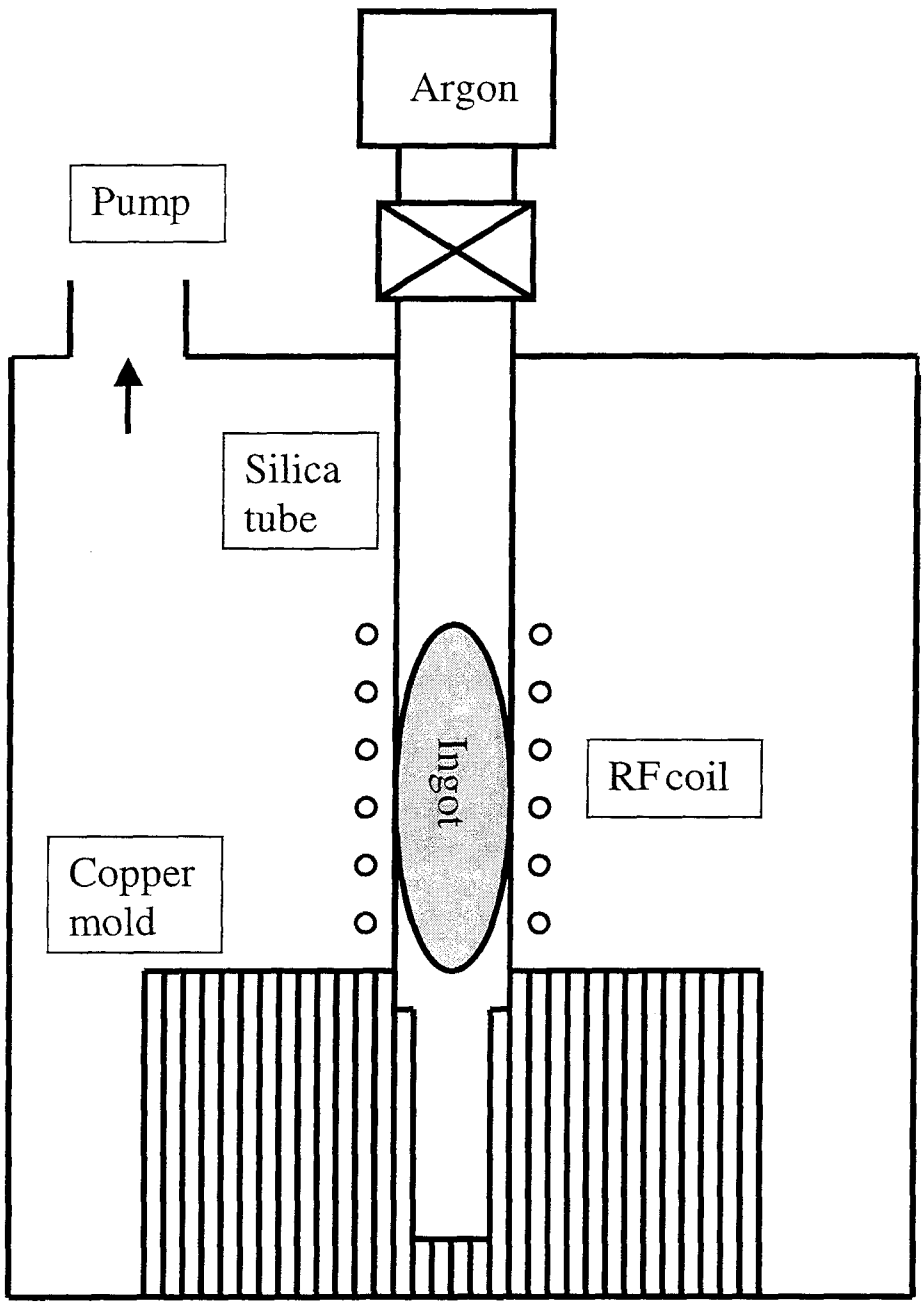

Fig. 2.1. Schematic of the mold-casting setup.

Reinforcement/matrix	Vit 101	Vit 105	Vit 106
10% SiC 50 μm	A	A	A
20% SiC 50 μm	A	A	A
30% SiC 50 μm	A	X	X
10% SiC 30 μm	A	X	A
20% SiC 30 μm	A	X	X
10% SiC 1 μm	X	---	---
10% TiC 20 μm	A	X	A
5% WC 30 μm	X	A	A
10%WC 30 μm	X	X	A
15% WC 30 μm	X	X	A
5% W 30 μm	A	A	A
10%W 30 μm	X	X	A
15%W 30 μm	X	X	A
5% W 12 μm	---	---	A
5% Ta 30 μm	---	---	A
10% Ta 30 μm	---	---	A
10%W short wire	A	A	A

Table 2.1 Lists of combinations between three different compositions of bulk metallic glasses and particles. Vit 101 is $Cu_{47}Ti_{34}Zr_{11}Ni_8$. Vit 105 is $Zr_{52.5}Ti_5Al_{10}Cu_{17.9}Ni_{14.6}$. Vit 106 is $Zr_{57}Nb_5Al_{10}Cu_{15.4}Ni_{12.}$

2.2 RESULTS OF MICROSTRUCTURE OF $Zr_{57}Nb_5Al_{10}Cu_{15.4}Ni_{12.6}$ BULK METALLIC GLASS COMPOSITES

2.2.1 X-Ray Diffraction, Differential Scanning Calorimetry and Optical Microscopy

Cross sections of cast strips and rods were examined by X-ray diffraction. A Simens D-500 diffractometer with a copper X-ray tube (for Kα radiation, λ= 0.1542 nm) was used for the results reported here. This apparatus uses a θ-2θ goniometer configuration for the sample and the X-ray detector to mechanically scan through a range of angles. For calibration, peaks from a silicon powder sample were measured and compared to tabulated values. Figure 2.2 shows the X-ray diffraction pattern of the Vit 106 matrix, the alloy reinforced with 10% WC and pure WC particles in one plot. The pattern of the composite shows diffraction peaks from WC particles superimposed on the broad diffuse scattering maxima from the amorphous phase. No considerable amounts of other phases are detected within the sensitivity limit of X-ray diffraction. Similarly, Figure 2.3 shows the patterns of Vit 106, the alloy reinforced with 10% SiC and SiC particles. Figures 2.4 and 2.5 show the patterns of Vit 106 reinforced with 10% W and Vit 106 reinforced with 10% Ta, respectively. In all four cases the X-ray diffraction patterns suggest that the Vit 106 matrix is amorphous after processing and quenching. The particles maintained their crystal structure. Since no significant peak shifts of the reflexes of the particles are observed, we can assume that no considerable amount of matrix atoms were dissolved into the particles.

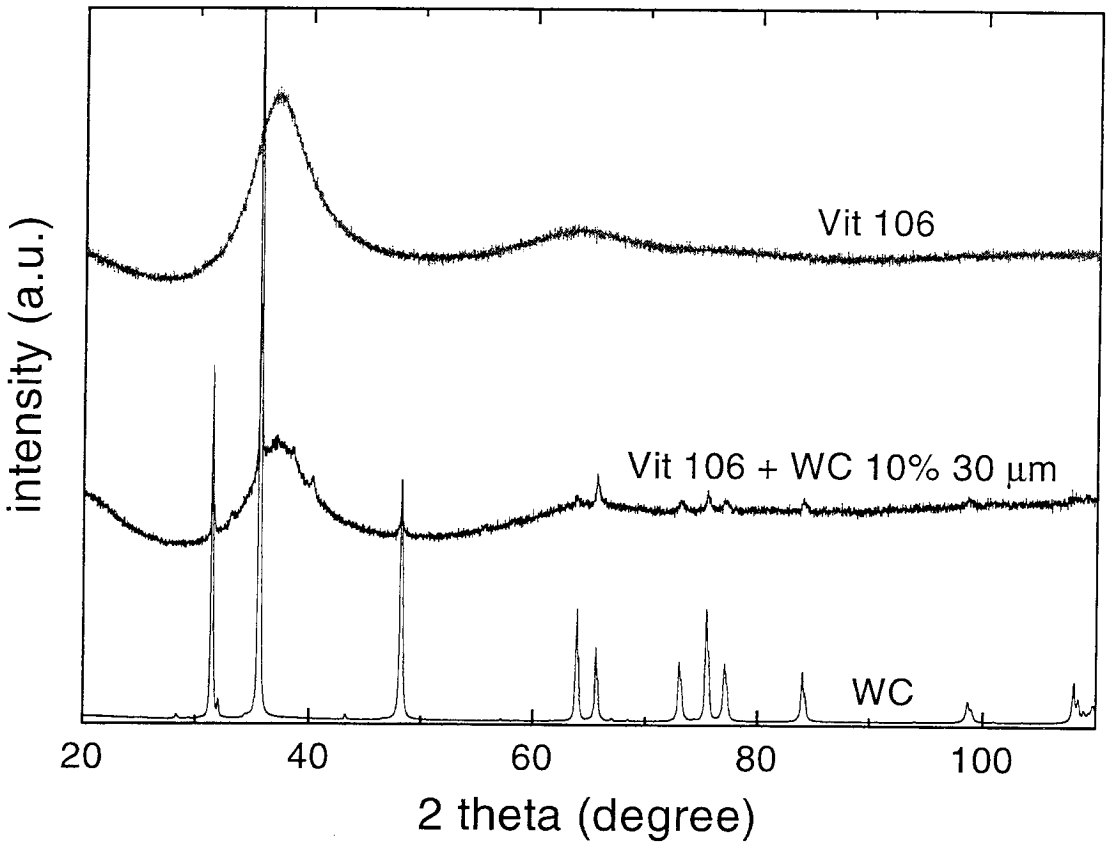

Fig. 2.2. X-ray diffraction patterns of the Vit 106 matrix, the alloy reinforced with 10% WC and pure WC particles. Vit 106 matrix is amorphous after processing and quenching. The particles also maintained their crystal structure.

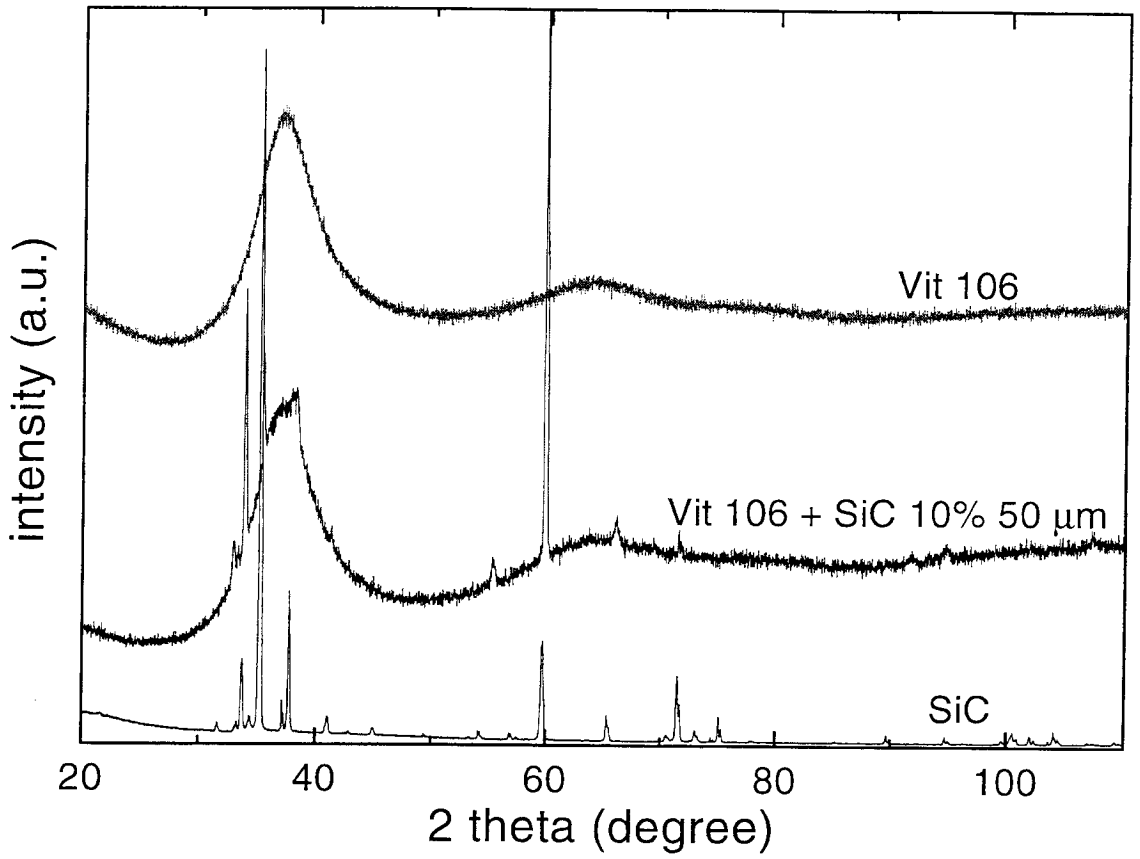

Fig. 2.3. X-ray diffraction patterns of the Vit 106 matrix, the alloy reinforced with 10% SiC and SiC particles.

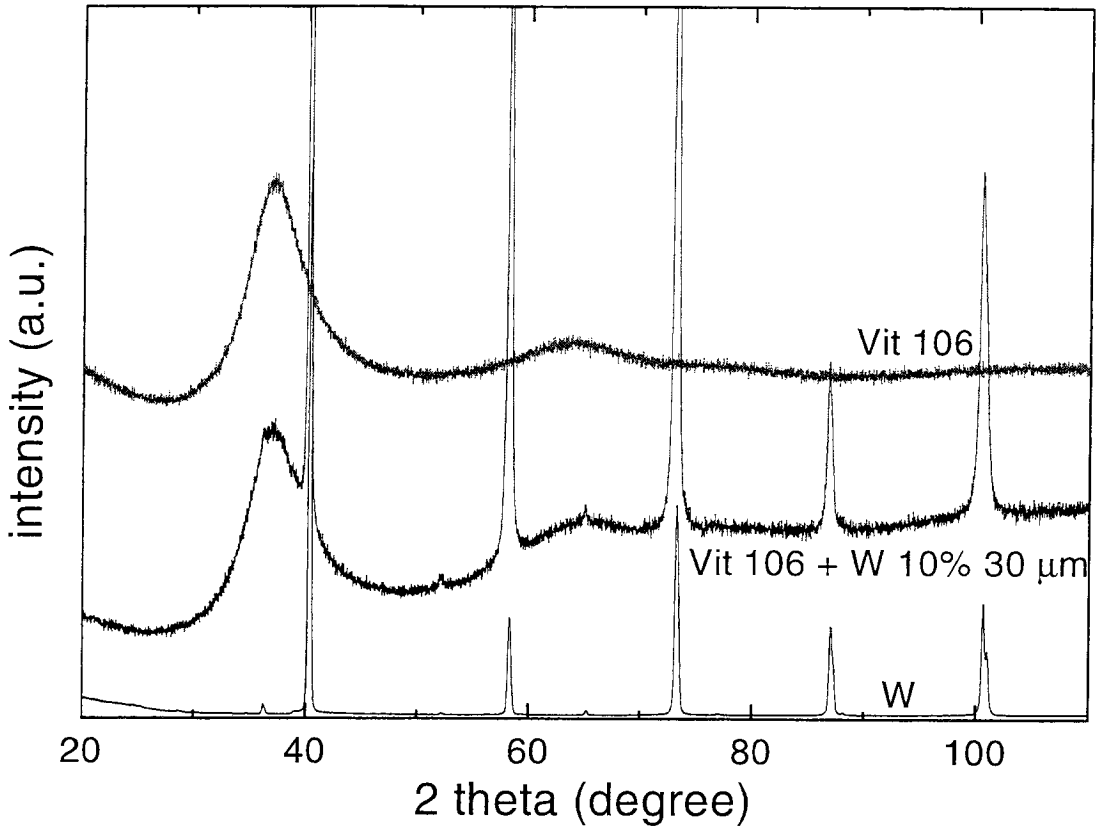

Fig. 2.4. X-ray diffraction pattern of the Vit 106 matrix, the alloy reinforced with 10% W and W particles.

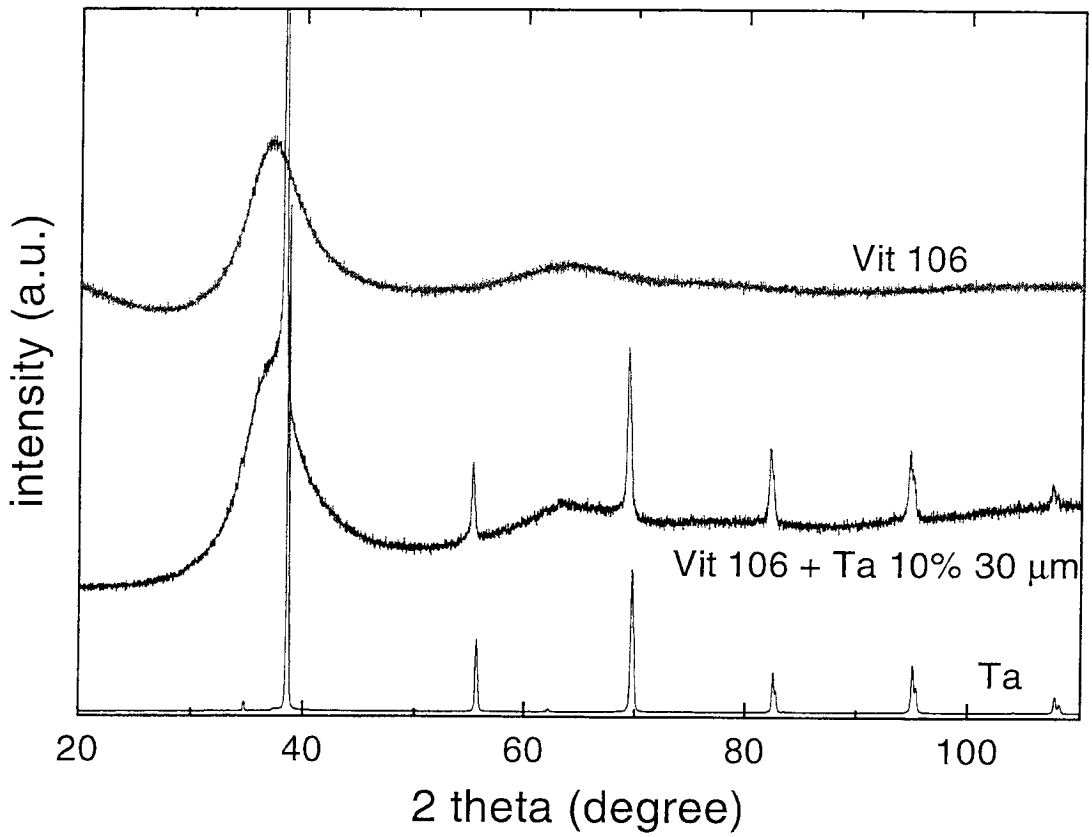

Fig. 2.5. X-ray diffraction pattern of the Vit 106 matrix, the alloy reinforced with 10% Ta and Ta particles.

The glass transition and crystallization of all samples was studied with a differential scanning calorimeter (Perkin-Elmer DSC 7). Different heating rates between 0.0167 and 3.33 K/s were used. The glass transition and the crystallization behavior of the amorphous matrix of the composites were investigated in DSC scans using various heating rates. Fig. 2.6 shows DSC scans of the pure amorphous Vit 106 and WC, SiC reinforced composites using a heating rate of 0.33 K/s. They exhibit an endothermic heat event characteristic of the glass transition followed by two characteristic exothermic heat releases indicating the transformation from the metastable undercooled liquid state into the crystalline compounds. T_g is defined as the onset of the glass transition temperature. T_{x1} is the onset temperature of the first crystallization event. The value ΔT_x, which is defined as T_{x1}-T_g, is referred to as the supercooled liquid region. Based on the DSC scans in Fig. 2.6, it is observed that the addition of WC particles into the Vit 106 produces no discernible change in either T_g or T_{x1}. Contrarily, the addition of SiC particles into the Vit 106 produces an extension of the supercooled liquid region. A similar effect will be presented in Chapter 4, when SiC was introduced in the $Cu_{47}Ti_{34}Zr_{11}Ni_8$ bulk metallic glass forming liquid. Fig. 2.7 shows the DSC scans of Vit 106 as well as of the W and Ta reinforced composites. It is observed that the addition of W or Ta into the Vit 106 does not produce any change in thermal behavior of Vit 106. We can conclude that in no case the introduction of the particles negatively affects the thermal stability of the amorphous Vit 106 matrix. In the case of SiC it is even enhanced.

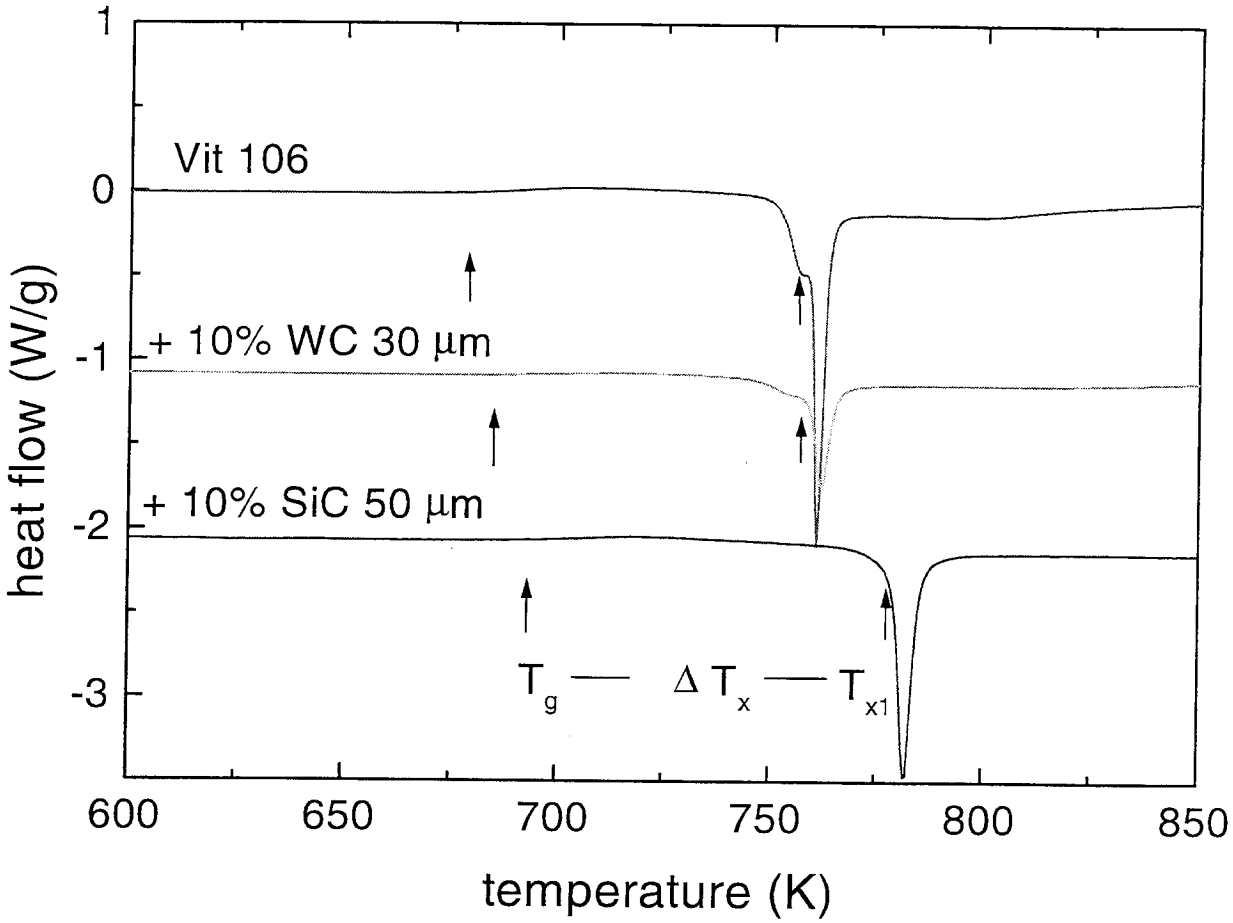

Fig. 2.6. DSC thermogram (heating rate of 0.33 K/s) of the Vit 106 and WC, SiC reinforced composites for Vit 106. The width of the supercooled liquid region, ΔT_x, is the temperature interval between onset of the glass transition, T_g, and the onset of primary crystallization, T_{x1}. In no case the introduction of the particles negatively affects the thermal stability of the Vit 106 matrix.

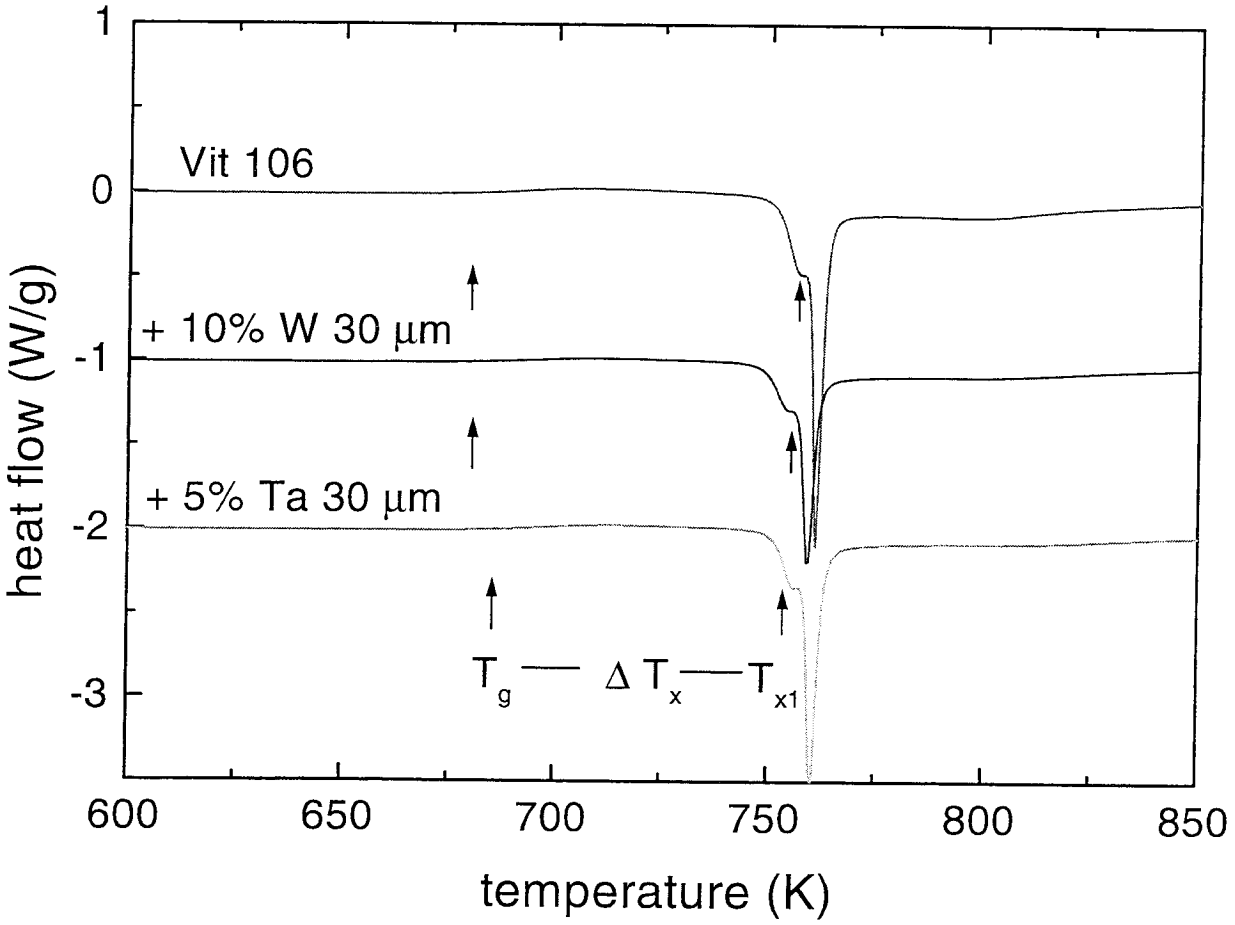

Fig. 2.7. DSC thermogram (heating rate of 0.33 K/s) of the Vit 106 and W, Ta reinforced composites for Vit 106.

The particle distribution in the composite specimens was investigated by optical microscopy. Figure 2.8 shows the optical micrographs of the uniformly distributed WC particles in the metallic matrix. Similarly, Fig. 2.9(a) and (b) show the optical micrographs of the SiC and W particles in the Vit 106 matrix. The matrix appears uniform and free of heterogeneity in all the three optical micrographs.

2.2.2 Interfaces Between Matrix and Particles

In selected samples the interfaces between particles and matrix were examined by electron microprobe, scanning electron microscopy (SEM). Electron microprobe is one of the most powerful instruments for the microanalysis of materials. The primary reason for the electron microprobe's usefulness is that compositional information, using characteristic x-ray lines, with a spatial resolution of the order of 2 μm can be obtained from a sample. SEM that is combined with the electron microprobe gives high-resolution images of details from millimeters to microns in size. In general, backscatter images contain contrast effects from both surface topography and the average atomic number of the material. Cross sections of the samples analyzed for electron microprobe and SEM were polished down to 0.25 μm diamond grit.

Figure 2.10 shows an SEM backscattering image of a WC particle in the Vit 106 matrix. At the interface a layer with a thickness of about 1 μm had formed during processing. According to microprobe analyses, this layer consists of ZrC with small amounts (below 1 at. %) of the other matrix elements. Throughout the entire matrix we find a W concentration of approximately 0.25

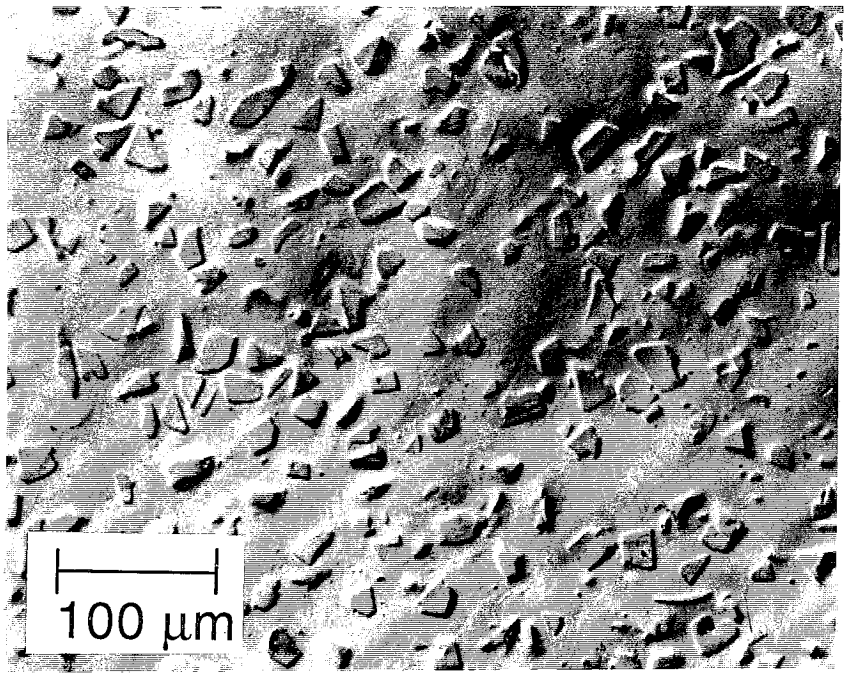

Fig. 2.8. Optical micrographs of polished surface of $Zr_{57}Nb_5Al_{10}Cu_{15.4}Ni_{12.6}$ alloy (Vit 106)/WC composites.

(a)

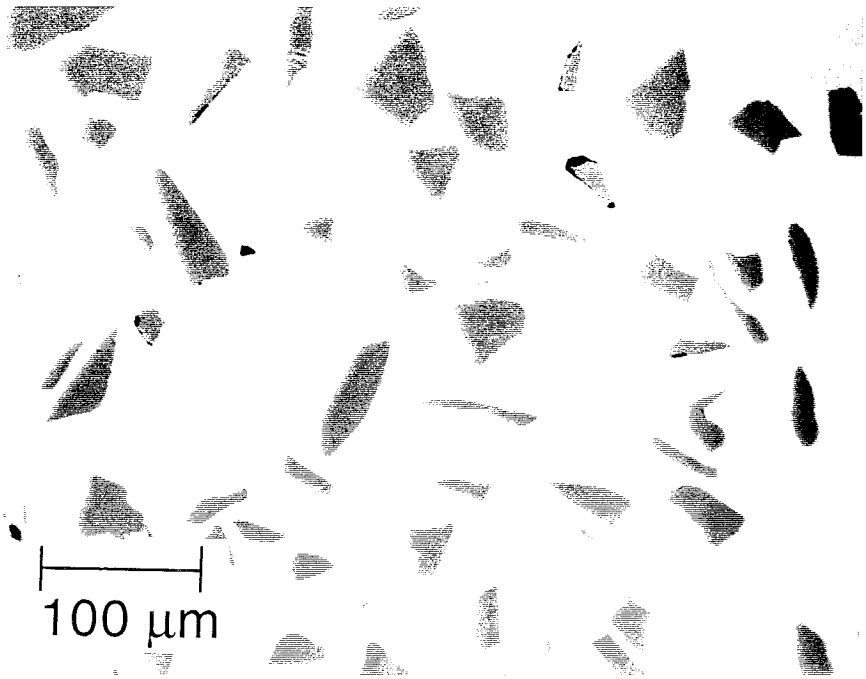

(b)

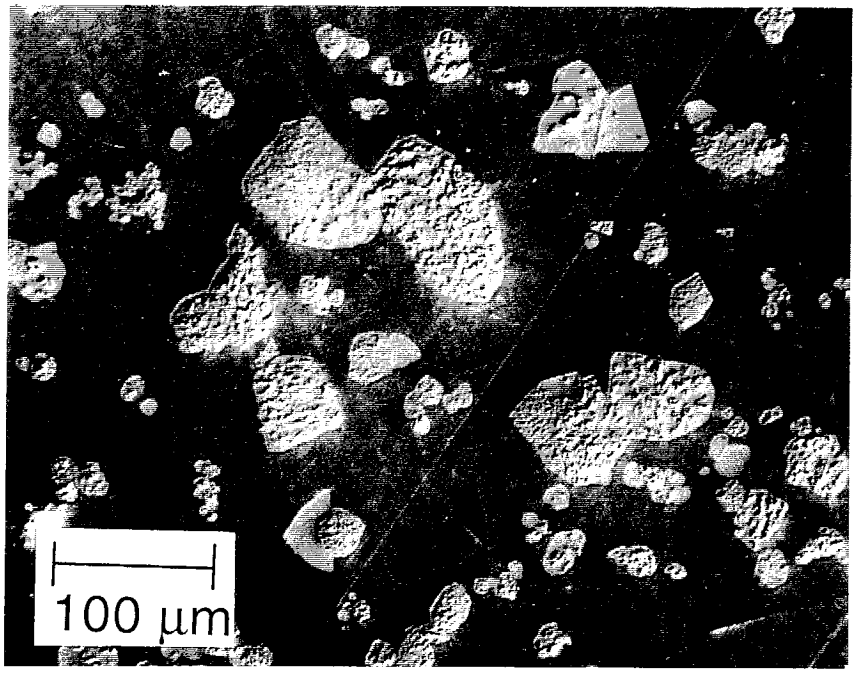

Fig. 2.9. Optical micrographs of polished surface of (a)Vit 106/SiC composites and (b)Vit 106/W composites, showing a uniform distribution of particles in the Vit 106 matrix.

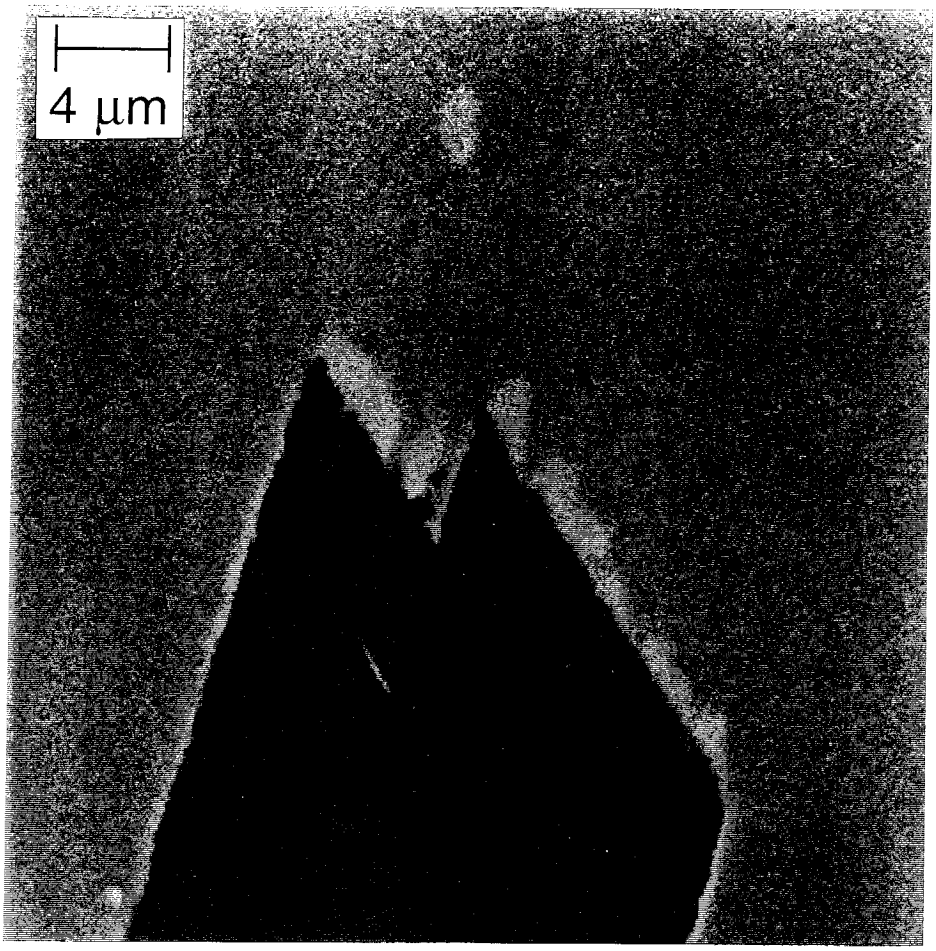

Fig. 2.10. SEM backscattering image of a WC particle in the Vit 106 matrix. The reaction layer of ZrC with a thickness of 1 μm was formed around a WC particle. Throughout the entire matrix, a W concentration of 0.25 at. % was found.

at. %. This indicates that during the growth of the ZrC layer at the interface between WC and ZrC, the W is replaced by Zr. Subsequently the W diffuses through the ZrC layer into the matrix. Because of the high diffusivity in the molten matrix during processing, the W is evenly distributed.

For the SiC particles in the Vit 106 matrix a similar reaction is observed. Microprobe analyses show that the matrix of this composite contains 0.9 at. % Si. As shown in Fig. 2.6, the matrix of this composite is thermally more stable above the glass transition than the pure Vit 106. The microprobe analyses of the interface between matrix and particles suggest that also in this case a ZrC layer has formed.

To investigate this further, the interface between SiC particle and matrix was imaged by TEM. TEM studies of the composite microstructure offer great advantages. The magnification capabilities are usually much greater than other forms of microscopy. Thus, we can image the interfacial region between the reinforcement and matrix in much finer details. All the TEM work presented here was performed on a Philips EM430 electron microscope at 300 keV. It is also equipped with a EDAX 9900 energy-dispersive x-ray analyzer.

Figure 2.11 shows the dark field (DF) TEM image as well as the diffraction pattern of the imaged region. The diffraction pattern shows the (large) reflexes caused by the single SiC grain, the diffuse amorphous ring, as well as a series of rings that can be clearly identified as the reflexes corresponding to ZrC. One of the latter reflexes was used to produce the dark field image. From the DF image we can therefore conclude that a ZrC layer had formed at the interface. This is also confirmed by energy dispersive x-ray analysis (EDAX) of the layer

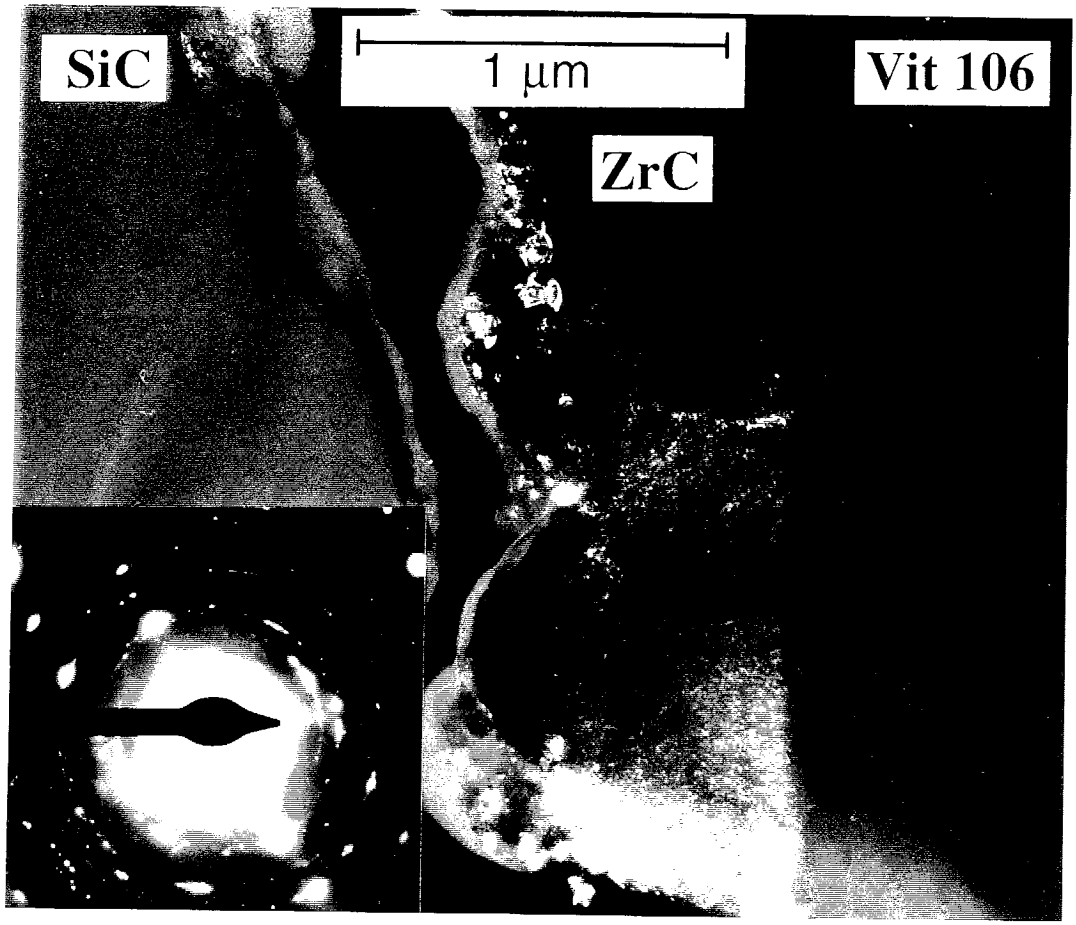

Fig. 2.11. Dark field TEM of interfacial region between a SiC particle and the Vit 106 matrix. The diffraction pattern of the imaged region is also shown. A ZrC layer had formed at the interface. The inferface between the SiC and ZrC is mechanically very weak. The inferface between the Vit 106 matrix and the ZrC appears to be strong.

in the scanning mode of the TEM. It is worth noting that the interface between the SiC and the ZrC is mechanically very weak. At all reacted layers that were looked at, this interface was broken. This effect was observed in any cases, whether the sample was prepared by ion milled or by microtomy. The interface between the amorphous matrix and the ZrC, in contrast, appears to be rather strong.

Interfaces between Vit 106 and W particles were also studied. On the scale of the SEM image, no reaction layer can be detected as shown in Fig. 2.12. The microprobe analysis, however, reveals that W diffuse into the matrix. An average concentration of 0.4 at. % of W is found in the matrix. Traces of Cu and Ni of about 0.3 at. % are detected in the W particles. To investigate the interface between the W particle and the matrix more closely, TEM work was performed. In Fig. 2.13, the DF TEM image of the interface between the W particle and the matrix is shown. It also contains the diffraction patterns of the W particle, the amorphous matrix and the interface, respectively. At the interface between the matrix and the W particle, crystals with a diameter of 50-100 nm have formed. According to qualitative EDAX analyses, the compositions of these crystals are closed to the average matrix composition, with the exeption of the Ni. The Ni signal is reduced to about 50% compared to the matrix suggesting that the crystals are considerably depleted of Ni. The crystal structure of the nanocrystals could not be determined yet.

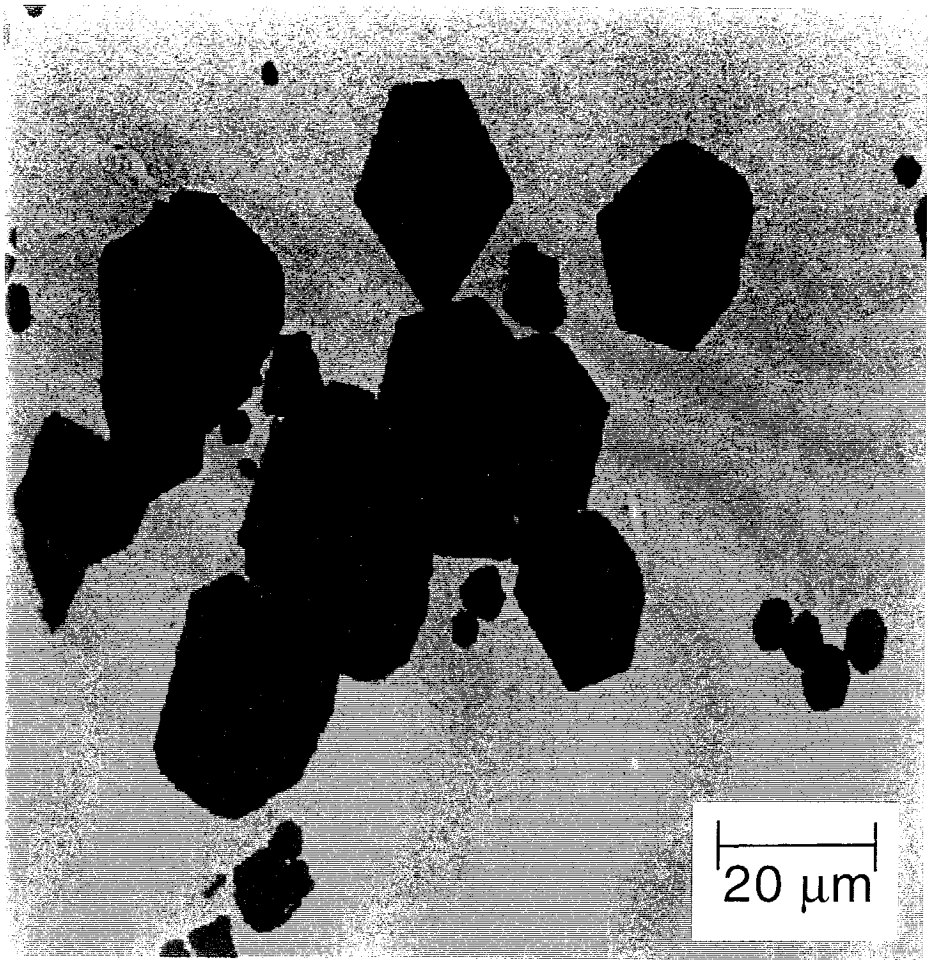

Fig. 2.12. SEM backscattering image of a W particle in the Vit 106 matrix. No reaction layer can be detected on the scale of the SEM image.

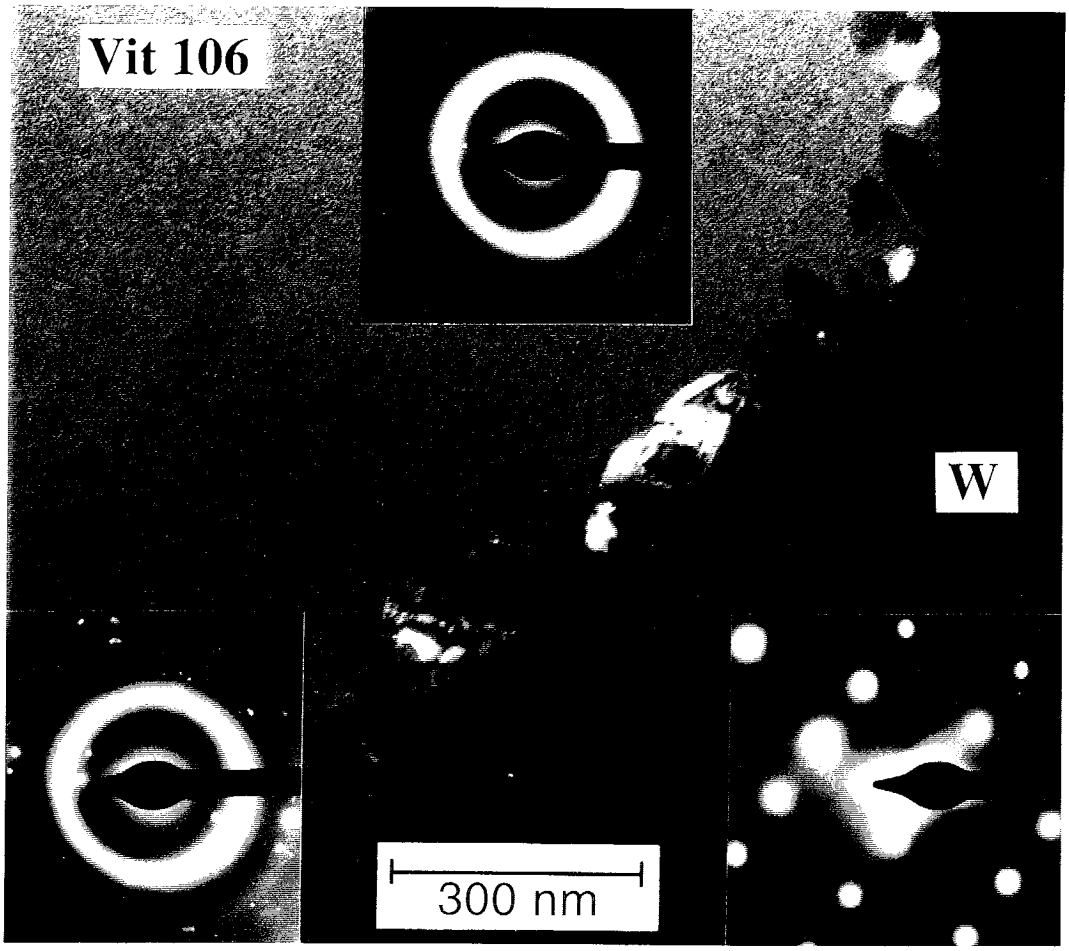

Fig. 2.13. TEM of interfacial region between W particle and Vit 106 matrix. The dark field TEM image of the interface is shown with the diffraction patterns of the W particle, the amorphous matrix and the interface, respectively. Crystals with a diameter of 50-100 nm have been found at the interface.

2.3 DISCUSSION

The success in making composites with an amorphous matrix is somewhat surprising. According to early studies of crystal nucleation, such second phase crystalline solid additions to the glass forming melts should tend to act as catalytic sites for heterogeneous crystal nucleation and growth.[4] The absence of heterogeneous nucleation of crystalline phases in the metallic glass induced by interfacial contact with the reinforcement is related to crystallization kinetics in these glass forming melts. It has been shown, for example, that crystallization in these glasses is sluggish as evidenced by critical cooling rates of the order of 10-100 K/s.[5-7]

The synthesis methods used in this work are effective and simple. Particles were introduced directly into the metallic glass during induction melting. This method has the advantage of mixing the particles and glass forming liquid through radio frequence stirring of the melt. Wetting of particles by the molten metal is observed to occur spontaneously. We found from this study that although Vit 105 is the best glass former among the three alloys reported on the paper (as assessed by earlier studies of critical cooling rates [1,2]), Vit 106 is the most processable matrix phase for fabricating composites containing a completely glassy matrix. The reduced glass transition temperature (T_{rg}), the ratio of glass transition temperature and liquidus temperature of the crystalline alloy, has often been cited as a critical parameter determining the glass forming ability of metallic alloys. High values of T_{rg} are associated with

good glass forming ability. In the current context we know that the T_{rg} of Vit 105 is 0.638 while the T_{rg} of Vit 106 is 0.620.

The maximum volume fraction of particles that could be introduced into the glassy alloys by the present casting methods was 30 percent. A high speed of injecting molten alloys into the mold is necessary to achieve a high enough cooling rate to avoid crystallization of the matrix during casting. Adding a higher volume fraction of solid particles to the liquid alloy increases the viscosity of the mixture and lowers the injection speed achievable during casting, thus limiting the volume fraction of particles that can be added to the glass matrix. Table 2.1 also shows processability versus particle sizes. A given volume fraction of small particles have more interfacial area between the particles and glass forming alloy than the same volume fractions of larger particles. This enhances chemical reaction between the particles and the glass matrix. Dissolution or reaction of an excessive amount of the reinforcement phase with the metallic glass matrix changes the composition of the metallic glass in a manner, which removes the composition from the optimum glass forming range. Interfacial reactions and dissolution of reinforcement into the melt are ultimately believed responsible for degradation of the glass forming ability of the matrix.[8] On the other hand, one can improve the glass forming ability of the matrix by interdiffusion between the reinforcement and the metallic glass matrix. These factors will be discussed in Chapter 4.

In this investigation, we used either carbides or pure refractory metals as reinforcements. In the case of the carbide particulates, a ZrC layer is formed at the interface during processing, due to the larger heat of formation for ZrC compared

to WC and SiC. The metal (W) or semiconductor (Si) atom is released into the matrix. In the case of the Ta and W particulates, the metals are simply dissolved into the liquid matrix during processing.

After the liquid/particulate mixtures are cooled in the mold casting process, no crystallization is observed at the ZrC/Vit 106 interface, indicating that the ZrC interface does not act as a heterogeneous nucleation site (Fig. 2.11). At the W/Vit 106 interface, in contrast, crystallization of matrix material is observed. Nanocrystals with a composition not far from the matrix composition have formed during the cooling process. This can be either a result of heterogeneous nucleation at the W/Vit 106 interface, or the glass forming ability of the matrix in the vicinity of the tungsten can be reduced due to the enhanced W concentration (in the W concentration gradient) close to the particle compared to the small tungsten concentration in most of the matrix of less than 0.5 at.%.

From the DSC studies it is clear that in none of the composites the thermal stability of the matrix after reheating into the supercooled liquid is reduced. The extension of the supercooled liquid region did not change for WC, W, and Ta. In the case of the SiC particulates the glass forming ability was even improved.

The calorimetric studies were used to calculate the activation energies of crystallization for the particulate reinforced Vit 106 composites. By measuring the peak positions for primary crystallization in Fig. 2.6 and 2.7 at different heating rates, it is possible to determine the activation energies for the reaction by the Kissinger method[9], i.e., from the slopes of the curves of $\ln((\partial T/\partial t)/T_p^2)$ against $1/T_p$, where T_p is the peak temperature and $\partial T/\partial t$, the heating rate. These plots are presented in Fig. 2.14 for Vit 106 and with the different reinforcements.

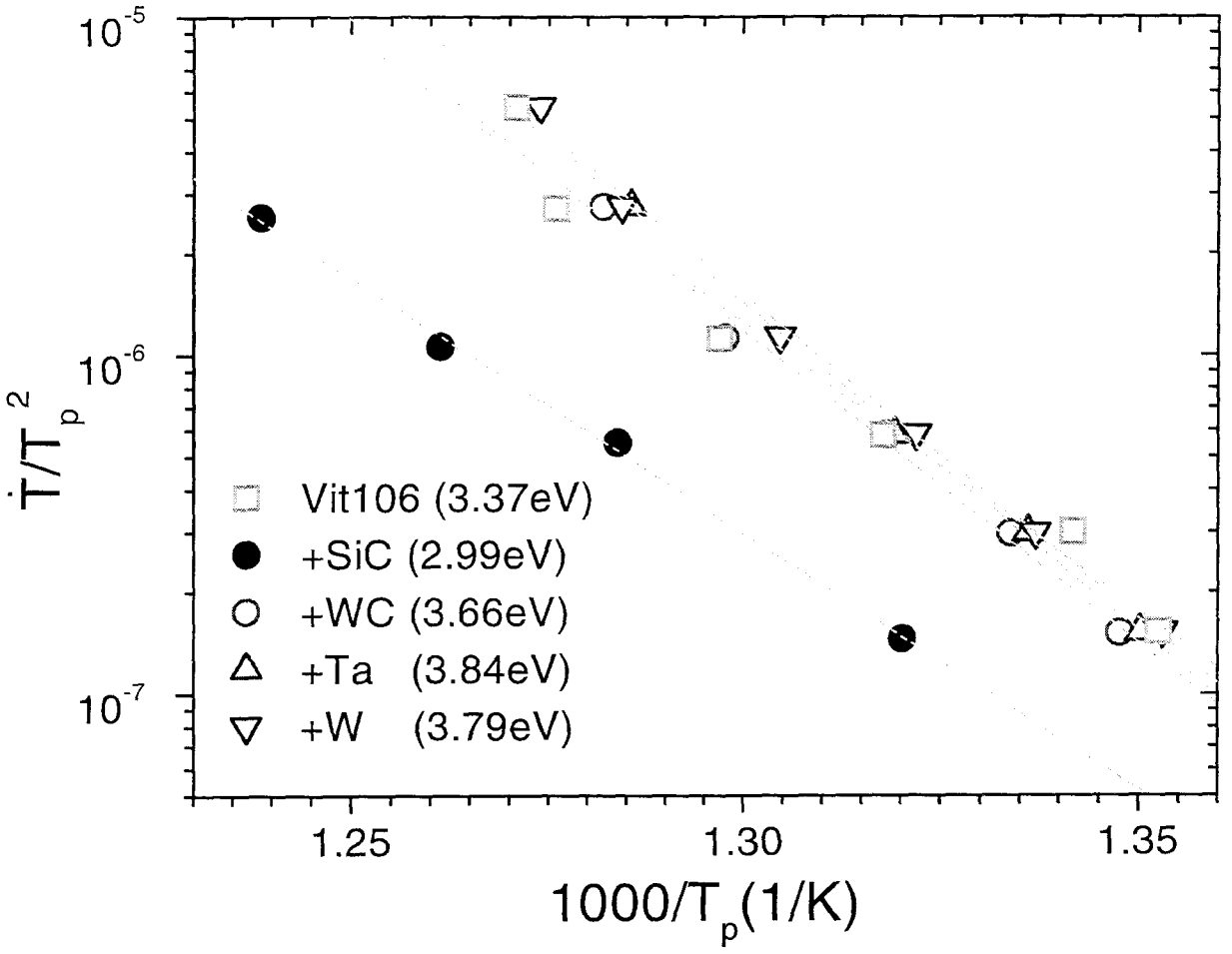

Fig. 2.14. Kissinger plots obtained after heating the composites with different heating rates. The activation energy for crystallization does not change significantly after adding the different particles consisting of W, Ta or Si into the glass matrix, respectively.

The plot reveals that there is no significant change in activation barrier when adding the different particles consisting of W, Ta or Si into the glass matrix respectively.

2.4 CONCLUSIONS

According to the present study, it has been proven that adding second phase crystalline materials into bulk metallic glass forming melt does not significantly degrade the bulk glass forming ability of the matrix alloy. The recent development of extremely stable bulk metallic glasses has made it possible to fabricate such composites. A variety of reinforcement materials have been added into the metallic glass matrix without inducing crystallization. Utilization of a relatively low maximum processing temperature prevents excessive reaction between the particles and glass matrix, thus allowing one to retain the excellent glass forming ability of the matrix.

The composites were characterized with respect to their structure, microstructure and thermal stability. In all cases the metallic matrix retained the amorphous state after adding up to 30 vol. % of particles. The thermal stability of the matrix did not deteriorate after adding the particles. In the case of SiC the matrix became even more robust with respect to crystallization. At the interfaces between the matrix and the WC or SiC particles, ZrC layers formed. W and Si diffused into the matrix, repectively. During solidification no heterogeneous nucleation is observed at the interface between ZrC and matrix. At the interface between W and the matrix, a thin layer of nanocrystals is observed after cooling the liquid/particulate mixture. When reheating the

composites into the supercooled liquid region of the matrix, no considerable reduction in crystallization temperature and activation energy for crystallization has been observed. This suggests that heterogeneous nucleation at the interfaces, if it occurs at all, does not considerably affect the crystallization of the entire matrix.

REFERENCES

1. X.H. Lin and W.L. Johnson, *J. Appl. Phys.* **78**, 6514 (1995).
2. X.H. Lin, Ph.D. thesis, California Institute of Technology; X.H. Lin and W.L. Johnson, *Mater. Trans. JIM.* **38**, 475 (1997).
3. J.I. Goldstein, *SEM and X-ray Microanalysis*, Plenum Press, New York, (1981).
4. D. Turnbull, *Contemp. Phys.* **10**, 473 (1989).
5. A. Inoue, T. Zhang, and T. Masumoto, *Trans. JIM.* **31**, 425 (1990).
6. T. Zhang, A. Inoue, and T. Masumoto, *Trans. JIM.* **32,** 1005 (1991).
7. A. Peker and W.L. Johnson, *Appl. Phys. Lett.* **63**, 2342 (1993).
8. R.B. Dandliker, Ph.D. thesis, California Institute of Technology (1997).
9. H.E. Kissinger, *Anal. Chem.* **29**, 1702 (1957).

CHAPTER 3
MECHANICAL PROPERTIES OF BULK METALLIC GLASS MATRIX COMPOSITES

3.1 INTRODUCTION

The mechanical response of a material under the external forces can be categorized into two responses: elastic and plastic. The elastic response is that the material recovers its shape instantaneously when the load is released. Almost all classes of solids also exhibit, at least over a certain temperature range, nonlinear and time-dependent elasticity, which is called viscoelasticity. The plastic response is that the material deforms permanently.

The deformation response of metallic glasses as affected by applied stress and temperature is illustrated in the schematic deformation map of Fig. 3.1. Metallic glasses behave in a linear elastic response in low stress levels and low temperatures. At higher temperatures, the behavior becomes dominated by the viscoelastic response. The viscoelasticity of metallic glasses is caused by recoverable atomic readjustments occurring in the presence of an applied stress. Metallic glasses deform plastically before fracture at high stresses even at low temperatures. The plastic response occurs in two regimes.[2] At high temperatures and low strain-rates the deformation is 'homogeneous' while at lower temperatures and higher strain-rates it becomes 'inhomogeneous'.

Homogeneous flow results in uniform deformation by which each volume element of the metallic glass contributes to the strain. Homogeneous flow occurs

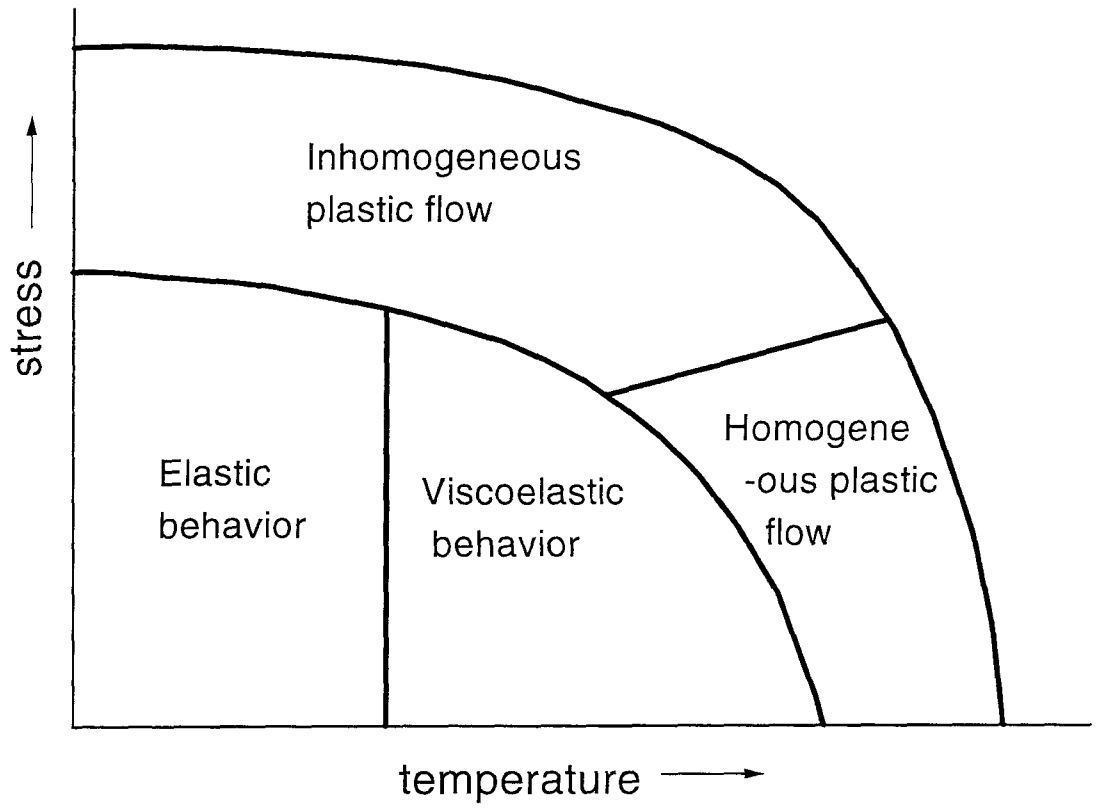

Fig. 3.1. A schematic deformation mechanism diagram for metallic glasses. Reproduced from ref. 2.

at low stresses and high temperature and is measured in stress relaxation tests. Since metallic glasses are in a thermodynamically unstable state, they continuously change their structure to lower their free energy. This structural relaxation affects all the physical properties, but most strongly the atomic transport properties.

Inhomogeneous flow is much less sensitive to structural relaxation. This deformation is localized in discrete, thin shear bands. Inhomogeneous flow occurs at high stresses and low temperature and is observed in tensile tests, compression tests, hardness tests and cold working processes such as rolling and wire drawing.

In this work, the inhomogeneous flow that is observed in compression and tension tests performed on metallic glasses and metallic glass matrix composites will be emphasized and examined.

3.1.1 Failure Mode of Metallic Glasses

Metallic glasses deform by highly localized shear flow. This inhomogeneous plastic flow is accompanied by the formation of shear deformation bands on the specimen surfaces. Shear bands are always oriented along a direction very close to the direction of maximum shear stress. In compression tests and tensile tests, the normal to the shear band has an angle close to 45 degrees to the loading axis. Final fracture occurs through a singular intense shear band, which develops over the entire cross section of the specimen.

There have been many approaches to explain the nature of the plastic process and how it propagates. Polk and Turnbull have suggested that

deformation of metallic glasses below their glass transition temperature could form a more compositional disordered structure.[3] Since this creates a reduced apparent viscosity, it leads to a localized plastic deformation. Pampillo reported a preferential etching effect on shear bands on a metallic glass which gives some support to Polk and Turnbull's suggestion that plastic deformation may form a more disordered structure.[4] The preferential etching susceptibility of shear bands means that the chemical potential within the bands has been changed with respect to the rest of the material. The structural change leading to this effect is the reduction of short range order in the shear band. Besides this, as suggested by Spaepen and Turnbull, dilatance which is probably associated with plastic shear strain also contribute to the weakening across sheared planes of metallic glasses.[5] The shear viscosity should be lowered in regions which are dilated by stress concentrations. Such a marked lowering of viscosity with dilatation would be in accordance with the free volume model for transport, as developed by Cohen and Turnbull.[6] A local dilatancy induces a greater local free volume that serves to catalyze localized flow and leads to formation of a shear band. Further, the difference in volume between the material within a formed shear band and the undeformed material adjacent to it leads to a stress concentration at the interface between these regions. This stress concentration is large enough to propagate the band at a stress level less than that required forming a second band.

In addition, Leamy, Chen and Wang suggested that fracture is initiated by adiabatic shear.[7] They suppose that the plastic zone becomes heated to temperatures exceeding the glass temperature by adiabatic release of the

deformation energy. Bruck, Rosakis and Johnson reported temperature increases due to adiabatic heating occur only after the onset of inhomogeneous deformation.[8] They also found temperatures near the melting point of Zr-Ti-Cu-Ni-Be alloys may be approached within shear bands after the specimen has failed.

The fracture surface morphology of the metallic glasses is called 'vein' pattern. The vein pattern might be produced by collision of cracks nucleated at different spots due to the reduction in stress concentration produced when two cracks meet each other and to local heating of the thin slab of material left in between.[9] There are also tributary veins, which merge into the main vein and point towards the crack nucleation site. The formation of tributary vein is thought to be due to an instability of the crack front. The instability which leads to the formation of these tributary veins into the viscous medium is the Taylor instability.[10] This instability occurs when a viscous fluid is driven forward by another fluid of smaller viscosity. The interface between the fluids becomes unstable and fingers from the less viscous fluid penetrate into the more viscous one. The main vein pattern and tributary veins of fracture morphology of metallic glasses will be given below.

3.1.2 Objectives of Making Bulk Metallic Glass Matrix Composites

Bulk metallic glasses have excellent mechanical properties such as high yield strength (~2 GPa) and a high elastic strain limit (~2%) combined with relatively high fracture toughness, fatigue and corrosion resistance.[11-13] They are also ductile when the mechanical constraint is such that catastrophic instability is

avoided, e.g., in uniaxial compression[14] , bending[15], rolling.[16] However, they have little ductility in tension. Although the local plastic strain in a shear band is quite large, the overall strain is determined by the number of shear bands. In a tensile test, only a few shear bands are active, which makes the stress-strain curve similar to that of a brittle material. But, the fracture process terminates the flow as a ductile one because it occurs along a shear band, not normal to the tensile axis, and forms a vein pattern on the fracture surface, which is associated with extensive plastic flow. The lack of tensile ductility is an important drawback in many applications. One way to address this problem is to reinforce the glass. Those reinforcements include ceramics such as SiC, TiC, or WC and the metals W or Ta. Improvements of the tensile ductility and fracture toughness could be achieved by hindering propagation of shear bands and encouraging the formation of multiple shear bands due to the existence of the second solid crystalline phase.

In this chapter, measured mechanical properties of unreinforced metallic glasses and metallic glass matrix composites will be reported and compared. The large influence of reinforcing particles on the mechanical properties of the metallic glasses also will be presented and discussed.

3.2 EXPERIMENTAL METHODS

Ingots of $Zr_{57}Nb_5Al_{10}Cu_{15.4}Ni_{12.6}$ (Vit 106) metallic glass was prepared by arc melting a mixture of the elements having purity of 99.7% or better. Then a mixture of the pre-alloyed metallic glass forming elements and second phased material was induction melted on a water-cooled copper boat under a 800 mbar Ti-gettered

argon atmosphere. Volume fractions of particles ranged between 5 and 30 percent and the sizes of the particles varied between 3 and 50 μm. The composite ingots were remelted at temperatures ranging from 850 to 1100 °C under vacuum in a quartz tube using an induction heating coil and then infected through a nozzle into a copper mold using high purity argon at 1 atm pressure. The copper mold had internal rod shaped cavities of 30 mm in length and 3 mm in diameter and strip shaped cavities of 35 mm in length, 6 mm in width and 2 mm in thickness. The rods, which were used in compression tests, were cut to a length that provided an aspect ratio of 2 using an Isomet saw equipped with a diamond blade. The cut rods were mounted in a collet holder which was clamped in a V-block and the ends of the rods were ground flat and perpendicular to the loading axis. The final polish was done using 600 grit SiC wet-dry sandpaper. Clamping the polished rod in a micrometer and examining the gap at 40x magnification using a binocular microscope checked the flatness and perpendicularity of the faces. The strips were ground into the dogbone-shaped specimens, which were used in tension tests. The gage length of each tensile specimen was 12 mm. It had a thickness of 1 mm. Fig. 3.2 represents a photograph of the as prepared compression and tension samples.

Quasi-static compression and tension tests were performed on an Instron 4204 load frame, at a strain rate of 0.02 inches per minute. The test specimen was compressed between tungsten carbide platens in a loading fixture designed to guarantee axial loading. The ends of the compression samples were lubricated to prevent "barreling" of the sample. The tensile specimens were held in threaded grips, which are fitted with a universal joint at their point of attachment to insure axial loading. A calibrated extensometer was used to measure strain in

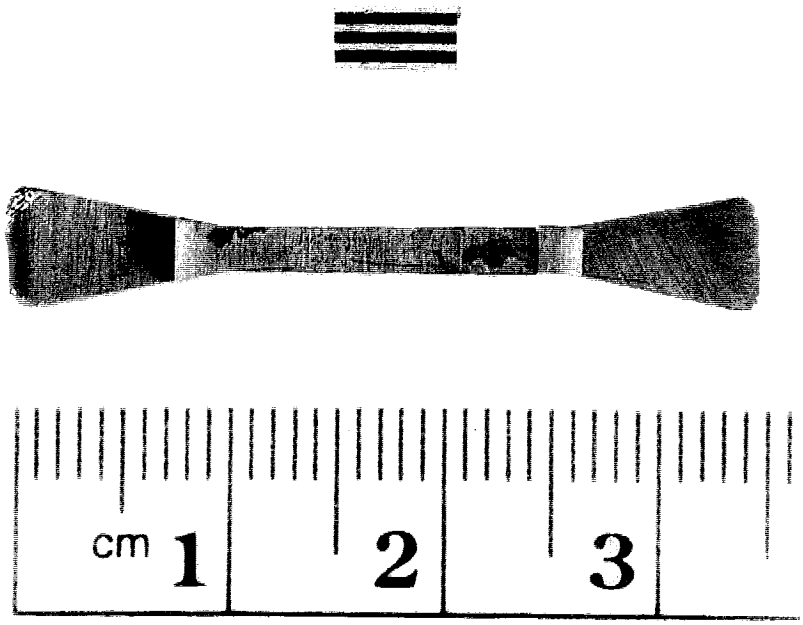

Fig. 3.2. Photograph of as prepared bulk metallic glass matrix composite. Compression and tension samples.

both compression and tensile samples. The fracture surfaces of the tested samples were examined using a scanning electron microscopy (SEM).

3.3 RESULTS OF MECHANICAL TESTS OF UNREINFORCED $Zr_{57}Nb_5Al_{10}Cu_{15.4}Ni_{12.6}$ METALLIC GLASSES

3.3.1 Compressive and Tensile Properties

Fig. 3.3 shows a cylindrical sample of aspect ratio approximately 2:1 which was deformed in uniaxial compression along the axis of the cylinder until failure. The sample failed along shear band oriented at 45 degrees to the compressive axis. The tensile specimen also failed on a plane, which was declined at an angle 45 degrees from the tensile axis as shown in Fig. 3.4. The fracture occurs along a shear band, not normal to the loading axis. Fig. 3.5 shows the compression and tension stress-strain curve of unreinforced $Zr_{57}Nb_5Al_{10}Cu_{15.4}Ni_{12.6}$ (Vit 106) alloys. Vit 106 had only ~0.5 % inelastic deformation in compression. There was no inelastic deformation in tension. However, fracture propagates in a ductile manner, since fracture propagates along a plane oriented at 45 degrees to the loading axis and shows vein patterns on the fracture surface. The elastic modulus of unreinforced Vit 106 alloy was measured using the slope of the stress-strain curve in Fig. 3.5. The elastic modulus was 85 GPa in compression and 83 GPa in tension. This is a good agreement with the value measured using the ultrasonic technique.[17] The compressive strength and tensile strength of Vit 106 alloy is 1.8 GPa and 1.2 GPa, respectively. The 1.2 GPa tensile strength of Vit 106 alloy is 2/3 of the compressive strength. However, this value of tensile strength of Vit 106 is not reliable because the big void was found on the fracture surface of

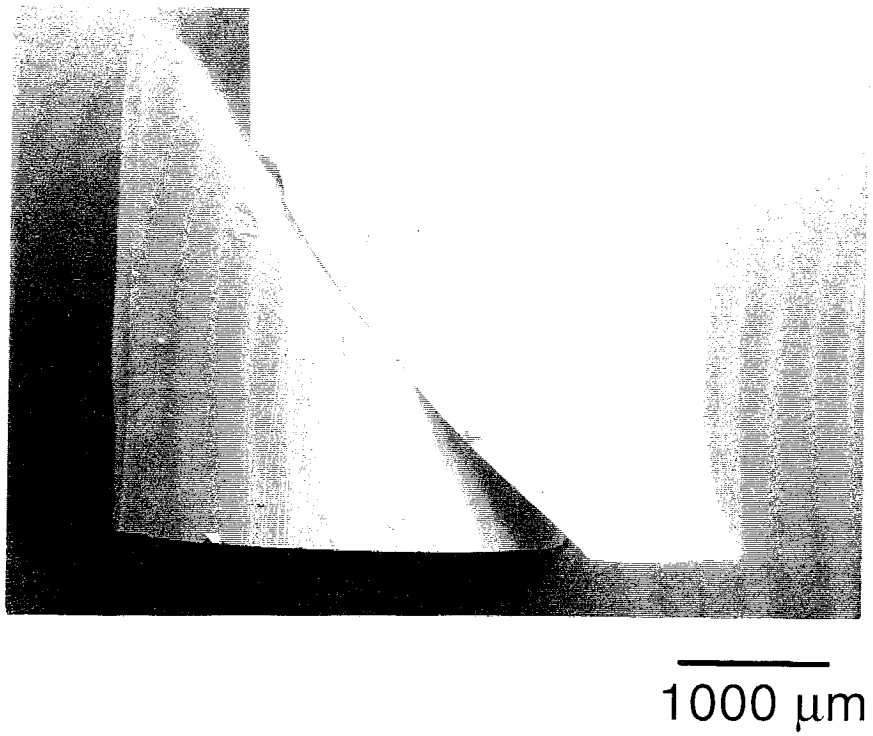

Fig. 3.3. Vit 106 compression test specimen. The specimen failed along 45 degree to compressive axis.

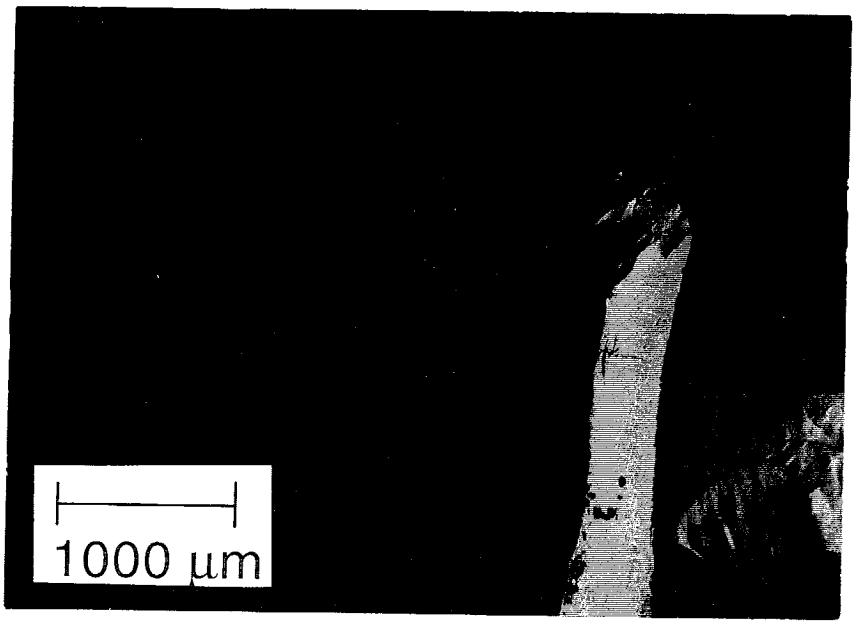

Fig. 3.4. Vit 106 tension test specimen. The specimen failed on the plane, which is declined at 45 degrees from the tensile axis.

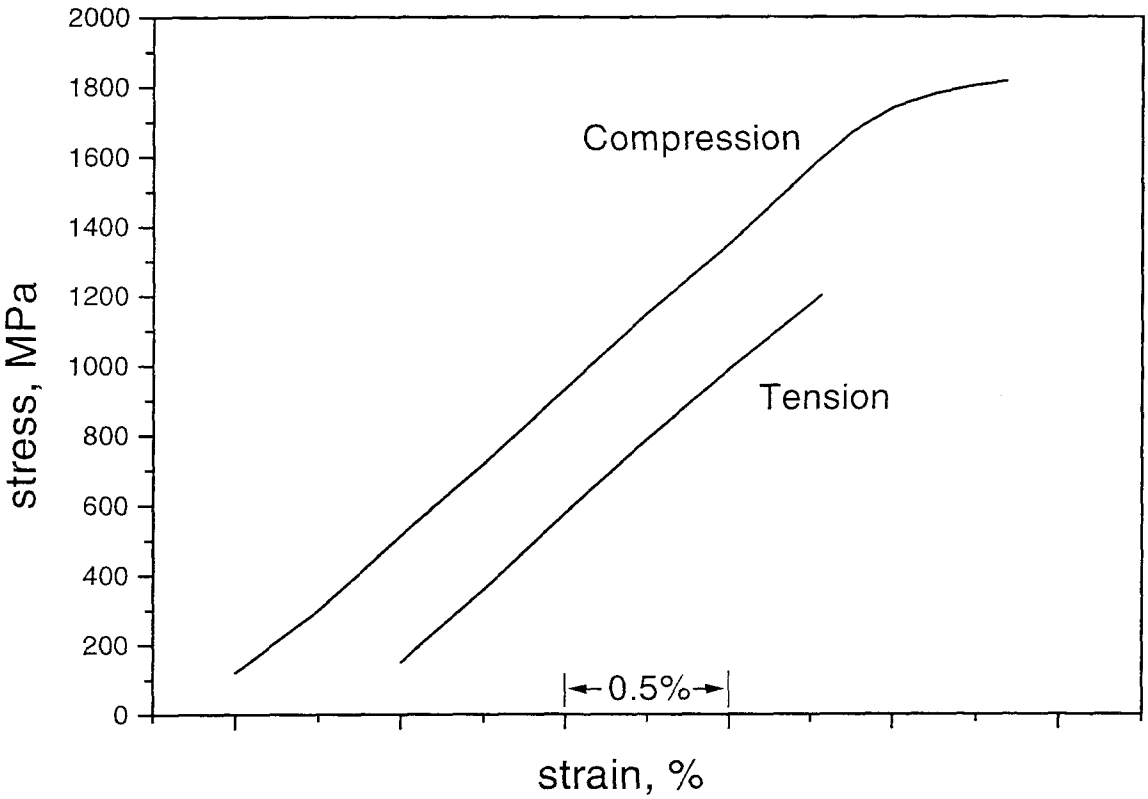

Fig. 3.5 Compression and tension stress-strain curve for Vit 106.

specimen after the tensile test. So the value of the elastic modulus of Vit 106 will be more emphasized and compared with the value of elastic modulus of Vit 106 composite.

3.3.2 Compressive and Tensile Fracture Surface Morphology

The fracture surfaces of the unreinforced Vit 106 after compression test were obtained using scanning electron microscopy shown in Fig. 3.6 and Fig. 3.7. Fig. 3.6 shows typical vein pattern on a flat, very smooth and featureless surface at 45 degrees to the compression axis. These features are identical to those obtained on the failure surfaces of other metallic glasses tested in compression.[18] The tributary veins or 'fingers' are shown in Fig. 3.7. The formation of tributary veins or fingers is due to an instability of the interface between two fluids that have different viscosity. This hypothesis was confirmed by shear experiments performed on a viscous material that has been placed between glass slides.[9] After the slides are sheared apart, tributary veins are formed on the separated surfaces. Fig. 3.8 shows two matching segments of tensile specimen of a Vit 106 alloy. This specimen fractured on two macroscopic surfaces, each oriented 45 degree from the tensile axis. Fig. 3.9 shows the two matching fracture surfaces of tensile specimen. These fracture surfaces show a more detailed view of the right side of the two opposing segments as shown in Fig. 3.8. When one observes the two matching fracture surfaces of Fig. 3.9, one generally finds that the location of the matching features with respect to the sides of the specimen are displaced one with respect to the other. This is shown schematically in Fig. 3.10. This suggests that shear, between the two sides, has

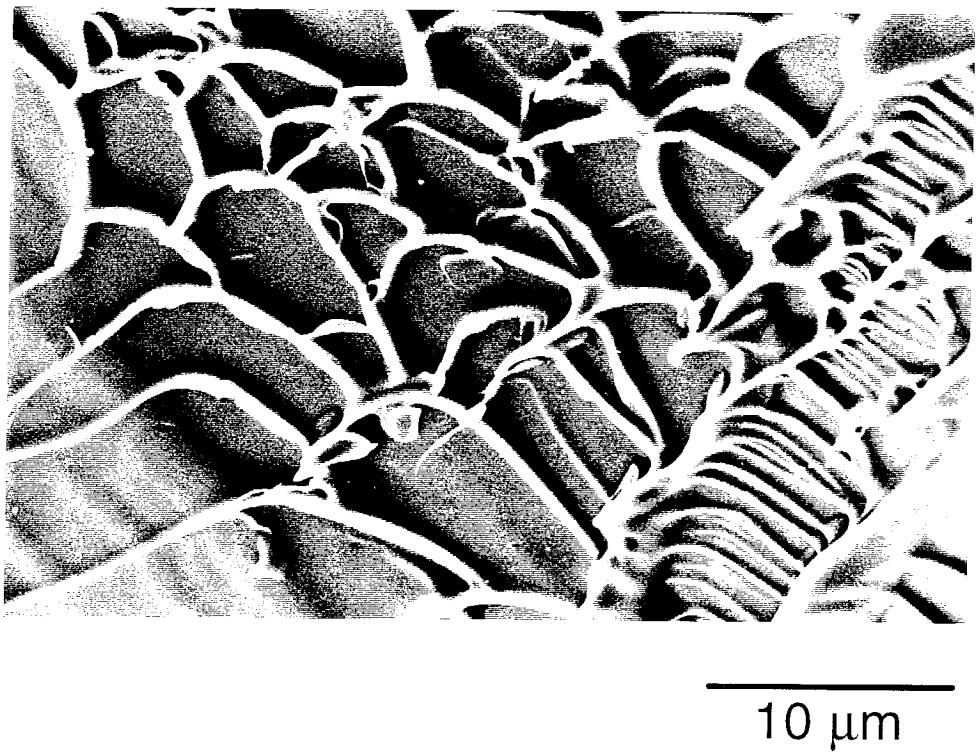

Fig. 3.6. Vein pattern of Vit 106 compression specimen.

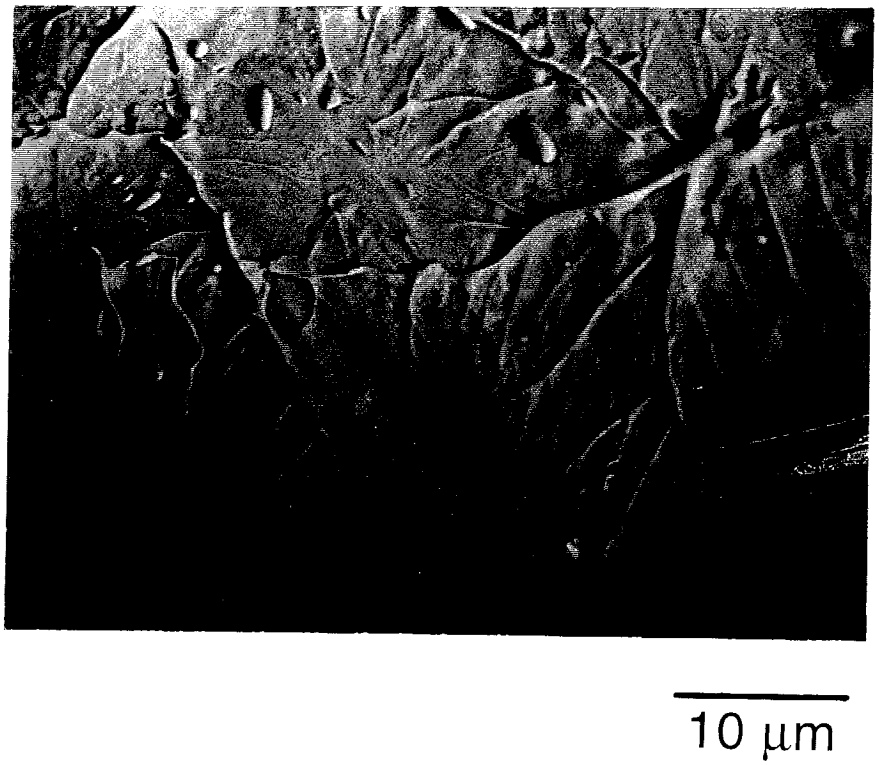

Fig. 3.7. The tributary veins or fingers of Vit 106 compression specimen.

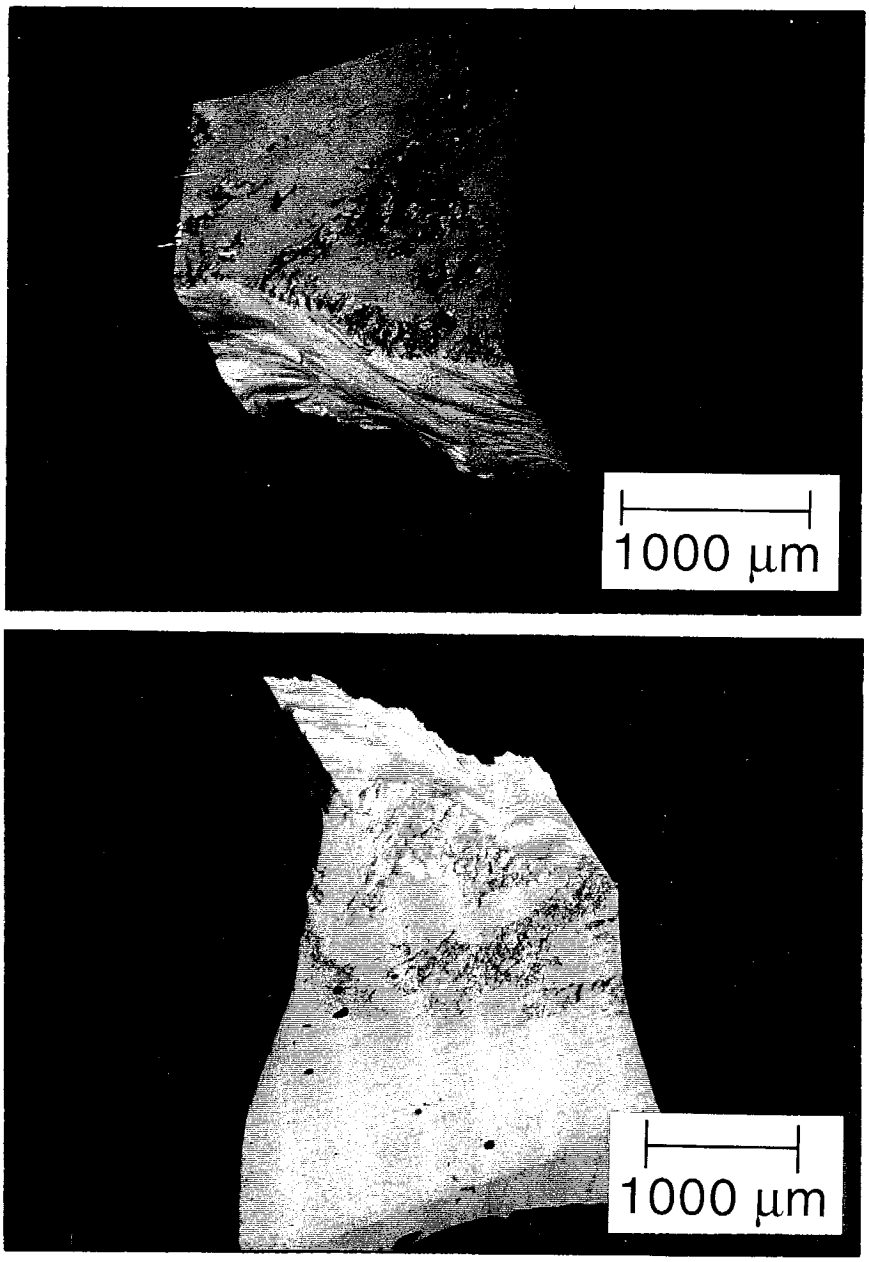

Fig. 3.8. SEM micrograph of the tensile fracture surface of opposing segments of pure Vit 106. Specimen fractured on two macroscopic surfaces, each oriented 45 degree from the tensile axis, the same as for uniaxial compression.

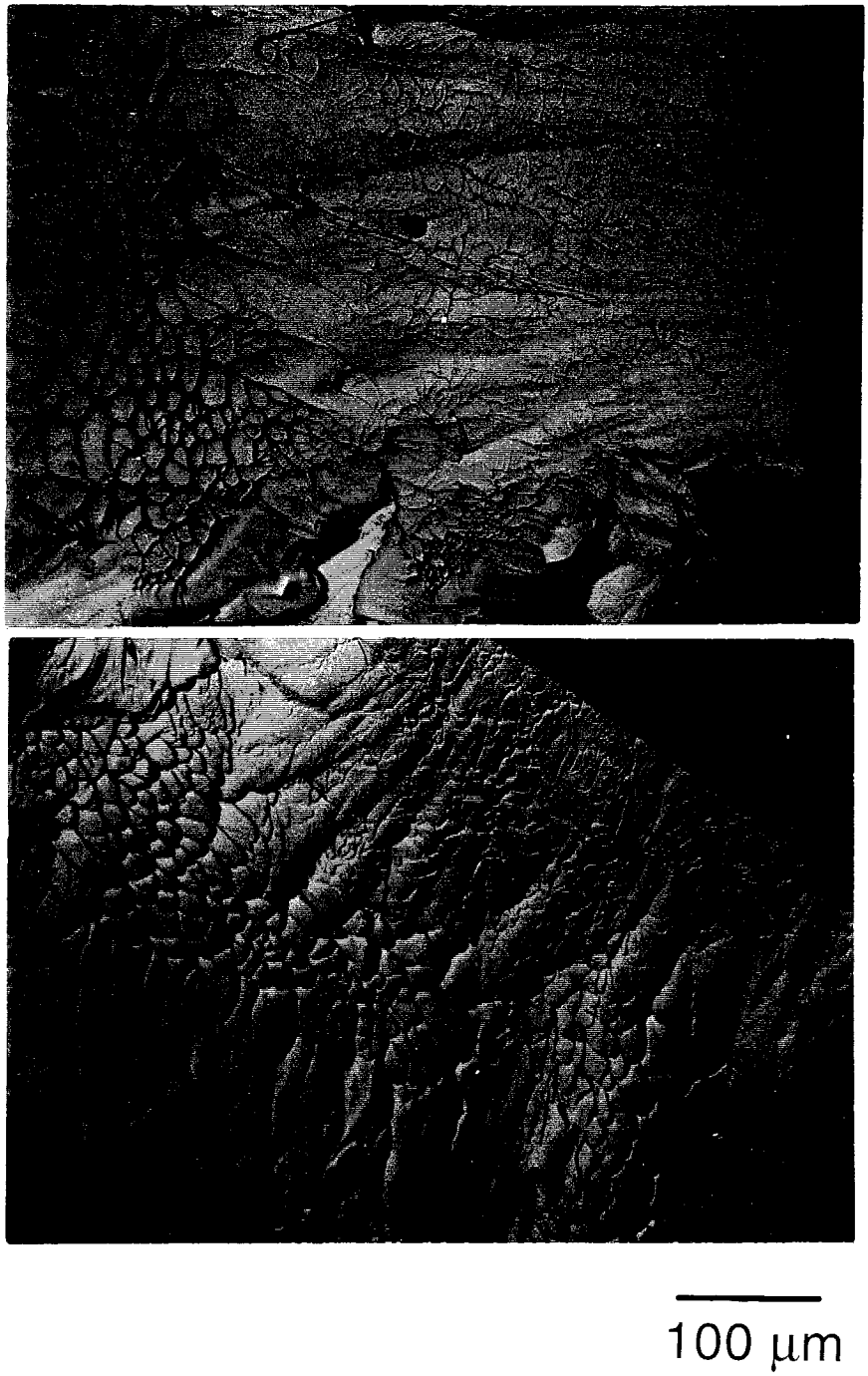

Fig. 3.9. The tensile fracture morphology of a Vit 106. The surfaces of opposing segments of the fractured specimens are shown in the upper and lower parts of micrographs.

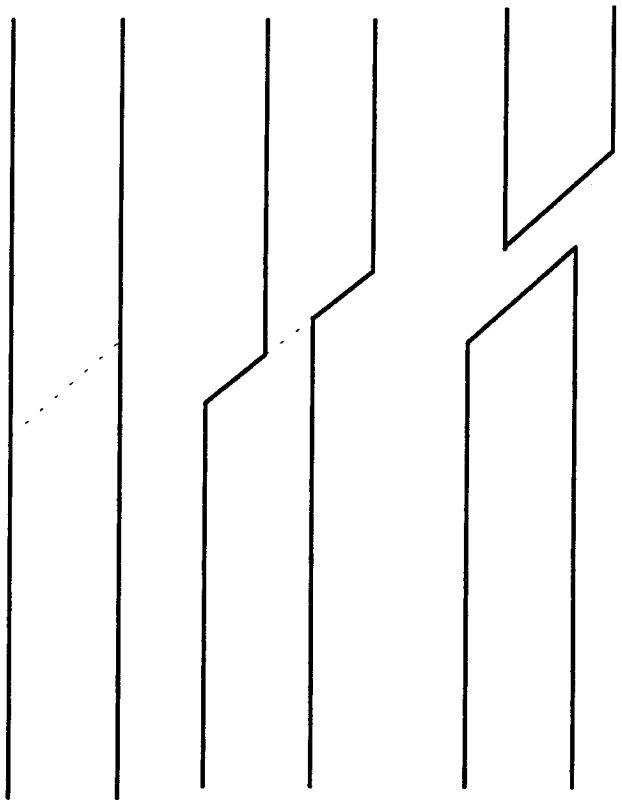

Fig. 3.10 Schematically showing the shearing before failure and failure along the sheared surface.

occurred before failure. The fracture morphology consists of two distinguished zones. One zone is featureless and appears smooth. This featureless area is corresponding to the slip step formed just before failure. The other zone shows vein patterns, which are associated with extensive plastic flow. It is apparent that this alloy does not fracture in a typical glassy or brittle manner; i.e., the two complementary fracture surfaces are not mirror images on a microscopic scale and the fracture surfaces are not normal to the tensile axis.

3.4 RESULTS OF MECHANICAL TESTS OF $Zr_{57}Nb_5Al_{10}Cu_{15.4}Ni_{12.6}$ METALLIC GLASSES COMPOSITES

3.4.1 Compressive and Tensile Properties

Compression tests were performed on particulate composites containing WC, SiC, W, and Ta. In all composite specimens, the compressive fracture takes place along the maximum shear plane, which is declined by about 45 degrees to the direction of compressive load. Pure Vit 106 exhibits only 0.5% inelastic deformation in compression. Samples reinforced with SiC shows similar behavior like pure Vit 106. However, plastic elongation of samples reinforced with WC, W and Ta exhibited 3 to 7% under compression as shown in Fig. 3.11. This increase is the result of residual tensile stress in the matrix and the formation of multiple shear bands. Residual stress develops within the composite upon cooling due to the thermal strain which results from the unequal thermal expansion of the particle and the matrix. The thermal expansion coefficient, α, of metallic glasses is larger than the thermal expansion coefficients of all of the reinforcing particles. So the difference in the thermal expansion coefficients,

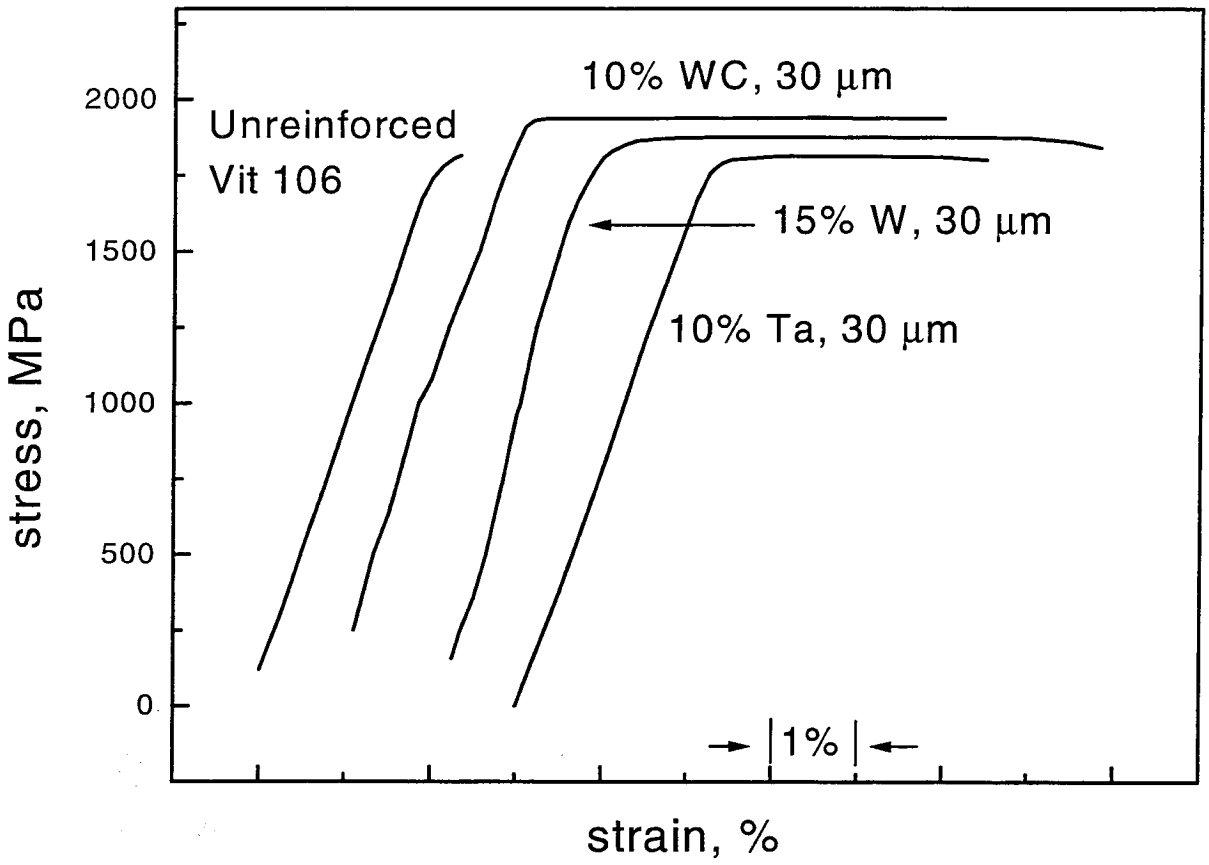

Fig. 3.11. Quasi-static compression stress-strain curves of Vit 106 and composites reinforced with WC, W, and Ta. The composites exhibited substantial plasticity (3-7 %) under compression.

$\Delta\alpha=\alpha_p-\alpha_m$, is negative in all the composites tested. The temperature change upon cooling is ΔT= -400 K, which is the difference between room temperature, T=293K and the measured glass transition temperature, T_g=693K. The thermal strain, $\varepsilon_T= \Delta\alpha\Delta T$, is positive, which gives the effect of placing the particle in compression and the matrix in tension. As a result of the residual tensile matrix stresses, cracks are directed toward the particles. The particles then act to retard crack propagation. The strength of the metallic glass composites was increased little compared to that of the unreinforced metallic glasses. The compressive strength of composites increased from 1.82 GPa at 0 vol% reinforcement to 1.96 GPa at 15 vol% W reinforced composites.

Fig. 3.12 shows the stress-strain curves of Vit 106 and the composites containing WC, SiC, and W obtained by tensile tests. None of the specimens shows extensive plastic deformation as observed in the compression specimens. The stress-strain curves for the W composite samples show a noticeable nonlinearity compared to the linear behavior of unreinforced Vit 106 alloy. The composite with SiC shows a smaller value of elastic modulus than pure Vit 106. In addition, composites with 5% W, but different particle sizes of 12 μm and 30 μm, respectively, are compared. They both show an increased elastic modulus compared to the pure Vit 106. The composite with 5% of 12 μm W has higher elastic modulus than the one of the composite with 5% of 30 μm W. Numerical integration of the tensile stress-strain curves gives a specific energy for failure of Vit 106 of 870 MJ/m^3. The specific energy of composite reinforced with 5% of 30μm W was 1330 MJ/m^3.[17]

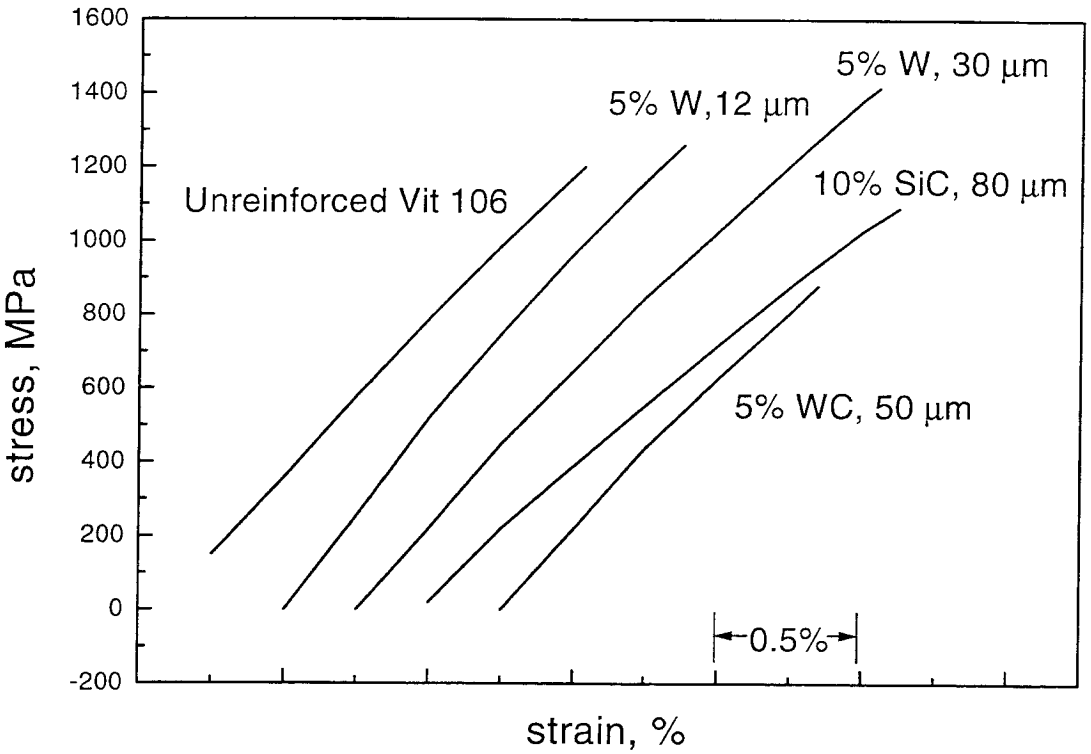

Fig. 3.12. Quasi-static tensile stress-strain curves for Vit 106 and composites reinforced with WC, SiC, and W. The energy to break the material increased by over 50% in W reinforced Vit 106.

So the energy to break, which reflects an increase in toughness, increased by over 50% in W reinforced Vit 106. The ceramic particle reinforcements did not provide significant increase in toughness.

3.4.2 Compressive and Tensile Fracture Surface Morphology

As shown in Fig. 3.11, compressive ductility of the glass in the composite was enhanced by adding particles into the glass. Figure 3.13 depicts a micrograph of the side of a composite reinforced with 10% WC. This picture reveals that multiple shear bands form in the glass. This suggests that the deformation mechanism in the composite must have changed compared to the pure glass. Evidently the constraint which the reinforcement provides on the matrix prevents catastrophic failure of the material and leads to the formation of secondary bands parallel to the initial band.

Multiple shear bands can be uniformly distributed in the entire volume of the glass or occur in region close to the primary shear band, as it is observed in Fig. 3.13. Uniform shear band distributions are expected when the initial slip displacement is small (for example, when volume fraction of reinforcement is high).[19] Localized multiple shear banding is expected when initial slip displacements are large.[20] Fig. 3.13 shows localized multiple shear banding near the primary shear band. The formation of multiple shear bands is initiated by particles, which are blocking the propagation of the single shear band. Based on these results, we can conclude that the extended plasticity of the composites was obtained after promoting the formation of multiple shear bands.

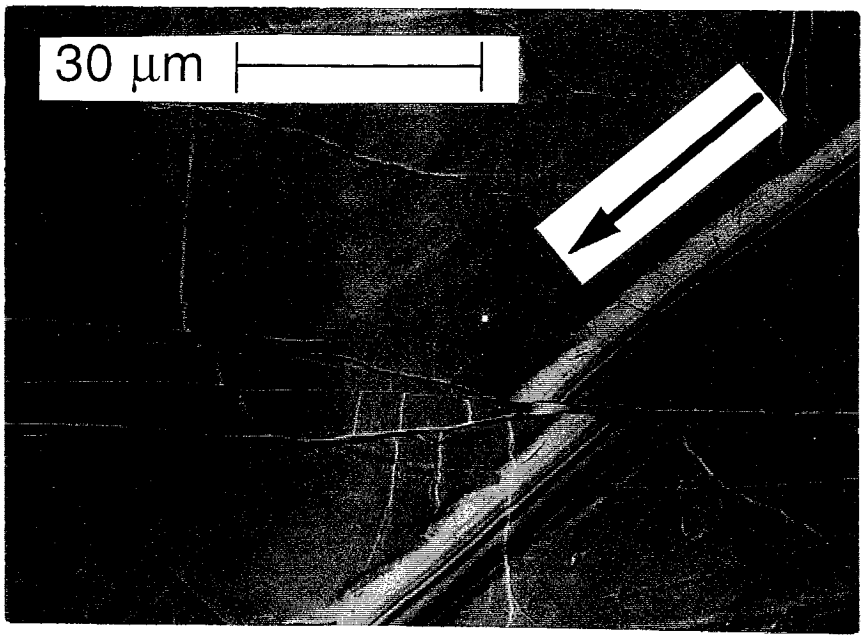

Fig. 3.13. SEM micrograph of the side of a 10% WC reinforced composite for Vit 106. Multiple shear bands are clearly visible and localized near the primary shear band. The arrow indicates the direction of compressive load.

Figure 3.14 shows the fracture surface of a composite around a particle. The fracture occurred under compression in a specimen reinforced with 5% W. This picture exhibits the characteristic vein pattern of the resulting fracture surface morphology. As discussed previously, this vein-like morphology on the failure surface is probably attributed to localized melting during shear banding failure. The direction of the veins is related to the direction of the fracture process. The slippage occurred in the direction of the arrow. The picture clearly proves that particles are restricting shear band propagation. The reduced size of the vein pattern in front of the particle indicates that the flow of material had slowed down in front of the particle. That means the propagation of shear band was blocked by the reinforcing particles. We also observe the flow of metallic glass over the particle. This indicates that the viscosity of the glass in the shear band is low compared to the surrounding glass. It has been shown that during the deformation of metallic glasses a fluid layer is formed in the shear plane.[9]

Fig. 3.8 and 3.15 show the tensile specimens fracture surfaces of pure Vit 106 and Vit 106 reinforced with 5% of 30 μm W particles, respectively. Fig. 3.8 shows the typical tensile failure mode of pure metallic glass, which fails along 45 degrees to the axial loading direction. The highly localized deformation associated with a shear band leads to failure following propagation of the first shear band during tensile loading, which limit tensile ductility for metallic glasses. In Fig. 3.15, rims are observed on both edges of the sample, which are never present on pure Vit 106 sample. This change of tensile failure mode in Vit 106 reinforced with W particles must be caused by particles. Fig. 3.16 is a higher magnification micrograph showing the area closed to rim. The step is more

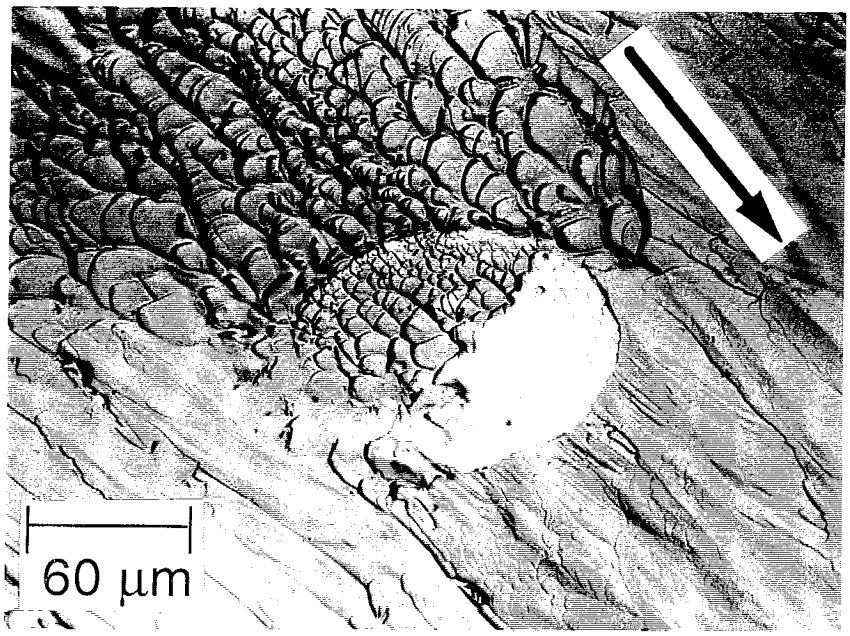

Fig. 3.14. SEM micrograph of the compressive fracture surface of a 5% W reinforced composite for Vit 106. The arrow indicates direction of shear band propagation. The propagation of shear band was slowed down by the reinforcing particles.

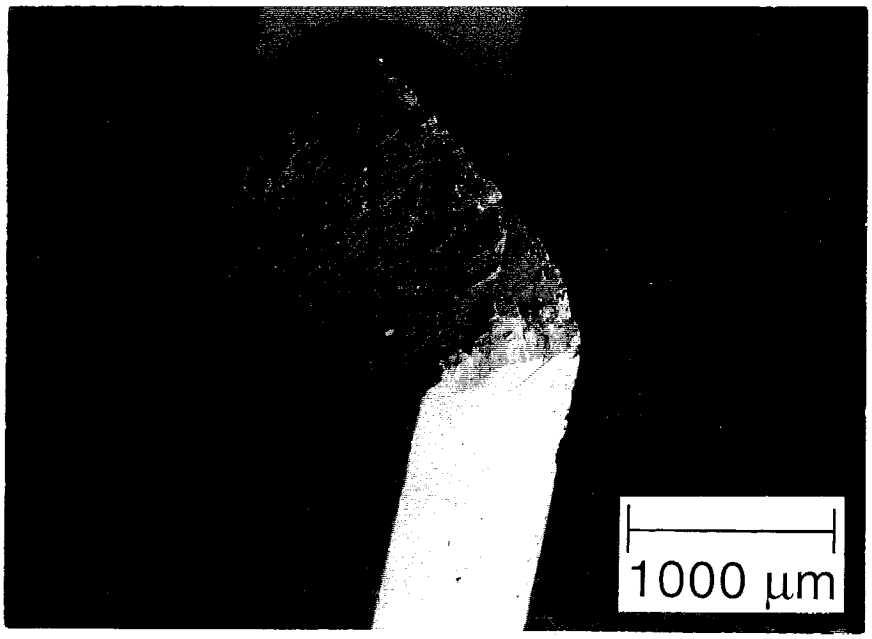

Fig. 3.15 SEM micrograph of Vit 106 reinforced with 5% of 30 µm W particles tensile fracture surface. Rims, which have ductile fracture surfaces, are on both edges of the sample.

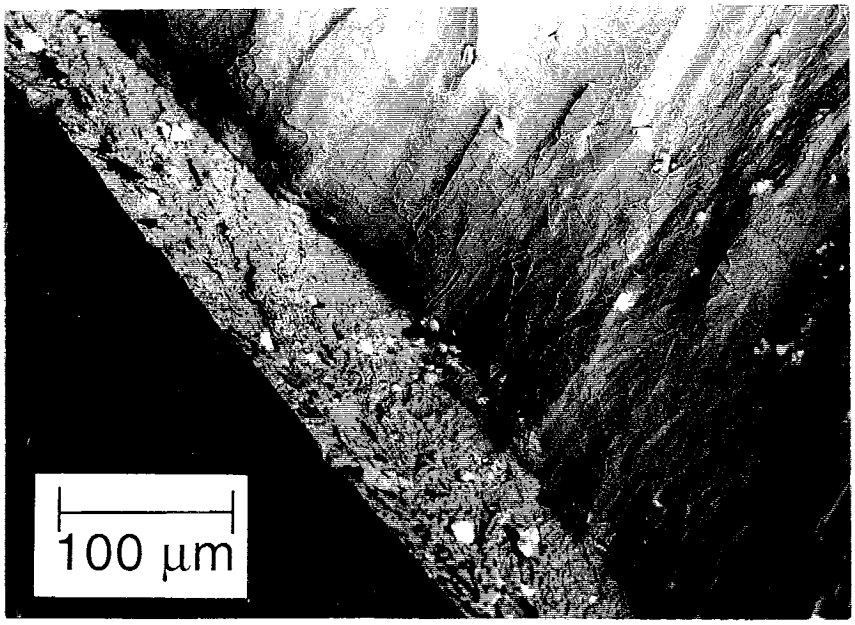

Fig. 3.16. A higher magnification micorgraph showing the area closed to the rim. The step is more clearly visible.

clearly visible. These rims become wider when Vit 106 is reinforced with smaller size of W particle. Fig. 3.17 is the fracture surface of a Vit 106 reinforced with 5% of 12 μm W particles. The wider rims imply the bigger fracture toughness, since the region of rims reveals ductile fracture surface. Fig. 3.18 represents a closer look at a rim. The upper left side of the picture shows typical vein patterns of the metallic glass fracture surface and the lower right side of the picture shows the area of rim on one edge of the sample. This rim region exhibits a fracture surface as it is observed in ductile materials. This rough, dimpled surface is characteristic of most ductile fracture surfaces in polycrystals. This suggests that adding particles into the metallic glass increases the fracture toughness.

As mentioned previously, the elastic modulus of composite with 5% of 12 μm W is higher than the one of composite with 5% of 30 μm W. Fig. 3.19 shows the 30 μm W particle in the matrix. A gap between the particle and matrix is clearly visible. This means the load could not be transferred efficiently. Contrarily, Fig. 3.20 shows the 12 μm W particle in the matrix. There is no gap between the particle and the matrix. This means the load was transferred efficiently. This explains the higher modulus of composite with 5% of 12 μm W compared to that of composite with 5% of 30 μm W.

3.5 CONCLUSIONS

The range of plastic deformation of the material was improved drastically under compression in the case of WC, W, and Ta particles. This is attributed to the formation of multiple shear bands in the presence of particles. The SiC, in

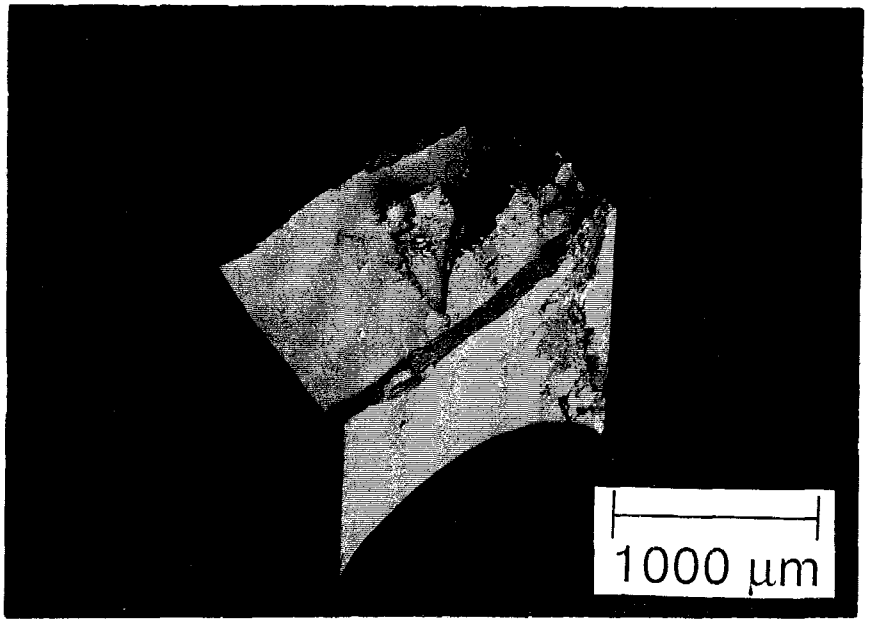

Fig. 3.17. Tensile fracture surface of Vit 106 reinforced with 5% of 12 μm W particles. Rims are wider compared to that of Vit 106 with 5% of 30 μm W particles.

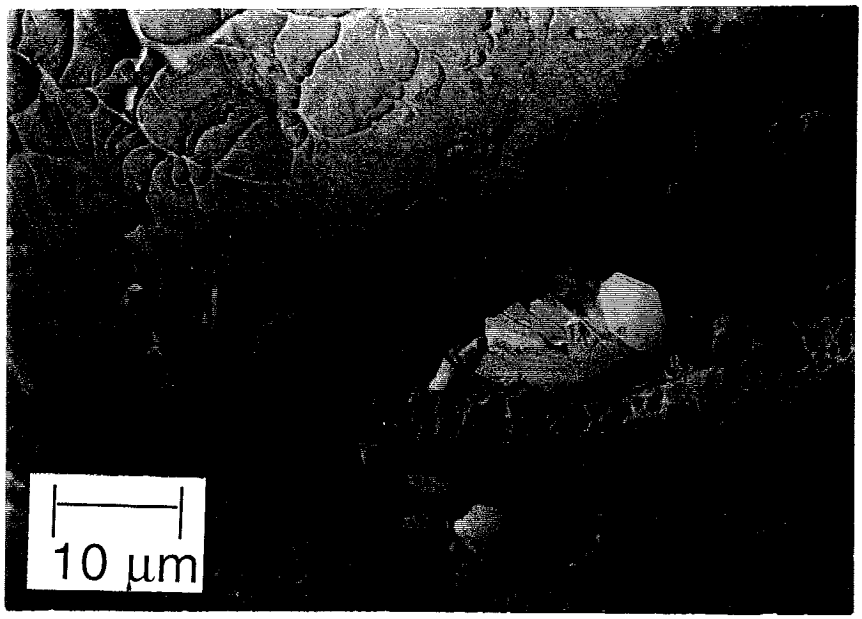

Fig. 3.18. Close up of area around rim of Fig. 3.17. The upper left side shows vein pattern of the metallic glass fracture surface and the lower right side shows a dimpled fracture surface which is characteristic of most ductile fracture surface in polycrystals. Fractured W particle are observed in the rim.

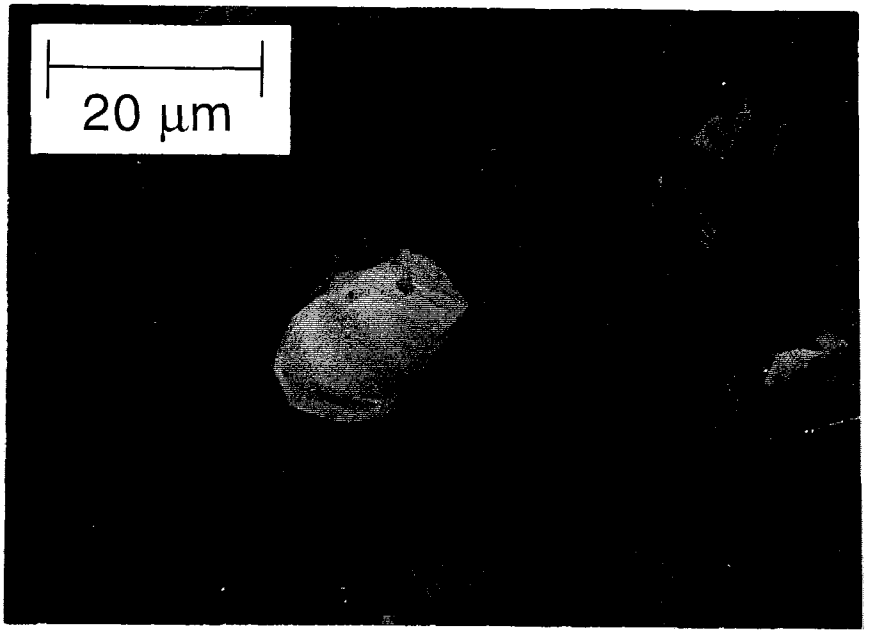

Fig. 3.19. The 30 μm W particle in the Vit 106 matrix. The gap between the particle and matrix is clearly visible.

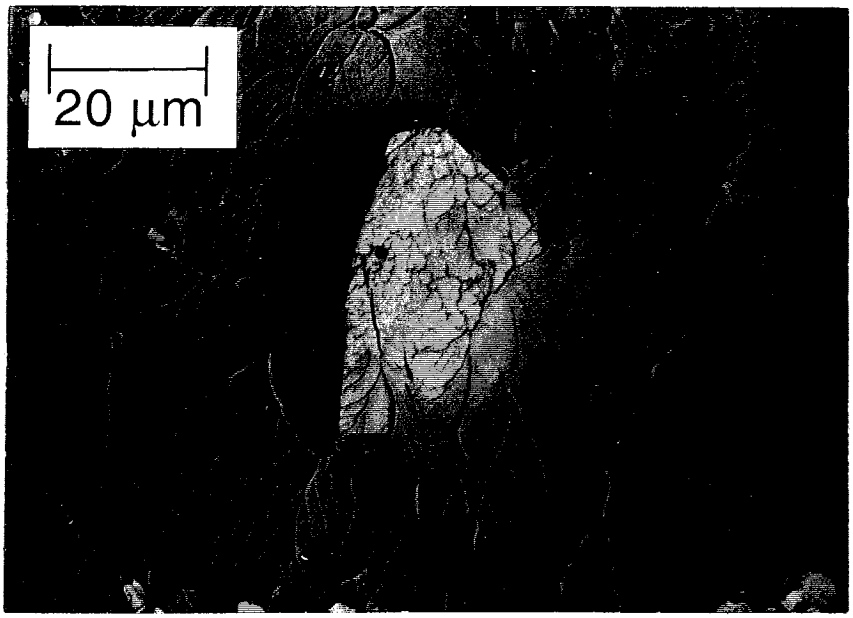

Fig. 3.20. The 12 µm W particle in the Vit 106 matrix. In constrast to the 30 µm W particle in the Vit 106 matrix, there is no gap between the particle and the matrix.

contrast, did not improve the ductility, which is related to the fact that the interface between the SiC particles and their shell of ZrC turned out to be very weak. In tension no significant improvement of plasticity was observed. However, the energy to break the material increased substantially. The investigation of the fracture surfaces after failure under tension reveal an increasing tendency to ductile failure with increasing volume fraction and decreasing size of the particulates.

REFERENCES

1. T.H. Courtney, *Mechanical Behavior of Materials*, McGraw Hill, New York (1990).
2. F. Spaepen, *Acta Met.* **25**, 407 (1977).
3. D.E. Polk and D. Turnbull, *Acta Met.* **20**, 493 (1972).
4. C.A. Pampillo, *Scripta Met.* **6**, 915 (1972).
5. F. Spaepen and D. Turnbull, *Scripta Met.* **8**, 563 (1974).
6. M.H. Cohen and D. Turnbull, *J. Chem. Phys.* **52**, 3038 (1970).
7. H.J. Leamy, H.S. Chen and T.T. Wang, *Met. Trans.* **3**, 699 (1972).
8. H.A. Bruck, A.J. Rosakis and W.L. Johnson, *J. Mater. Res.* **11**, 503 (1996).
9. C.A. Pampillo and A.C. Reimschuessel, *Journal of Materials Science*. **9**, 718 (1974).
10. P.G. Saffman and G. Taylor, *Proc. Roy. Soc. London* A **245**, 312 (1958).
11. H.A. Bruck, T. Christman, A.J. Rosakis and W.L. Johnson, *Scripta Met.* **30,** 429 (1994).
12. C.G. Gilbert, R.O. Ritchie and W.L. Johnson, *Appl. Phys. Lett.* **71**, 476 (1997).
13. D. Conner, A.J. Rosakis and W.L. Johnson, *Scripta Met.* **37**, 1373 (1997).
14. C.A. Pampillo and H.S. Chen, *Mat. Sci. Eng.* **13**, 181 (1974).
15. H.S. Chen, H.J. Leamy and M.J. O'Brien, *Scripta Met.* **7**, 415 (1973).

16. S. Takayama and R. Maddin, *Acta Met.* **23**, 943 (1975).

17. R.D. Conner, H. Choi-Yim and W.L. Johnson, *Journal of Material Science* (in press); R.D. Conner, Ph.D. thesis, California Institute of Technology (1998).

18. H.A. Bruck, Ph.D. thesis, California Institute of Technology (1995).

19. A.T. Alpas and J.D. Embury, *Scripta Metall.* **22**, 265 (1988).

20. Y. Leng and T.H. Courtney, *Journal of Materials Science*. **24**, 2006 (1989).

CHAPTER 4
THE EFFECT OF SILICON ON THE GLASS FORMING ABILITY OF THE $Cu_{47}Ti_{34}Zr_{11}Ni_8$ BULK METALLIC GLASS FORMING ALLOY DURING PROCESSING OF THE COMPOSITES

4.1 INTRODUCTION

Bulk metallic glass formers are excellent matrix materials for composites because of their low melting and glass transition temperatures. The low glass transition temperature helps to reduce differential thermal stresses, which develop between the reinforcement and matrix during freezing upon cooling. The low melting temperatures of metallic glass formers result in slow chemical interactions between the reinforcing particles and the liquid during processing. However, the dissolution or reaction of a certain amount of the reinforcement phase with the metallic glass matrix has still to be taken into account. These interfacial reactions and dissolution of reinforcement into the melt can be responsible for degradation of the glass forming ability of the matrix, e.g., by moving the composition of the liquid out of the optimum glass forming range.[1]

In this section, we observe the opposite case. One can improve the glass forming ability of the matrix by interdiffusion between the reinforcement and the metallic glass matrix. It will be shown that the addition of Si to Cu-Ti-Zr-Ni alloy enlarges the supercooled liquid region and the glass forming ability.

4.2 EXPERIMENTAL PROCEDURE

The $Cu_{47}Ti_{34}Zr_{11}Ni_8$ alloy (Vit 101) [2] was used as a matrix material for composites. Ingots of the alloy were prepared by arc melting a mixture of the elements having a purity of 99.7 at. % or better. Subsequently, a mixture of the pre-alloyed Vit 101 and SiC particles was induction melted on a water cooled copper boat under a 800 mbar Ti-gettered argon atmosphere. Volume fractions of SiC particles ranged from 10 to 30 percent and the average size of the particles was 50 micrometers. In order to obtain an amorphous matrix, the composites were then cast into Cu-molds. This resulted in rods with a diameter of 3 mm and a length of 30 mm. In addition, quintary $Cu_{47}Ti_{34-x}Zr_{11}Ni_8Si_x$ (x= 0.5, 1, 2) alloys (Vit 102) were synthesized. First, binary alloys were prepared by arc melting a mixture of Cu and Si to form a solid solution of Si in Cu. Then the binary Cu-Si solid solution and the other three elements were arc melted together under argon atmosphere. Ingots were remelted and cast into a copper mold resulting in glassy strips or rods of different sizes up to a dimension of 7 mm.

4.3 RESULTS

4.3.1 Optical Microscope and X-ray

The particle distribution in the composite specimens was investigated by optical microscopy. Figure 4.1 shows the optical micrographs of the uniformly distributed SiC particles in the metallic matrix. The volume fractions of SiC

(a)

(b)

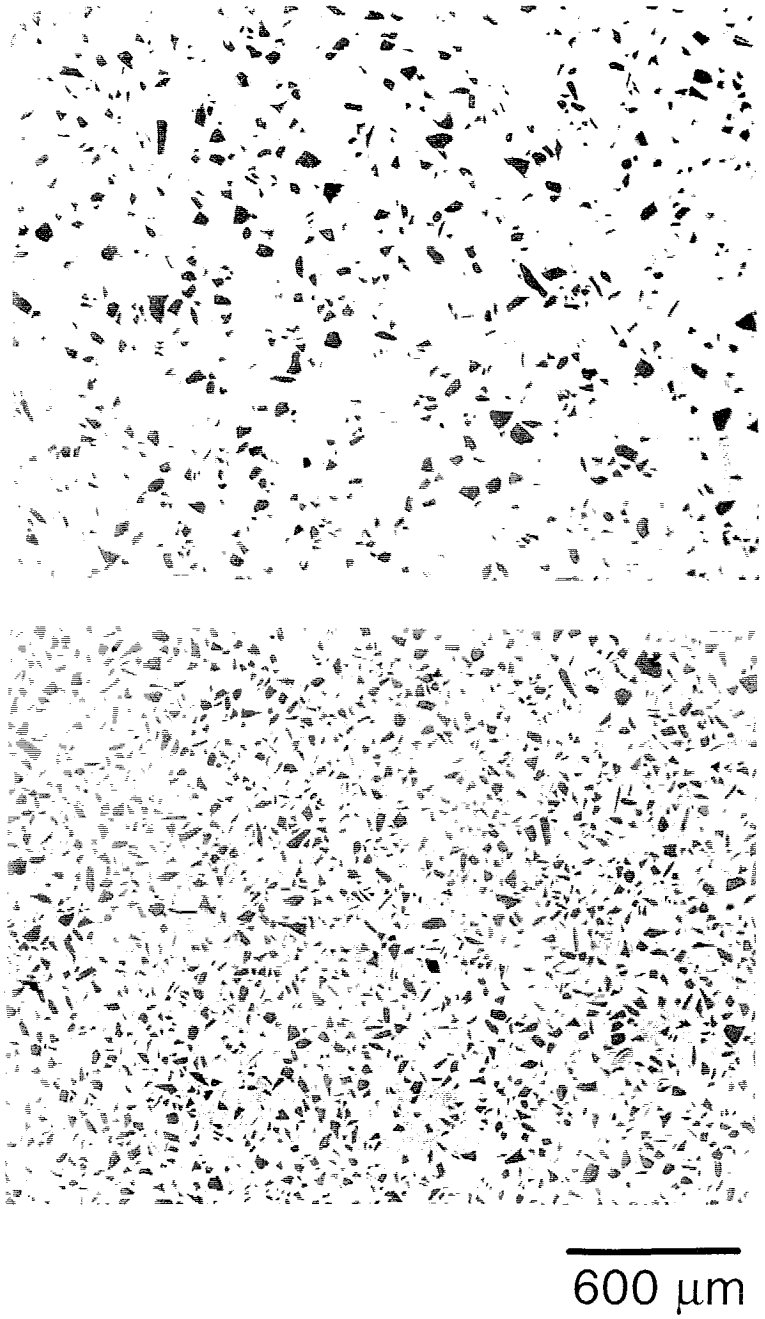

Fig. 4.1. Optical micrographs of $Cu_{47}Ti_{34}Zr_{11}Ni_8$ (Vit 101)/SiC composites, showing the uniform distribution of SiC particles in the Vit 101 matrix. In (a) the volume fraction of SiC particles is 10 % and in (b) it is 20 %. The average size of particles is about 50 micrometers.

particles were 10% and 20% in Fig. 4.1(a) and Fig. 4.1(b), respectively. The matrix appears uniform and free of heterogeneity.

Cross sections of cast strips and rods were examined by X-ray diffraction. In Fig. 4.2, the X-ray diffraction patterns of the amorphous matrix, the composite and the SiC particles are compared. The pattern of the specimen containing 30 volume percent SiC in a Vit 101 matrix shows diffraction peaks of SiC particles superimposed on the broad diffuse scattering maxima from the amorphous phase. The positions of the peaks in (b) and (c) exactly match. However, the intensity of the peaks are not the same due to the changing texture of the particles during processing. No other phases are detected within the sensitivity limits of X-ray diffraction. The volume fraction of a thin TiC interlayer between the SiC particles and the glassy matrix (see below) is too small to be detected by X-ray diffraction.

4.3.2 Differential Scanning Calorimetry

The glass transition and crystallization of all samples was studied with a Perkin-Elmer DSC 7. Different heating rates between 0.0167 and 3.33 K/s were used. Fig. 4.3 shows DSC scans of the pure amorphous Vit 101 and a series of SiC/Vit 101 composites with increasing SiC volume fraction from 10 vol. % to 30 vol. %. All measurements were performed with a heating rate of 0.33 K/s. They exhibit the endothermic heat effect due to the glass transition and the three characteristic steps of heat release, indicating the successive stepwise transformations from the metastable undercooled liquid state into the crystalline

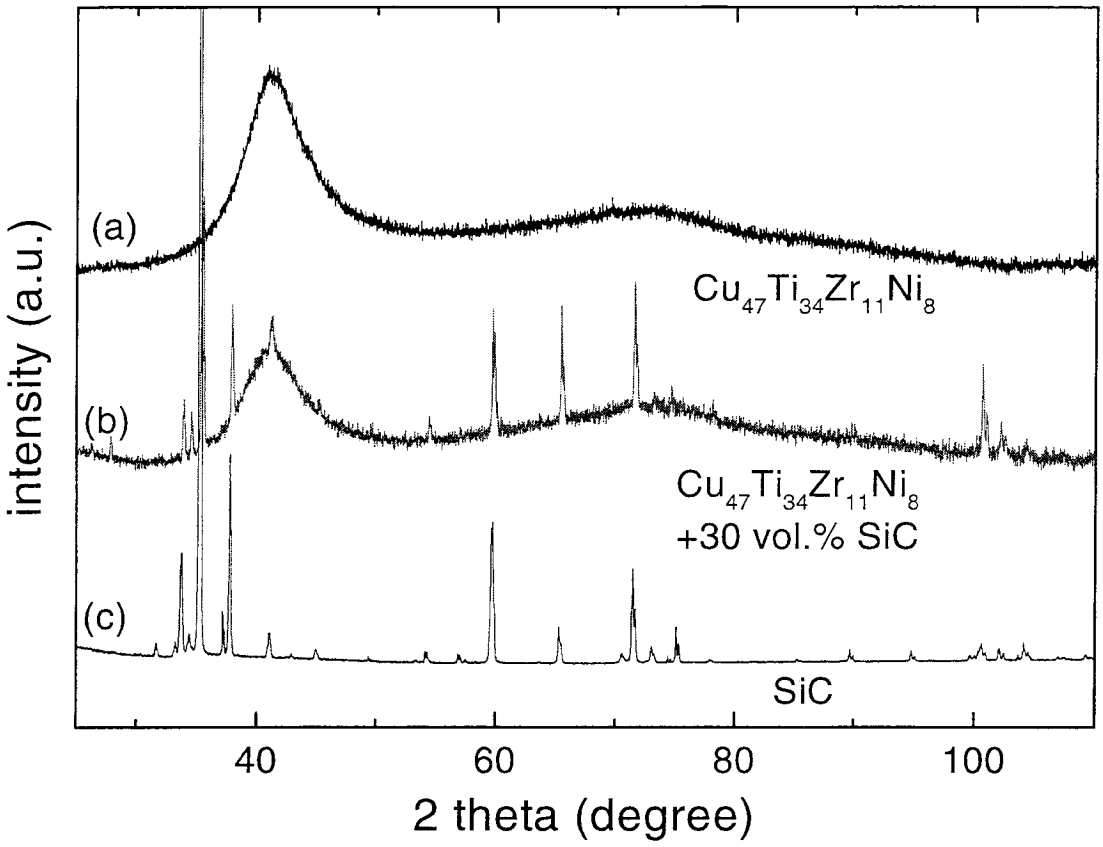

Fig. 4.2. X-ray diffraction patterns of (a) the amorphous $Cu_{47}Ti_{34}Zr_{11}Ni_8$, (b) a composite containing 30 vol. % SiC and (c) the pure SiC powder.

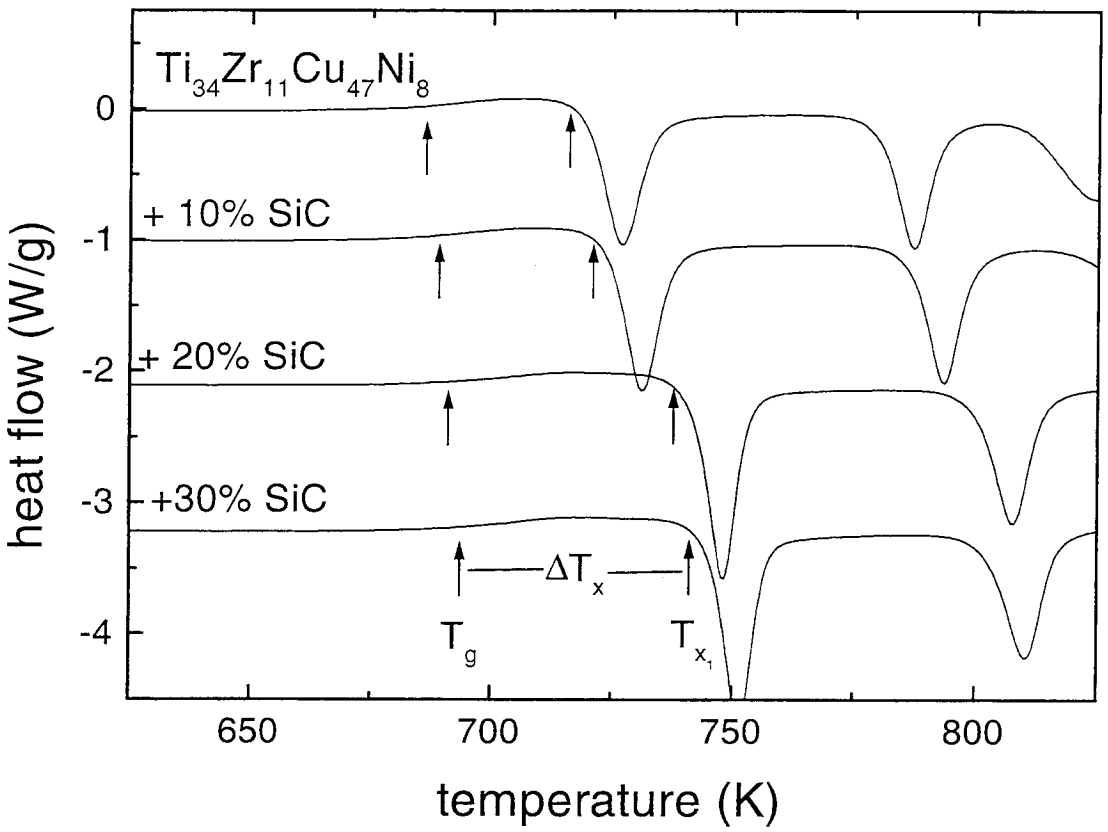

Fig. 4.3. DSC thermogram (heating rate of 0.33 K/s) of Vit 101 and SiC reinforced Vit101 with a volume fraction of 10, 20 and 30%, respectively. The width of the supercooled liquid region, ΔT_x, between onset of the glass transition, T_g, and the onset of primary crystallization, T_{x1}, increases with rising SiC particle content. The average particle size is 50 μm.

compounds. The glass transition temperature, T_g, is here defined as the onset of the endothermic DSC event. The primary crystallization temperature, T_{x1}, is defined as the onset temperature of the first exothermic event. Based on the DSC scans, it is observed that the addition of SiC particles into the Vit 101 produces a significant extension of the supercooled liquid region (ΔT_x) defined by the difference between T_g and T_{x1}. With increasing SiC particle addition into Vit 101, the glass transition temperature increases slightly. The onset temperature of primary crystallization (T_{x1}) rises even more resulting in an increase of ΔT_x from 46 K in the pure Vit 101 to 66 K for the Vit 101 that was reinforced with 30 vol. % SiC. This means that, surprisingly, the thermal stability of the bulk metallic glass matrix was enhanced during composite processing.

4.3.3 Scanning Auger Microscopy

In selected samples, in order to investigate the reaction that must have taken place during reactive wetting of the SiC particles by the matrix, the composites were investigated by scanning auger microscopy. The scanning Auger microscope (SAM) works in a similar way as the SEM. Both can be used on bulk samples. However, the SAM has a detector for Auger electrons which are emitted during relaxation of ionized atoms in the sample. This is a different mode of relaxation compared to emission of x-rays, which are detected by energy dispersive x-ray spectroscopy (EDS or EDXS). However, the preferred relaxation mechanism depends upon atomic number, and thus different elements are detected more easily by one technique than the other. In particular, the Auger

technique is much more sensitive to light elements. However, since Auger electrons can escape only from within a few angstroms of the sample surface without loss of the energy, the depth into the material that is analyzed by Auger spectroscopy is much smaller than that by EDXS.

Figure 4.4 shows the results of an auger line scan across the interface between matrix and particle. The auger signals for Si, C, and Ti are depicted. At the interface a TiC layer with a thickness of 500nm has grown. It forms a shell around the SiC particles. This means during processing Ti must have diffused from the matrix into the TiC layer, whereas Si must have diffused from the SiC particle throughout the TiC layer into the melt. In first approximation the Si content of the matrix equals the reduction of the Ti content in the melt. These observations suggest that a Si addition to Vit 101 is the reason for the enhanced thermal stability of the alloy.

To prove this, we prepared alloys in which we substituted 0.5, 1 and 2 at. % of the Ti in Vit 101 by Si. These concentrations can be estimated from the TiC layer thickness, the particle size and volume fraction. They are the approximate matrix Si-concentration in the composites containing 10, 20 and 30 vol. % SiC, respectively. The DSC scans of these $Cu_{47}Ti_{34-x}Zr_{11}Ni_8Si_x$ alloys (Vit 102) are shown in Fig. 4.5 in addition to the pure Vit 101. The Si addition substantially increases the supercooled liquid region. As can be seen in Fig. 4.6, the DSC scan for a sample with 1% Si is in good agreement with the DSC scan of a composite with 20 vol. % SiC. The matrix of the composite with a SiC content of 10 vol. % contains 0.5 at. % Si (not shown).

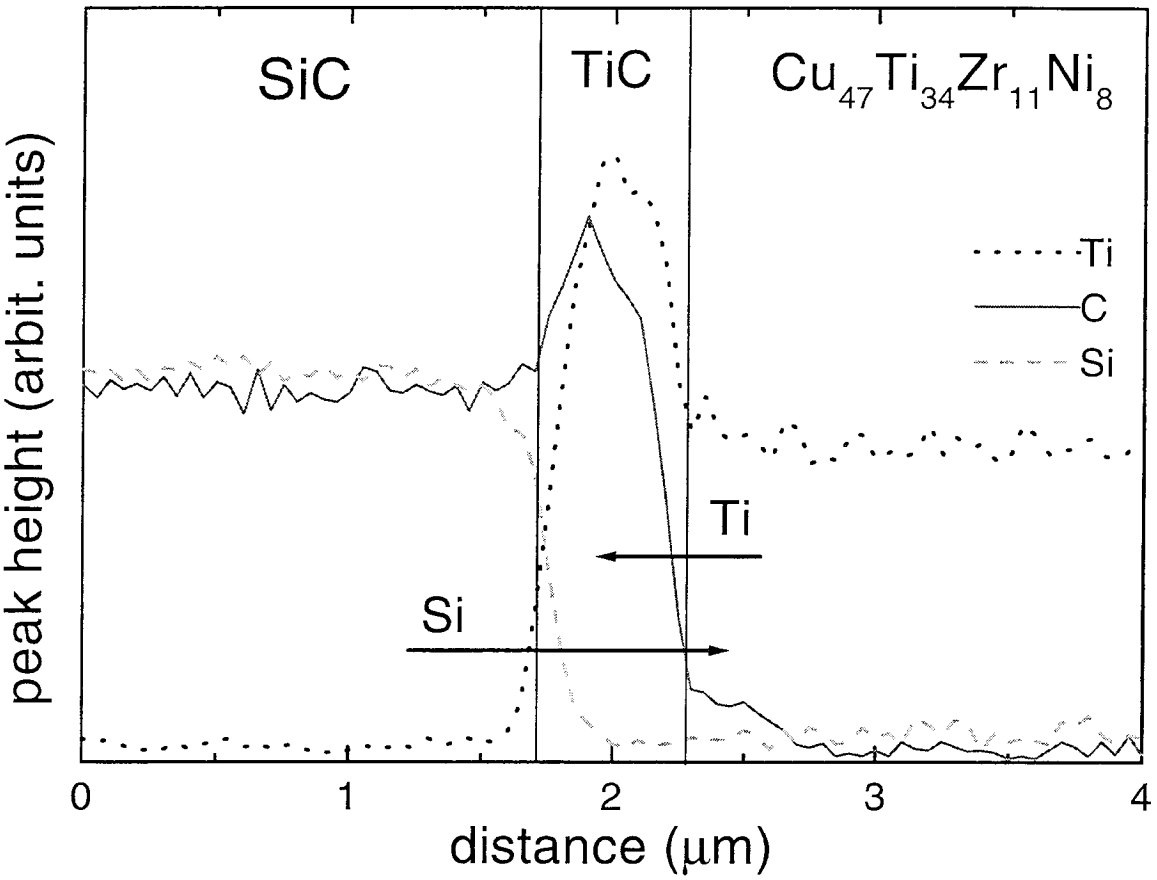

Fig. 4.4. Scanning auger microscopy line scans across the Vit 101 / SiC interface. A TiC layer with a thickness of about 500 nm formed at the interface during processing when the Vit 101 was in the liquid state.

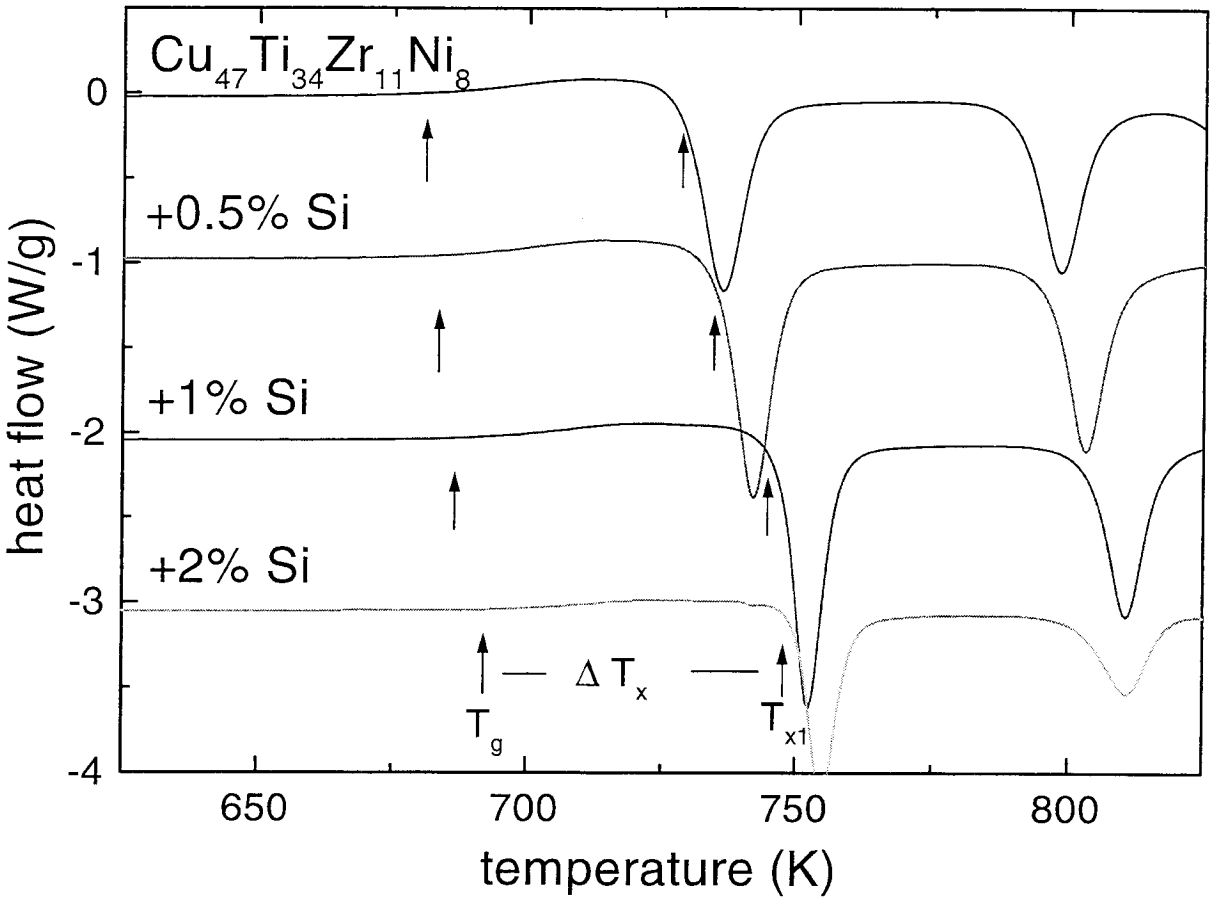

Fig. 4.5. DSC thermogram (heating rate of 0.33 K/s) of Vit 101 and of the Si bearing alloys (Vit 102).

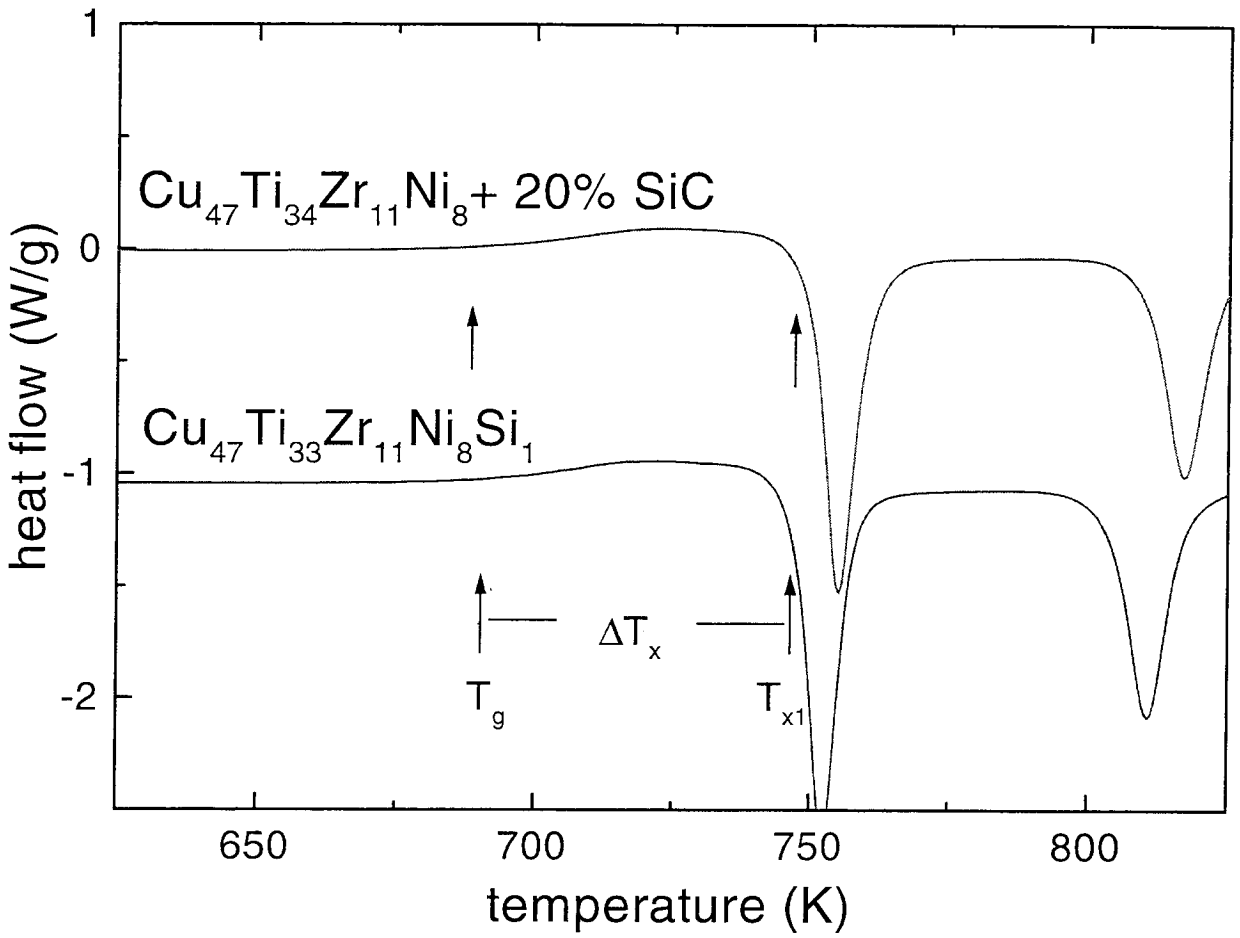

Fig. 4.6. DSC scans of the composite with a volume fraction of 20% particle in comparison with the $Cu_{47}Ti_{33}Zr_{11}Ni_8Si_1$ alloy (0.33 K/s).

The enlarged supercooled liquid region by Si addition suggests that the Vit 102 alloys have a better glass forming ability than the Vit 101 alloys, which we can mold cast up to a thickness of 4 mm. Fig. 4.7 compares the DSC scans of cast samples of Vit 101 with samples of Vit 102 containing 0.5 and 1 at. % Si, respectively. The Vit 101 alloy does not show a glass transition and crystallization peaks. It is completely crystalline. The Vit 102 alloys, in contrast, are completely amorphous as additional X-ray diffraction investigations confirm. The alloy that contains 1 at. % Si could be cast up to a thickness of 7 mm, which is an improvement by a factor of 1.7 compared to Vit 101. This reveals that the critical cooling rate for the Si-bearing alloy to form a glass is about a factor of 3 smaller than for the alloy without Si, because the critical thickness of the sample is proportional to the square root of the critical cooling rate. If we increase the amount of Si to 2 at. %, the glass forming ability degrades again, even though the supercooled liquid region becomes larger (Fig. 4.5). This is probably due to the fact that the formation of high melting point silicides could not be avoided during processing. These silicides are likely to serve as heterogeneous nucleation sites.

The addition of silicon to the alloy increases the glass transition temperature of the alloy slightly. The reduced glass transition temperature, T_{rg}, is a value to estimate the glass forming ability of alloys and represents the ratio of glass transition temperature and liquidus temperature. In order to determine whether the reduced glass transition temperature changes with Si content, the melting behavior of the different alloys was investigated in a Perkin Elmer DTA 7.

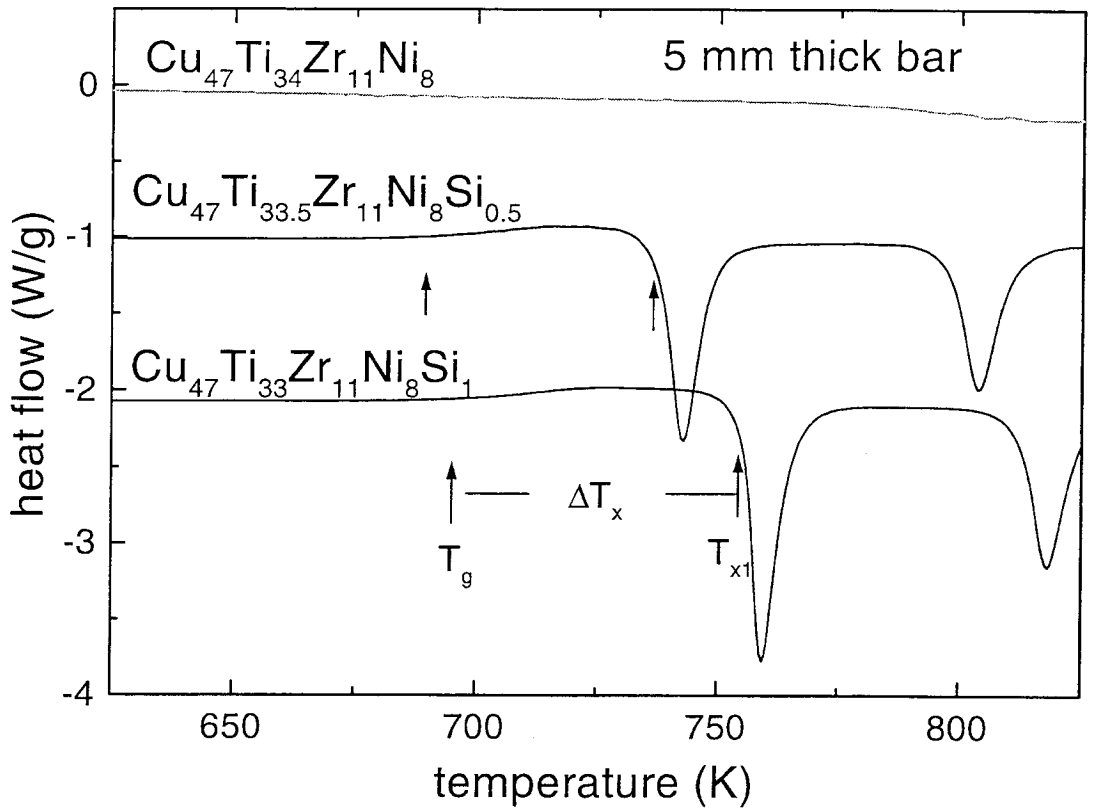

Fig. 4.7. DSC thermograms of Vit 101 and two Vit 102 alloys with different Si content, having dimension of 5 mm. Vit 101 was completely crystalline, whereas the Vit 102 alloys were amorphous prior to the DSC measurements.

As Fig. 4.8 reveals, the liquidus temperature increases slightly with Si content, which compensates the effect of an increasing glass transition temperature. The reduced glass transition temperatures for all the alloys are 0.58 within the experimental error when heated with a rate of 0.33 K/s.

4.4 DISCUSSION

During composite processing of SiC in a $Cu_{47}Ti_{34}Zr_{11}Ni_8$ bulk metallic glass matrix, we observed the formation of TiC at the interface between liquid matrix and solid SiC particles (Fig. 4.4). The growth of this layer is most likely diffusion controlled. It is governed by the diffusion of Ti from the matrix throughout the layer to the interface between the TiC and the SiC. Si diffuses in the opposite direction through the TiC layer and finally into the matrix. If one considers the high melting point of TiC of 3140 K, we can assume that the growth of the TiC layer proceeds much slower than the diffusion of Si in the liquid matrix. This means that the Si becomes virtually evenly distributed in the matrix. The result is a homogeneous matrix with a Si composition that depends on the interface area between particles and matrix as well as on the thickness of the reacted Ti-C layer. The matrix is thermally more stable with respect to crystallization when heated above the glass transition than the $Cu_{47}Ti_{34}Zr_{11}Ni_8$ alloy without silicon.

The same thermal stability can be obtained by just alloying the appropriate amount of Si with the initial alloy. In fact, if we assume that we replace each Ti-atom in the matrix that participated in the TiC formation by a Si-

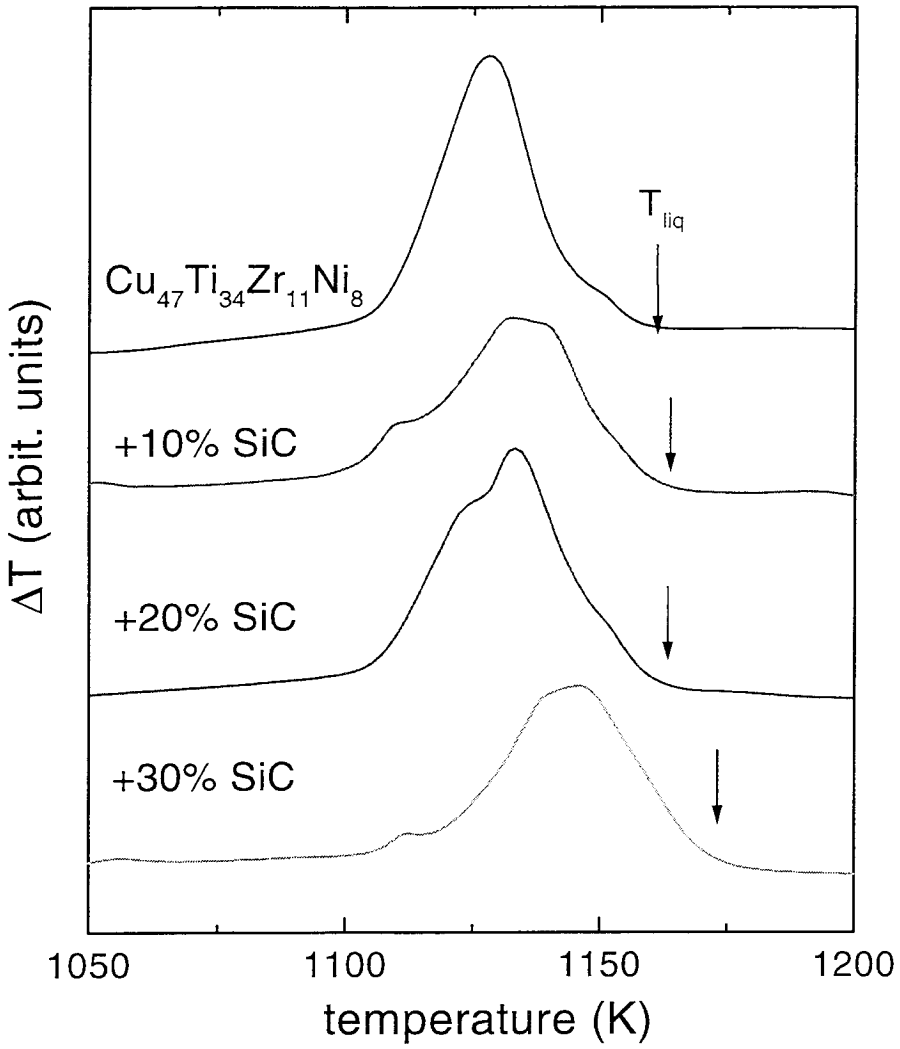

Fig. 4.8. DTA melting endotherms of the composites with different SiC contents. The liquidus temperatures of the matrix increase slightly with the Si content.

atom, we calculate as well as find experimentally that the processing of 10 vol. % 50 μm SiC particles results in a matrix concentration of 0.5 at. % Si. Consequently, an increase of volume fraction to 20% with same particle size results in 1 at. % Si in the matrix. At this point the question arises how such a small amount of Si can improve the glass forming ability considerably. As mentioned above, the reduced glass transition temperature of the alloy is virtually independent of the Si concentration. Both the glass transition temperature and the liquidus temperature increase slightly. In addition, the specific heat capacity difference at the glass transition as well as the entropy of fusion do not change. All these factors indicate that the thermodynamics of the alloy do not change by adding the silicon.

The calorimetric studies were used to calculate the activation energies of crystallization for the investigated SiC reinforced Vit 101 composites. By measuring the peak positions in Fig. 4.3 at different heating rates, it is possible to determine the activation energies for the different reaction steps by the Kissinger method[3], i.e., from the slopes of the cruves of $\ln((\partial T/\partial t)/T_p^2)$ against $1/T_p$, where T_p is the peak temperature and $\partial T/\partial t$, the heating rate. These results are presented in Fig. 4.9 for Vit 101 and SiC reinforced Vit 101 composites. The plot reveals that there is no significant change in activation barrier when adding the SiC particles and introducing Si into the glass matrix. This finding has two consequences. First, the interfaces between the TiC layer and the matrix do not act as heterogeneous nucleation sites, which would decrease the nucleation barrier. Second, the Si does not substantially change the growth kinetics and

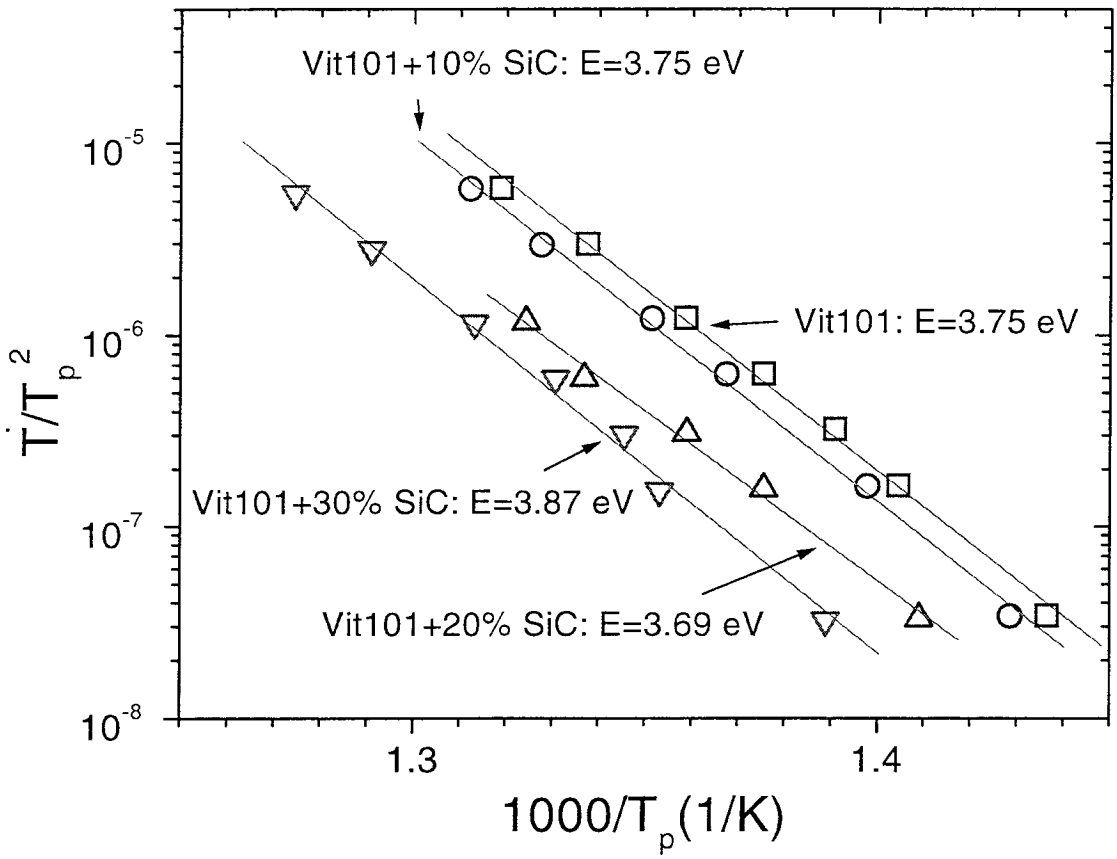

Fig. 4.9. Kissinger plots obtained after heating the composites with different heating rates. The activation energy for nucleation does not decrease if SiC particles are added. Heterogeneous nucleation at the interface between the TiC layer and the melt does not occur.

crystallization products. As shown in Fig. 4.3 the crystallization events are only shifted to higher temperatures.

The heating rate dependence of the glass transition can be analyzed by another method. It was shown earlier[4] that the heating rate dependence of T_g reflects the temperature dependence of the viscosity and the relaxation time in the supercooled liquid. Bulk metallic glasses are strong liquids[5] that show a pronounced heating rate dependence of the glass transition, which represents the structural relaxation. In Fig. 4.10, the inverse heating rate is plotted as a function of onset of glass transition normalized to T_g^*, which is the onset of the glass transition measured at 0.0167 K/s. On this "fragility plot" data are shown for different metallic glass formers. The parameter D^* indicated in Fig. 4.10 is a measure for the fragility of the liquid. As shown in the insert in Fig. 10, viscosity curves for different materials are found between $D^*=100$ (strong) and $D^*=2$ (fragile).[6] Less complex alloys such as Zr-Ni or Zr-Al-Ni are more fragile (less strong) than Zr-Ti-Cu-Ni-Be or Cu-Ti-Zr-Ni-(Si). A high fragility means a fast increase of the structural relaxation time upon rising temperature. The strong Cu-Ti-Zr-Ni alloy shows a slow increase of the structural relaxation time. It can be seen in Fig. 4.10 that the introduction of Si into the Cu-Ti-Zr-Ni matrix does not change the fragility of the alloy, i.e., if we add 10 vol. % and 20 vol. % SiC , respectively. Si does not affect the relaxation kinetics of the alloy. All Cu-Ti-Zr-Ni-(Si) liquids show the same fragility within the experimental error.

We thus can rule out that the Si influences the thermodynamics (reduced glass transition temperature), the crystallization kinetics (activation energy) and

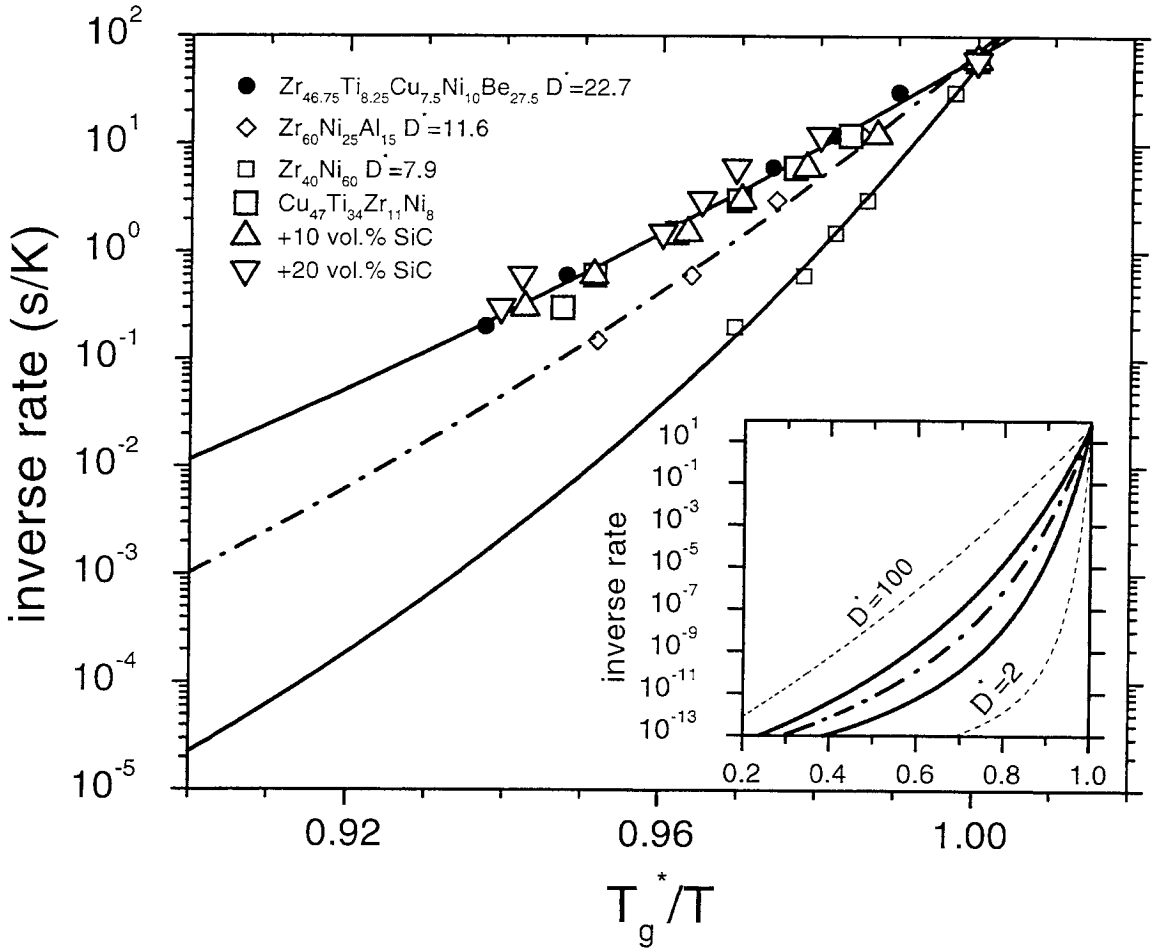

Fig. 4.10. Fragility plot of the inverse heating rate as a function of onset temperature for the glass transition normalized to the onset temperature of the glass transition measured with a rate of 0.0167 K/s (T_g). The kinetics of the glass transition do not change significantly with Si content. The insert (same units on x-axis) shows the range of viscosities that are observed for different materials.

the intrinsic kinetics (relaxation at the glass transition) in the supercooled liquid of the alloy.

4.5 CONCLUSIONS

Bulk amorphous $Cu_{47}Ti_{34}Zr_{11}Ni_8$ composites containing SiC particles up to 30 vol. % were formed by copper mold casting. The interface reaction between particles and matrix resulted in the dissolution of Si into the matrix that enhanced the glass forming ability of the matrix even though the thermodynamic and kinetic properties of the matrix did not change considerably. This leads us to the conclusion that the Si most likely acts on the impurities in the melt predominantly present in the form of oxygen.

It was shown for the $Zr_{52.5}Ti_5Cu_{17.9}Ni_{14.6}Al_{10}$ alloys that increasing amount of oxygen destroys the glass forming ability, which suggests that the presence of heterogeneous nucleation sites within the melt plays an important role during crystallization.[7] This effect should not be confused with heterogeneous nucleation at a particle/matrix interface. Since a certain amount of impurities can not be avoided in the melt, it is desirable to neutralize the nucleation sites.

In the Ni-Pd-P alloy system, it was shown by Volkert and Spaepen[8], that the addition of 1 at. % Si improves the thermal stability of the supercooled liquid of this particular alloy. In this case the improvement by adding Si was attributed to the destabilization of P_2O_5 clusters that were considered to act as nucleation

sites. In our Ti based alloy the Si might act in a similar way. Si might help to destabilize TiO_2 clusters present in the melt.

REFERENCES

1. X.H. Lin and W.L. Johnson, J. Appl. Phys. **78**, 6514 (1995).
2. R.B. Dandliker, Ph.D. thesis, California Institute of Technology (1998).
3. H.E. Kissinger, Anal. Chem., **29**, 1702 (1957).
4. R. Busch, W. Liu, and W.L. Johnson, J. Appl. Phys. **83**, 4134 (1998).
5. R. Busch, A. Masuhr, E. Bakke, and W.L. Johnson, Mat. Res. Soc. Symp.Proc. **455**, 369 (1997).
6. C.A. Angell, Science **267**, 1924 (1995).
7. X.H. Lin, Ph.D. thesis, California Institute of Technology (1997); X.H. Lin and W.L. Johnson, Mater. Trans. JIM. **38**, 475 (1997).
8. C. A. Volkert, Ph.D. thesis, Harvard University (1988).